DI Stephan Nestl, BSc

# Biogas reforming and the steam iron process for the production of pressurised hydrogen

## DOCTORAL THESIS

to achieve the university degree of

Doktor der technischen Wissenschaften

submitted to

## Graz University of Technology
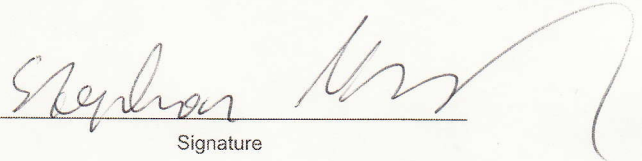
Supervisor

Assoc.Prof. Dipl.-Ing. Dr.techn. Viktor Hacker

Institute of Chemical Engineering and Environmental Technology

Graz, September 2015

# AFFIDAVIT

I declare that I have authored this thesis independently, that I have not used other than the declared sources/resources, and that I have explicitly indicated all material which has been quoted either literally or by content from the sources used. The text document uploaded to TUGRAZonline is identical to the present doctoral thesis.

__28.09.2015__
Date

Signature

*„Es ist nicht deine Schuld, dass die Welt ist, wie sie ist.*

*Es wär nur deine Schuld, wenn sie so bleibt."*

Die Ärzte. "Deine Schuld."

By Farin Urlaub *Geräusch*

Hot Action Records, 2003. CD.

# Preface

This work seeks to investigate an alternative concept for the build-up of a hydrogen infrastructure. The reformer-steam iron process enables, in the way it was developed during this thesis, the production, purification and storage of pure pressurised hydrogen based on a wide variety of hydrocarbons. The first chapter gives a short overview of the current situation of fossil fuel consumption and global warming. Chapter two introduces the concept of the reformer-steam iron process and thermodynamic simulations as well as preliminary experiments are presented. Major parts of this chapter were published in the *International Journal of Power Sources* [1]. In chapter three the steam reforming of methane and biogas using nickel and ruthenium based catalysts is discussed. Chapter four represents the work on $CeO_2$ stabilised oxygen carriers for the steam iron process and chemical looping combustion which was done during an extended research stay in the *Laboratory of Energy Science and Engineering* at *ETH-Zurich*. Chapter five can be seen as the fusion of the previous chapters. It represents the final goal of this work which was the design and construction of a working prototype for the production of pure hydrogen based on the reformer-steam iron process. A summary and conclusion of the previous chapters as well as an outlook is given in chapter six. The experimental setup and the used techniques for material characterisation are described in chapter seven.

# Acknowledgements

# Abstract

Over the past few decades worldwide energy consumption has continuously increased and this trend is not expected to end in the foreseeable future. Major efforts must be undertaken to change the energy sector which is based today on non-renewable and climate damaging fossil fuels and nuclear energy in order to protect the global climate. New technologies and energy carriers such as fuel cells and hydrogen must thus be implemented. In this thesis the results of theoretical and experimental investigations of hydrogen production, based on methane- and biogas reforming, are presented. A novel approach for efficient decentralised production of pure pressurised hydrogen is developed, based on steam reforming in combination with the cyclic steam iron process. Nickel and ruthenium based catalysts are used for the conversion of methane and biogas at temperatures between 650 °C and 750 °C and steam to carbon ratios between 2 and 4 with a conversion rate of $CH_4$ of 93% - 95%. The thermodynamics of steam methane reforming for the steam iron process reveal that this process should be performed at ambient pressure, at high temperatures and low steam to carbon ratios in order to produce a syngas with high concentrations of hydrogen and carbon monoxide but low concentrations of steam and carbon dioxide. This syngas can be used directly for the reduction of an iron based oxygen carrier and the re-oxidation of the oxygen carrier leads to the formation of pure pressurised hydrogen. Lab-scale experiments proved the concept of the process and stable hydrogen flow rates were achieved at a pressure level of 8 – 10 bar. To withstand the high temperatures and cyclic phase transitions the oxygen carrier must be stabilised with high-melting point oxides e.g. $Al_2O_3$ or $CeO_2$. Thermogravimetric analyses of synthesised oxygen carriers containing 10 wt% - 30 wt% $CeO_2$ show a stable oxygen storage capacity which only decreases between 0.1% and 0.5% per cycle. The oxygen carriers can be completely reduced to iron and $CeO_2$ while their re-oxidation with $CO_2$ leads to the formation of $CeFeO_3$. A consecutive air-oxidation step leads to the decomposition of $CeFeO_3$ which forms $Fe_2O_3$ and $CeO_2$. A prototype for the production of pure hydrogen based on the reformer-steam iron process is developed and characterised. The prototype operation using pure methane and methane-carbon dioxide mixtures led to the production of hydrogen with a purity of above 99.8% and only low amounts of 15 – 24 ppm carbon monoxide impurities. Based on the prototype experiments the ASPEN Plus simulation of the process revealed that the synthesis gas after the steam reforming at a temperature of 900 °C, at ambient pressure and with the steam to carbon ratio of 1.3 contains $H_2/H_2O$ in a ratio of 11.5 and $CO/CO_2$ in a ratio of 14.5. At thermodynamic equilibrium conditions, and without lean-gas recirculation, the reduction of the oxygen carrier leads to the hydrogen yield of 58% and the efficiency of 69% based on the lower heating values of methane and hydrogen.

# Kurzfassung

Innerhalb der letzten Jahrzehnte stieg der weltweite Energieverbrauch kontinuierlich an und ein Ende dieser Entwicklung ist nicht absehbar. Um schädliche Effekte auf das Weltklima zu minimieren, muss der momentan auf nicht erneuerbaren und klimaschädlichen fossilen Energieträgern sowie Kernenergie basierende Energiesektor wesentlich verändert werden. Neue Technologien und Energieträger, wie beispielsweise Wasserstoff und Brennstoffzellen müssen implementiert werden. In dieser Arbeit werden theoretische und experimentelle Untersuchungen zur Wasserstoffproduktion basierend auf Methan- und Biogasreformierung vorgestellt, sowie ein neuartiger Ansatz zur effizienten dezentralen Produktion von reinem Hochdruck-Wasserstoff, basierend auf der Dampfreformierung und dem Eisen-Dampf Prozess präsentiert. Katalysatoren auf Nickel- und Rutheniumbasis werden zur Umsetzung von Methan und Biogas zwischen 650 °C und 750 °C und bei Dampf zu Kohlenstoffverhältnissen zwischen 2 und 4 verwendet. Dabei werden Methanumsätze von 93% - 95% erreicht. Die thermodynamische Betrachtung der Dampfreformierung von Methan für den Eisen-Dampf Prozess zeigt, dass dieser Prozess bei Umgebungsdruck, hohen Temperaturen und niedrigen Dampf zu Kohlenstoffverhältnissen durchgeführt werden muss, um ein Synthesegas mit hohem Gehalt an Wasserstoff und Kohlenmonoxide aber niedrigen Dampf- und Kohlendioxidkonzentrationen zu produzieren. Dieses Synthesegas kann direkt zur Reduktion einer eisenbasierten Kontaktmasse verwendet werden. Die anschließende Rückoxidation mit Wasserdampf führt zur Freisetzung von reinem, verdichtetem Wasserstoff. Die Laborexperimente beweisen die Umsetzbarkeit des Konzeptes und stabile Wasserstoffflüsse konnten bei Drücken von 8 – 10 Bar erreicht werden. Zur Verbesserung der Widerstandsfähigkeit gegenüber hohen Temperaturen und zyklischen Phasenübergängen müssen die verwendeten Kontaktmassen mit hochschmelzenden Metalloxiden, wie z.B. $Al_2O_3$ oder $CeO_2$, stabilisiert werden. Thermogravimetrische Untersuchungen der hergestellten, 10 – 30 Gewichtsprozent $CeO_2$ beinhaltenden, Kontaktmassen zeigen stabile Sauerstoffspeicherkapazitäten, welche pro Zyklus nur um 0,1% – 0,5% abnehmen. Die Kontaktmasse kann komplett zu Eisen und $CeO_2$ reduziert werden, die Rückoxidation mit $CO_2$ führt zur Bildung von $CeFeO_3$. Ein anschließender Luft-Oxidationsschritt führt zur Zersetzung des $CeFeO_3$ zu $Fe_2O_3$ und $CeO_2$. Ein Prototyp zur Produktion von reinem Wasserstoff basierend auf dem Reformer-Eisen Dampf Prozess wurde entwickelt und charakterisiert. Der Betrieb des Prototyps mit reinem Methan und Methan-Kohlendioxid Mischungen ermöglichte die Produktion von Wasserstoff mit über 99,8% Reinheit und nur geringen Spuren von 15 – 24 ppm Kohlenmonoxid. Eine ASPEN Plus Simulation, basierend auf diesen Versuchen, zeigt, dass bei einer Reformertemperatur von 900 °C und einem Dampf zu Kohlenstoffverhältnis von 1,3 ein $H_2/H_2O$ Verhältnis von 11,5 und ein $CO/CO_2$ Verhältnis von 14,5 bei Umgebungsdruck erreicht wird. Am thermodynamischen Gleichgewicht führt dies ohne Berücksichtigung einer zusätzlichen Rückführung des anfallenden Schwachgasstromes zu einer Wasserstoffausbeute von 58% und einer Effizienz von 69%, basierend auf den Heizwerten von Wasserstoff und Methan.

# Content

# 1. Introduction

Dealing with the limited natural resources of the earth and the preservation of a healthy environment are main challenges of our time. The responsible and efficient utilisation of fossil resources as well as the continuous transition towards alternative and environmentally friendly forms of energy represents a commitment to all future generations. Within the last forty years the worldwide total primary energy supply has doubled and, although the amount of renewable energy has increased, fossil fuels are still the most important energy source [2]. Oil, coal and gas are limited resources and uneven distributed on earth. Almost 50% of the proved worldwide oil reserves and more than 43% of the proved worldwide reserves of natural gas are located in the Middle East while only 8.8% of the oil reserves and 30.5% of the natural gas reserves can be found in Europe and Central Asia, including Russia. The European Union only has control over 0.4% of the worldwide oil and 0.8% of the worldwide natural gas reserves [3]. Therefore, the EU is highly dependent on energy imports and crisis in oil and gas exporting countries can have huge impacts on the energy supply of 500 million EU-citizens. Beside these political and economic considerations the usage of fossil fuels has tremendous effects on the environment. In 1958 the seasonal and latitudinal variability in atmospheric carbon dioxide was documented by Charles David Keeling and the Scripps Institution of Oceanography for the very first time [4]. Long term measurements showed that atmospheric carbon dioxide concentrations each year were higher than the year before and by 1970 a worldwide increase in concentration, almost undeniably related to fossil fuel combustion was stated. In 2011 an analysis of the longest available records of atmospheric carbon dioxide and its $^{13}C/^{12}C$ ratio was published by the Scripps Institution of Oceanography [5]. The analysis documented the progressive build-up of a carbon dioxide excess in the northern hemisphere tied to fossil fuel burning. Figure 1 shows the changing carbon dioxide concentrations during different timespans. Based on ice-core data, Figure 1-A and B show that the carbon dioxide content ranged from below 200 ppm to below 300 ppm during the last 800 000 years but never exceeded 300 ppm until the beginning of the 20$^{th}$ century. Since 1958 detailed gas analysis is carried out and, therefore, also the seasonal change of the carbon dioxide concentration can be measured (Figure 1-C and D). Since mankind has started to combust fossil fuels on an industrial scale, the concentration of carbon dioxide has continuously increased and since more than 100 years, each year represents a new all-time record of carbon dioxide concentration. The increasing concentration of carbon dioxide, which is now in the range of 400 ppm (Figure 1-D), leads to an increased amount of adsorbed infrared radiation in the atmosphere. The adsorbed energy is re-emitted to the surface and the lower atmosphere and causes an increased global temperature. This mechanism, known as the greenhouse effect, significantly influences the global climate.
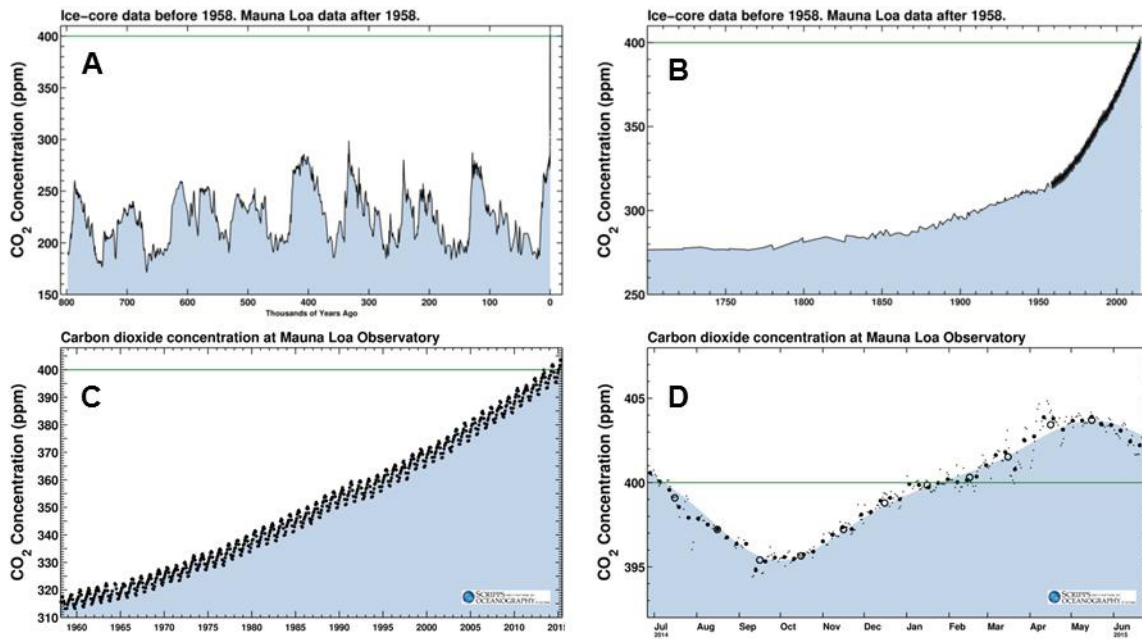
**Figure 1: Keeling curves for the last 800 000 years; latest CO$_2$ reading on June 25, 2015: 402.76 ppm [6].**

The averaged global surface temperature is 14 °C which is approximately 33 °C higher than it would be without the greenhouse effect [7,8]. Joseph Fourier is widely credited as being the first to recognise the importance of the greenhouse effect for the Earth's climate [9]. In 1827 he pointed out that the atmosphere is relatively transparent to solar radiation, but highly absorbent to thermal radiation [10]. This effect was further investigated by John Tyndall who investigated the adsorption of different gaseous compounds such as carbon dioxide and water vapour and pointed out that these components are responsible for the effect, although only trace amounts are present in the atmosphere [11]. Since 1995, greenhouse-gas (GHG) emissions have risen by more than one-quarter and the atmospheric concentration of these gases has increased steadily to 435 parts per million carbon-dioxide equivalent (ppm CO$_2$-eq, including CO$_2$, CH$_4$ and N$_2$O) in 2012 [12]. Although the natural greenhouse effect is essential for a habitable planet the continuous emission of greenhouse gases caused by the combustion of fossil fuels but also by other human caused actions, such as intensive cattle-breeding and fertilisation, will have significant impacts on the climate. Each of the last three decades has been successively warmer at the Earth's surface than any preceding decade since 1850 [13]. In 2007 the International Panel on Climate Change (IPCC) stated that most of the observed increase in global average temperatures since the middle of the 20th century is very likely due to the observed increase in anthropogenic greenhouse gas concentrations [14]. In 2014 the world bank group stated that data already showed dramatic climate changes, heat and weather extremes are already impacting people, damaging crops and coastlines and putting food, water, and energy security at risk [15]. In 2015 the IPCC has concluded that, in the absence of fully committed and urgent action, climate change will have

severe and irreversible impacts across the world [12]. These actions have to be a combination of all available technologies such as the utilisation of bio-based resources, renewable electric power generation and clean-mobility. In addition, also minimisation of energy dissipation by increasing process efficiency in every sector of society is necessary. Several reviews addressing the advantages and disadvantages of each of the various renewable energy conversion technologies were published within the last years [16–19]. Important progress was made in these fields. The global cumulative installed wind capacity increased from 7,600 MW in 1997 to 369,597 MW in 2014 which equals an increase by a factor of 48 [20]. The global cumulative installed photovoltaic capacity increased from 1,288 MW in 2010 to 138,856 MW in 2013 which equals an increase by a factor of 108 [21]. The world biofuel production volumes increased from 35 billion litres in 2005 to 107 billion litres in 2011 which equals an increase by a factor of 3 [22]. Globally, renewable electricity generation is estimated to rise to 25% of gross power generation in 2018, up from 20% in 2011 and 19% in 2006 [23]. In addition to these technologies, hydrogen has received more and more attention as a possible fuel of the future, especially in combination with fuel cells. Schultz et al. simulated the effects of a transition from fossil fuels combustion to fuel cell technology and stated that this can lead to substantially improved air quality and reduced climate forcing, provided that the hydrogen would be generated without additional emissions of ozone precursors and greenhouse gases [24]. Kleijn and Van der Voet investigated the resource constraints in a 100% hydrogen based economy and found out that renewable primary energy sources, mainly wind and solar energy, are sufficient to produce enough hydrogen for an growing world economy but the distribution of hydrogen as well as some scarce resources, e.g. platinum for fuel cells, might become show-stoppers [25]. Bartels et al. compared the costs of hydrogen production in 2010 and stated that coal and natural gas are the cheapest sources of hydrogen but also biomass provides an economic feedstock [26]. Andrews and Shabani re-envisioned the role of hydrogen in a sustainable energy economy and stated that hydrogen would play a crucial role in road and rail vehicles requiring a range comparable to petrol and diesel vehicles, in coastal and international shipping, in air transport and for longer-term seasonal storage of energy [27]. Mazloomi and Gomes further investigated hydrogen as an energy carrier and highlighted the possibility of decentralised hydrogen production and the profitability of hydrogen production using electric energy during off peak periods [28]. They identified storage and distribution of large amounts of hydrogen as main challenges for hydrogen as energy carrier. Contrary to this finding, in 2013 Agnolucci et al. presented a model for the optimisation of a hydrogen supply chain which had a tendency for large and medium-sized production facilities [29]. Although there is still discussion about the best technologies for hydrogen production, distribution and infrastructure development, a wide consensus on the importance of hydrogen as the crucial

energy carrier of the 21$^{st}$ century was reached by representatives of the industry, the scientific communities and by political leaders.

# 2. The reformer-steam iron process

Parts of the work presented in this chapter are part of the publication *The production of pure pressurised hydrogen by the reformer-steam iron process in a fixed bed reactor system* [1]. The experimental work was done by Michael Lammer (thesis completed in 2014) and Bernhard Marius (thesis submitted in 2015) under my guidance and parts of it can also be found in their master theses [30,31].
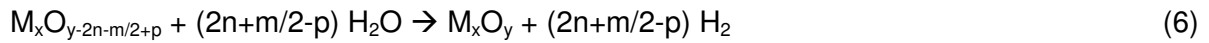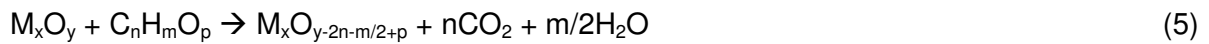
## 2.1. Fundamentals

Fuel cells have the potential to make emission free power generation and mobility possible but in order to achieve these goals an area-wide hydrogen supply is required. Today hydrogen is mainly produced for industrial applications and only corresponds to less than 2% of the world's primary energy demand [32]. Therefore, major efforts have to be undertaken to increase the capacities for hydrogen production, distribution and storage. One promising approach to achieve a comprehensive supply of hydrogen is its decentralised production based on an already existing supply infrastructure. This minimises the efforts needed for hydrogen transportation and long-term storage and enables a continuous growth of the hydrogen production capacity directly connected with the increasing demand for hydrogen. The only already fully commercialised technology for decentralised hydrogen production is electrolysis but, due to its high costs and low overall efficiency, this process is only favourable in periods of overproduction of electric energy. On the other hand, the decentralised conversion of hydrocarbons to a hydrogen rich syngas enables hydrogen production without such limitations. In the beginning this production method might include fossil fuels such as natural gas. In the mid and long term perspective the conversion of renewable resources, such as bio-ethanol, glycerine, solid biomass or biogas, offers a possibility for hydrogen production without net $CO_2$ emissions. The production of bio-based energy carriers requires large areas and the energy content of these compounds is low. The transport over long distances to the customer needs high amounts of energy and is economically challenging. This favours the on-site conversion of renewable resources to hydrogen. The common methods for $H_2$ production based on hydrocarbons are steam reforming (Eq. (1)), partial oxidation (Eq. (2)) and autothermal reforming (Eq. (3)) which is a combination of Eq. (1) and (2). These methods produce a CO rich syngas and are often combined with the water-gas shift reaction (Eq. (4)) to increase the amount of produced $H_2$.

$$C_xH_y + xH_2O \rightarrow (x+y/2)\ H_2 + xCO \hspace{4cm} (1)$$

$$C_xH_y + x/2O_2 \rightarrow y/2H_2 + xCO \hspace{4.5cm} (2)$$

$$C_xH_y + (x-z)\,H_2O + z/2O_2) \rightarrow (x-z+y/2)\,H_2 + xCO \tag{3}$$

$$H_2O + CO \leftrightarrow H_2 + CO_2 \tag{4}$$

Since the carbon monoxide conversion of the water gas shift reaction is thermodynamically limited at high temperatures and kinetically limited at low temperatures a two-stage process at different temperatures is required to maximise the amount of $H_2$ in the syngas. In order to remove the $CO_2$ as well as unreacted CO and $C_xH_y$ an additional purification step is necessary. This final gas clean up can be done by pressure swing adsorption (PSA), monoethanolamine scrubbing (MEA) or membrane based processes. For large scale hydrogen production PSA and MEA are technologically mature and show a good overall efficiency but are difficult to downscale. Membrane based hydrogen production, on the other hand, shows advantages in decentralised hydrogen production since it enables compact system design and low operation temperatures [33,34]. Though, it suffers from high material costs and needs further research. Therefore, up to now, no technology can completely fulfil the requirements for cost effective and efficient decentralised production of pure hydrogen. An alternative approach for filling this gap is chemical looping hydrogen production (CLH) according to Eq. (5) and (6).

$$M_xO_y + C_nH_mO_p \rightarrow M_xO_{y-2n-m/2+p} + nCO_2 + m/2H_2O \tag{5}$$

$$M_xO_{y-2n-m/2+p} + (2n+m/2-p)\,H_2O \rightarrow M_xO_y + (2n+m/2-p)\,H_2 \tag{6}$$

Chemical looping processes such as chemical looping combustion (CLC) and chemical looping reforming (CLR) have gained much interest during the last years as an efficient technology for $CO_2$ capture and storage applications [35–39] as well as for hydrogen production and purification [40–44].

## 2.2.    The reformer-steam iron process for production, purification and storage of pressurised hydrogen

The reformer-steam iron process, as an innovative process for the decentralised production of pure pressurised hydrogen, can be an important alternative to other chemical looping processes. The process is based on the *steam iron process* and the *reformer sponge iron cycle* published by Hacker et al. [45,46] which in turn are based on the historic *Messerschmitt-process* [47]. It features the production, purification and storage of hydrogen based on methane, biogas or higher hydrocarbons in one compact unit. In the first step a catalytic steam reforming reaction according to Eq. (1) is performed. This leads to the formation of a syngas, which is rich in CO and $H_2$ and is used in a consecutive step for the

stepwise reduction of a haematite ($Fe_2O_3$)-based oxygen carrier to magnetite ($Fe_3O_4$), wustite (FeO) and iron (Fe) according to Eq. (7) – (9).

$$3Fe_2O_3 + H_2/CO \rightarrow 2Fe_3O_4 + H_2O/CO_2 \tag{7}$$

$$Fe_3O_4 + H_2/CO \rightarrow 3FeO + H_2O/CO_2 \tag{8}$$

$$3FeO + 3H_2/CO \rightarrow 3Fe + 3H_2O/CO_2 \tag{9}$$

The maximum conversion rates of the reactions (7) – (9) depend on the equilibrium constants of the particular reaction. The so-called Baur–Glaessner diagram is often used to illustrate the equilibrium concentrations as a function of temperature and composition of the solid phase [40,48]. Figure 2 shows the different $H_2$ conversion rates which can be measured during the reduction of $Fe_2O_3$ in a fixed bed reactor. At the beginning of a reduction, when the reactor is filled with $Fe_2O_3$, complete hydrogen conversion can be achieved via reaction (7). After a certain amount of time, when most of the $Fe_2O_3$ is reduced, the equilibrium constants of reactions (8) and (9) limit the $H_2$ conversion.
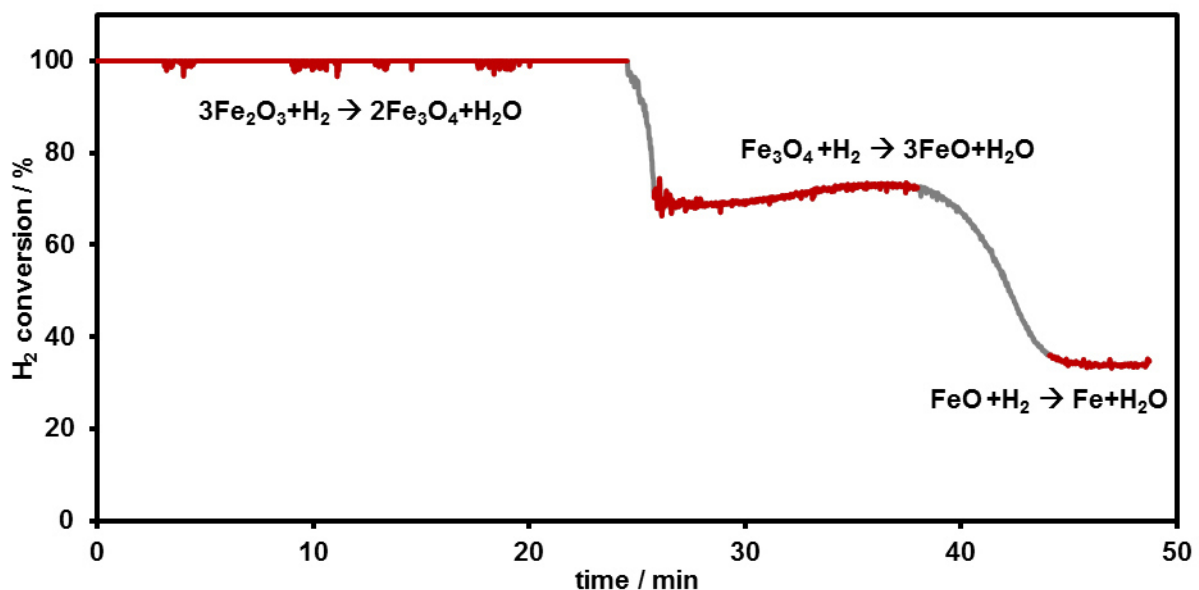


**Figure 2: Reduction of an $Fe_2O_3$-$Al_2O_3$ (90 wt% + 10 wt%) oxygen carrier at 800 °C with hydrogen in a fixed bed reactor [49].**

Besides reactions (7) - (9) also the direct reduction of haematite with methane following Eq. (10) is possible.

$$4Fe_2O_3 + 3CH_4 \rightarrow 8Fe + 3CO_2 + 6H_2O \tag{10}$$

The reduction reactions (7) – (9) can be performed at the same temperature as the reforming reaction which allows the realisation of a simple and compact unit that works without heat

exchanging steps between reforming and reduction. After the reduction step the iron is re-oxidised with steam (Eq. (11) and (12)).

$$3Fe + 3H_2O \rightarrow 3FeO + 3H_2 \tag{11}$$

$$3FeO + H_2O \rightarrow Fe_3O_4 + H_2 \tag{12}$$

As long as the formation of solid carbon is prevented during the reduction step, pure hydrogen for applications such as low temperature fuel cells is generated. After a cooling step, to remove unreacted steam from the product, pure hydrogen is obtained. If this process is operated at elevated pressure it is possible to produce pressurised hydrogen without the usage of an additional gas compression step. After the steam-oxidation step an additional oxidation step using air can be used to regenerate magnetite to haematite (Eq. (13)) otherwise the following reduction cycle starts with magnetite.

$$2Fe_3O_4 + 1/2O_2 \rightarrow 3Fe_2O_3 \tag{13}$$

Since the oxidation with steam only leads to the formation of $Fe_3O_4$ instead of $Fe_2O_3$ the amount of syngas which is used for the conversion of $Fe_2O_3$ to $Fe_3O_4$ cannot be recovered as hydrogen. This amount is 1/9 of the total amount of syngas ($SEQ_{,\ total}$) which would be needed for the complete reduction of $Fe_2O_3$ to Fe. Therefore, the maximum amount of hydrogen which can be produced from the reaction $Fe_2O_3 \rightarrow Fe \rightarrow Fe_3O_4$ using a certain amount ($SEQ_{,\ converted}$) of the total amount of syngas is given by equation (14). The term syngas equivalent (SEQ) is used to compare different reducing species in matters of the amount of oxygen atoms they can remove from the oxygen carrier. SEQ depends on the chemical composition of the reducing species and the general formula (Eq. (15)) is derived from equations (5) and (6). For the species $H_2$, CO and $CH_4$, which are considered in this thesis the corresponding values are 1, 1 and 4.

$$H_2 \cdot SEQ^{-1}_{,\ converted} = (SEQ_{,\ converted} - 1/9\ SEQ_{,\ total})/SEQ_{,\ converted} \tag{14}$$

$$SEQ = 2n + m/2 - p \tag{15}$$

In the ideal case of complete reduction of $Fe_2O_3$ to Fe and its re-oxidation to $Fe_3O_4$, the amount of produced hydrogen is 88.89% of the used SEQ. Since the share of not recovered syngas is always 1/9 of the total amount, needed for complete reduction, the ratio of recovered hydrogen per amount of SEQ is a function of the oxygen carrier conversion at the reduction step. Figure 3 shows the amount of produced hydrogen per used SEQ as a function of the solid oxygen carrier conversion and the different steps of the reduction reaction. It is obvious that the first 11% of the reducing species are used for reaction (7) and, therefore, it cannot be recovered as hydrogen. With ongoing oxygen carrier conversion the

amount of produced hydrogen per SEQ increases. At 33.33% solid conversion, which equals a complete reduction to FeO, 66% of the syngas can be converted to hydrogen. A maximum of 88.89% produced hydrogen per used SEQ can be reached if the solid oxygen carrier is completely converted to Fe.
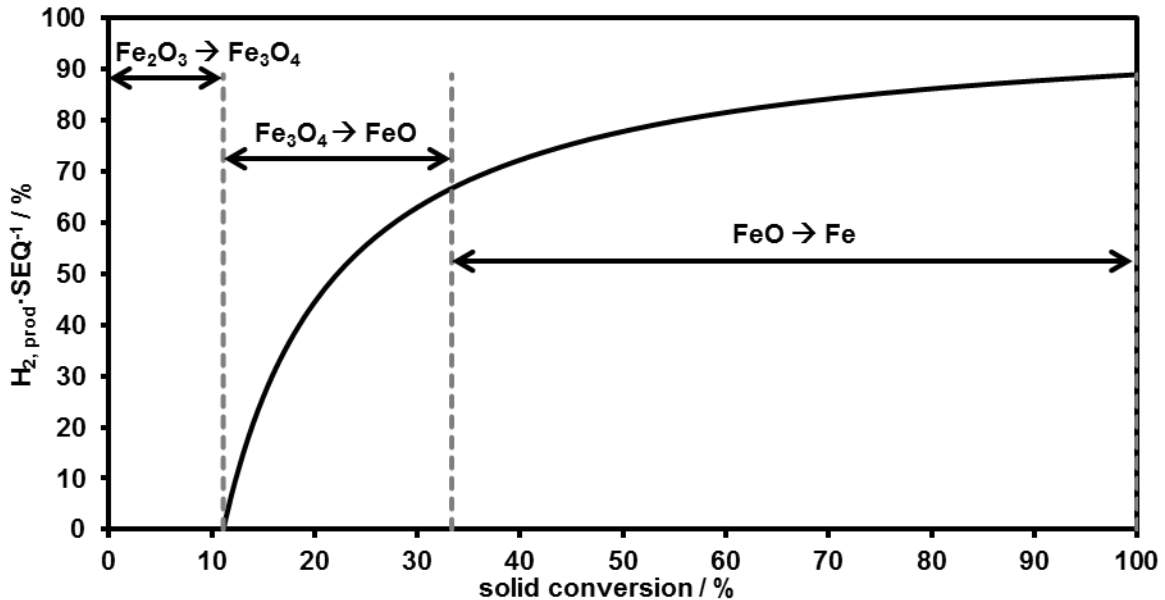


**Figure 3: Maximum amount of producible hydrogen from the reaction $Fe_2O_3$ → Fe → $Fe_3O_4$ (calculations and figure based on Aston et. al [44]).**

Different reactor concepts have been investigated for chemical looping but most operating plants use a configuration of two interconnected or circulating fluidised beds [37,43]. Such a configuration offers advantages on large scale applications but for decentralised hydrogen production a system of periodically operated fixed bed reactors, where generation of syngas, reduction and oxidation are performed in one compact unit, is to favour. Instead of moving the solid between two reactors the gas streams are switched between reduction and oxidation. For decentralised hydrogen production this configuration is expected to show three major advantages. The most obvious one is that, compared to interconnected fluidised bed technology, the fixed bed operation is less complex and more compact. Therefore, it represents a simple and cost efficient process for hydrogen production. Furthermore it enables a discontinuous operation and can be used as a hydrogen storage system. By keeping the iron in its reduced state, storage of hydrogen without any losses caused by diffusion or hydrogen boil-off is achieved. A simple steam treatment leads to the re-oxidation of the iron and releases hydrogen. Based on Eq. (11) and (12) a calculated mass based storage density of 4.8 wt% is possible [48,50,51]. The third advantage is that the periodically operation of the reactor enables the production of pressurised hydrogen without an additional gas compression step. The most commonly used method of hydrogen storage in fuel cell vehicles is compressed hydrogen tanks [52]. State of the art fuel cell powered vehicles store

hydrogen in pressure cylinders at a level of 350-700 bar. Therefore, after its generation additional hydrogen compression steps are necessary. These steps significantly reduce the efficiency of the whole process and increase the costs of a small-scale hydrogen production unit. The amount of consumed energy, as well as the complexity of the compression step, can be decreased significantly by increasing the production pressure of the produced hydrogen. Ahluwalia, Hua and Peng calculated the energy demand for the compression of hydrogen from 20 bar to 425 and 850 bar with 6 and 9.6% of the energy content of hydrogen [53]. Papadias et al. pointed out the dependence of the initial pressure on the efficiency of the hydrogen compression process [54]. They calculated an energy requirement for hydrogen compression, assuming an electric grid efficiency of 32.5%, from 1 to 425 atm of almost 40% of the lower heating value of hydrogen. Starting from an initial pressure of 20 atm the compression energy decreased to 20%. They proposed a membrane based process using a liquid feedstock for pressurised hydrogen production in order to increase the efficiency of hydrogen compression. Since the pressure built-up comes from the evaporation of the fuel such processes are limited to a liquid feedstock. The reformer-steam iron process can be used for the production of pressurised hydrogen without such a limitation. By the evaporation of water, the steam-oxidation pressure can be increased arbitrarily. Since the energy demand for pumping liquid water at elevated pressure is significantly lower than a subsequent hydrogen compression step a more efficient process is realised.

## 2.3.    Materials and experimental methods

This work investigated the feasibility of the reformer-steam iron process for the production of pure pressurised hydrogen. Therefore, a thermodynamic evaluation of the methane decomposition reaction as well as the steam reforming reaction was carried out. Special emphasis was given to the formation of solid carbon as this is of special importance for the generation of pure hydrogen. Experiments were performed using pure hydrogen, as well as a syngas mixture for the reduction of an iron based oxygen carrier. Steam-oxidation experiments were conducted to produce hydrogen at a maximum pressure of 11 bar(g). The experiments were carried out in a fixed bed reactor system and the solid was accessorily characterised by thermogravimetric analysis (TGA), scanning electron microscopy (SEM) and the Brunauer–Emmett–Teller method (BET).

### 2.3.1.  Thermodynamic analysis

The simulation was carried out using the software ASPEN Plus$^{TM}$ - V7.2 (Aspen Technology, Inc.) with the Standard Peng-Robinson equation of state which is suitable for gas processing of hydrocarbons [55,56]. Equilibrium compositions of the steam reforming process as well as

methane decomposition were calculated by the minimisation of the Gibbs function using the RGibbs reactor block. The investigated parameters were the temperature, the s/c-ratio and the pressure. A temperature range of 900 - 1300 K (step size 25 K) a s/c-ratio of 1 - 5 (step size 0.25) and a pressure range of 1.013 - 16.212 bar(a) were investigated. Special emphasis was given to the avoidance of carbon deposition as well as to the evaluation of the $H_2/H_2O$ and $CO/CO_2$ ratios of the syngas.

### 2.3.2. Sample preparation and characterisation

Samples of $Fe_2O_3$-$Al_2O_3$ were prepared by mechanical mixing of haematite powder (325 mesh) and $Al_2O_3$ powder (20 - 50 µm), both Alfa Aesar. A dry mixture containing 90 wt% $Fe_2O_3$ and 10 wt% $Al_2O_3$ was homogenised using an intensive mixer (Maschinenfabrik Gustav Eirich GmbH & Co KG). After the homogenisation step deionised water was slowly added during continuous mixing which led to the formation of granulate. After drying at 373 - 423 K in air the produced $Fe_2O_3$-$Al_2O_3$ granulates were fractionised. For material characterisation a 1 - 2 mm fraction of the material was crushed and fractionised again. A 90-125 µm fraction was characterised in a fixed bed reactor, by TGA, SEM and BET.

### 2.3.3. Fixed bed reactor experiments

The experiments were carried out placing 6.06 g of $Fe_2O_3$-$Al_2O_3$ (68 mmol Fe) in a tubular reactor made of HastelloyX® alloy (Parker Autoclave Engineers). An additional layer of silicon dioxide (Fluka Chemika, Quartz) was used as a preheating zone for the gases. The reactor was placed in an automated test rig for catalytic activity tests partly modified for the steam-iron-experiments (Figure 4). Heating was conducted with an electric furnace implemented into the test rig. The temperature was measured and controlled by means of a type K thermocouple inserted into the fixed bed. The reactor system and the piping were placed in a hot-box in order to avoid condensation of water. Gas analysis was carried out using a mass flow controller (Bronkhorst) and a micro gas chromatograph (Agilent 3000). Reduction and oxidation were carried out at 1023 K. For reduction 25 ml·min$^{-1}$ of hydrogen or 58 ml·min$^{-1}$ syngas (40 ml·min$^{-1}$ $H_2$, 12 ml·min$^{-1}$ CO, 6 ml·min$^{-1}$ $CO_2$) were used. In the latter also 24 ml·min$^{-1}$ $N_2$ as an internal standard for gas analysis were added. Gases were dosed using thermal mass flow controllers (Bronkhorst). Steam generation for the oxidation was performed by pumping liquid water (0.03 g·min$^{-1}$) with a HPLC pump (Gilson 307 piston pump) into the evaporator section of the system. Pressure was built up by closing the exit mass-flow controller. By this means the pressure build-up corresponded directly to the amount of generated hydrogen. By opening the mass-flow controller to a defined volume during the oxidation reaction a constant flow could be achieved.
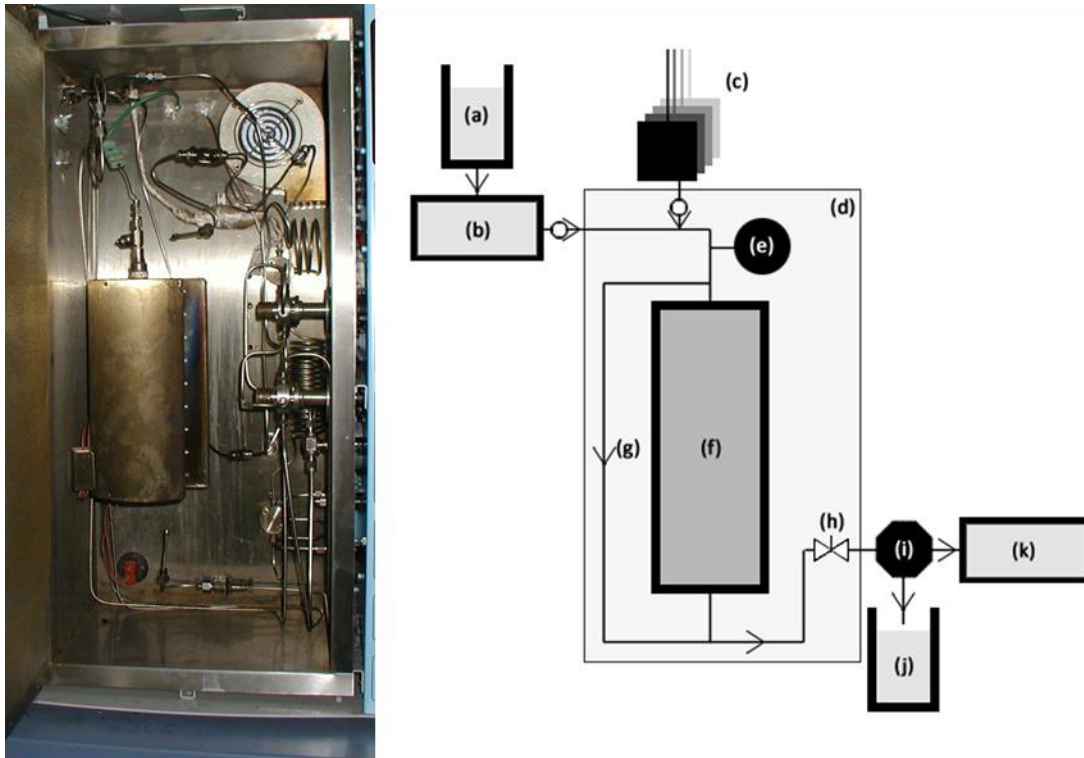
**Figure 4: Photography and schematic view of the microactivity-reference (PID Eng&Tech): (a) water reservoir, (b) HPLC pump, (c) gas supply and mass flow controllers, (d) hot box, (e) pressure sensor, (f) reactor, (g) reactor bypass, (h) pressure regulating valve (not used), (i) liquid-gas separator, (j) reservoir for condensate, (k) analysis system and MFC for pressure control.**

### 2.3.4. Thermogravimetric analysis

The TGA experiments were conducted using a thermo gravimetric analyser (STA 449C Jupiter, Netzsch) with a steam generator (aDrop, containing a Bronkhorst liquid flow controller). The weight change of the iron oxide was measured isothermal at 1023 K as a function of time. About 50 mg of $Fe_2O_3$-$Al_2O_3$ (90 - 125 µm) were heated to the reaction temperature following a temperature ramp of 10 K·min$^{-1}$ in nitrogen atmosphere. The reaction gas was a mixture of 100 ml·min$^{-1}$ $H_2$ and 30 ml·min$^{-1}$ $N_2$ for the reduction and 3.82 g·h$^{-1}$ steam and 30 ml·min$^{-1}$ $N_2$ for the oxidation. The reaction time was set to 20 minutes for the reduction step and to 10 minutes for the oxidation. To avoid mixing of the reactive gases a purge phase with $N_2$ was performed between each step for 5 minutes. To evaluate the stability of the iron oxide 9 cycles of reduction and oxidation were performed at ambient pressure.

### 2.3.5. Scanning electron microscopy

Scanning electron microscopy (SEM) images were taken with a Zeiss Ultra 55 at an acceleration voltage of 15kV. The „In-lens" detector collects especially the secondary

electrons emitted by the primary beam (SE1) and gives a better lateral resolution than the Everhart-Thornley-detector (ETD or SE2). Additionally for material contrast, which is related to the atomic number, backscatter images were taken with the AsB-detector.

## 2.4. Results and discussion

### 2.4.1. Thermodynamic analysis

Some work is published about chemical looping processes at elevated pressure, especially for chemical looping combustion of coal. The pressurised operation is expected to increase the thermal efficiency of the process as well as the efficiency of the consecutive carbon dioxide sequestration [57,58]. Chaudhari et al. also studied chemical looping combustion of simulated synthesis gas at 100 psi (6.89 bar) [59]. The direct reduction of iron oxide with syngas or methane for hydrogen production is possible and already demonstrated on a pre-industrial scale of 25 $kW_{th}$ using a system where iron oxide is circulated through several reactors [60,61]. However, less attention was given to the syngas generation step and no focus was given on the decentralised production of pure pressurised hydrogen. Three operation modes for the production of pure pressurised hydrogen by the steam iron process using methane as fuel are possible:

- The direct reduction of iron oxide with $CH_4$

- The conversion of $CH_4$ to syngas followed by the reduction at elevated pressure

- The conversion of $CH_4$ to syngas followed by the reduction at ambient pressure

At the fixed bed operation, as it is studied here, the formation of solid carbon is a critical issue especially in the case of direct reduction with methane. At the beginning of a reduction step, when the reactor is filled with haematite, the formation of steam and carbon dioxide according to Eq. (10) is possible. By the nature of the process, regions of different reduction stages are generated during the reduction period, as shown in Figure 5.
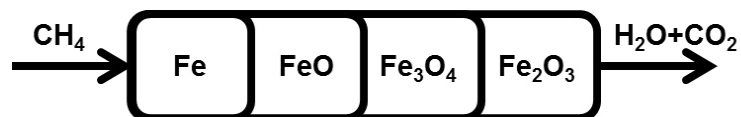


**Figure 5: Schematic illustration of regions with different oxygen content of the solid in fixed bed operation.**

Therefore, at a given moment reaction (10) is not possible due to a lack of oxidised iron. This enables the formation of solid carbon following Eq. (16).

$$CH_4 \leftrightarrow C_s + 2H_2 \tag{16}$$
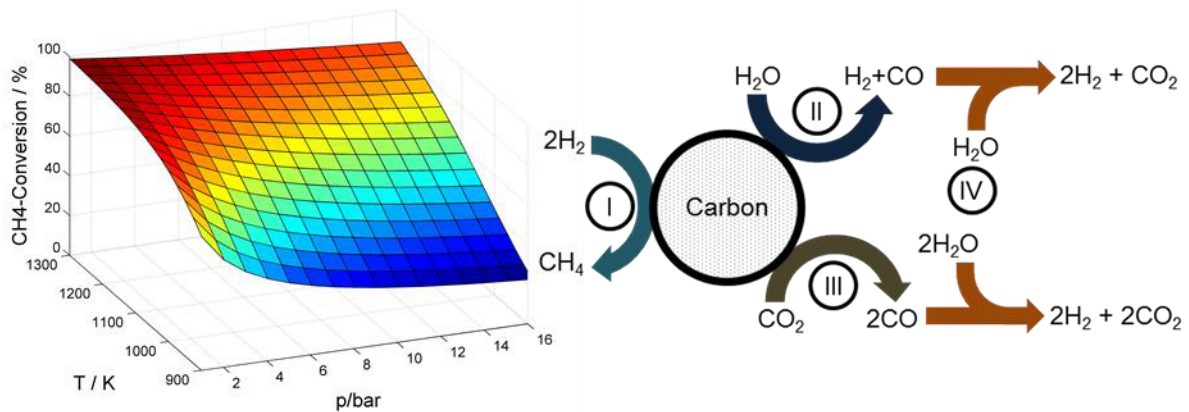
**Figure 6: Conversion of methane according to Eq. (16) in a reactor section of fully reduced iron (left) and possible reactions of solid carbon during the steam-oxidation step of the steam iron process (right).**

As seen in Figure 6 the decomposition of methane is possible over the whole temperature and pressure range investigated. Following the principle of Le Chatelier highest $CH_4$-conversion of 99% occurs at ambient pressure and at 1300 K. Even at 16 bar and at a temperature of 900 K, 22% of the fuel is converted to solid carbon. Since iron is known to catalyse the carbon deposition reaction the formation of solid carbon is unavoidable [62–65]. During the consecutive oxidation step the solid carbon can react to carbon monoxide, carbon dioxide or methane. Figure 6 gives an overview about possible reactions which can occur if carbon formation is not avoided. Since $CH_4$ does not influence the performance of PEM-FCs the hydrogenation of solid carbon (I) does not influence the hydrogen quality for this application [66,67]. By contrast, of special importance are reaction (II) and (III) which lead to the formation of carbon monoxide and, therefore, only limited usability of the produced hydrogen for low temperature fuel cells. Reaction (IV) leads to the formation of carbon dioxide and, therefore, enables reaction (III). Some work is published about the formation of inert carbon at iron particles that is not oxidised during the steam treatment and, therefore, does not lead to carbon monoxide impurities in the produced hydrogen [68,69]. Irrespective of this finding the formation of solid carbon has to be avoided since it may form amounts of carbon monoxide during the oxidation or plug the reactor during the reduction step after several cycles. Therefore, a prior syngas generation step by steam reforming has to be implemented. A thermodynamic analysis was carried out in order to investigate the influence of pressure on this reaction. Figure 7 shows the decrease of $CH_4$-conversion at 4 different pressure levels as a function of s/c-ratio and temperature. Almost complete methane conversion is possible at each pressure level but higher temperatures and s/c-ratios are needed at high pressure.
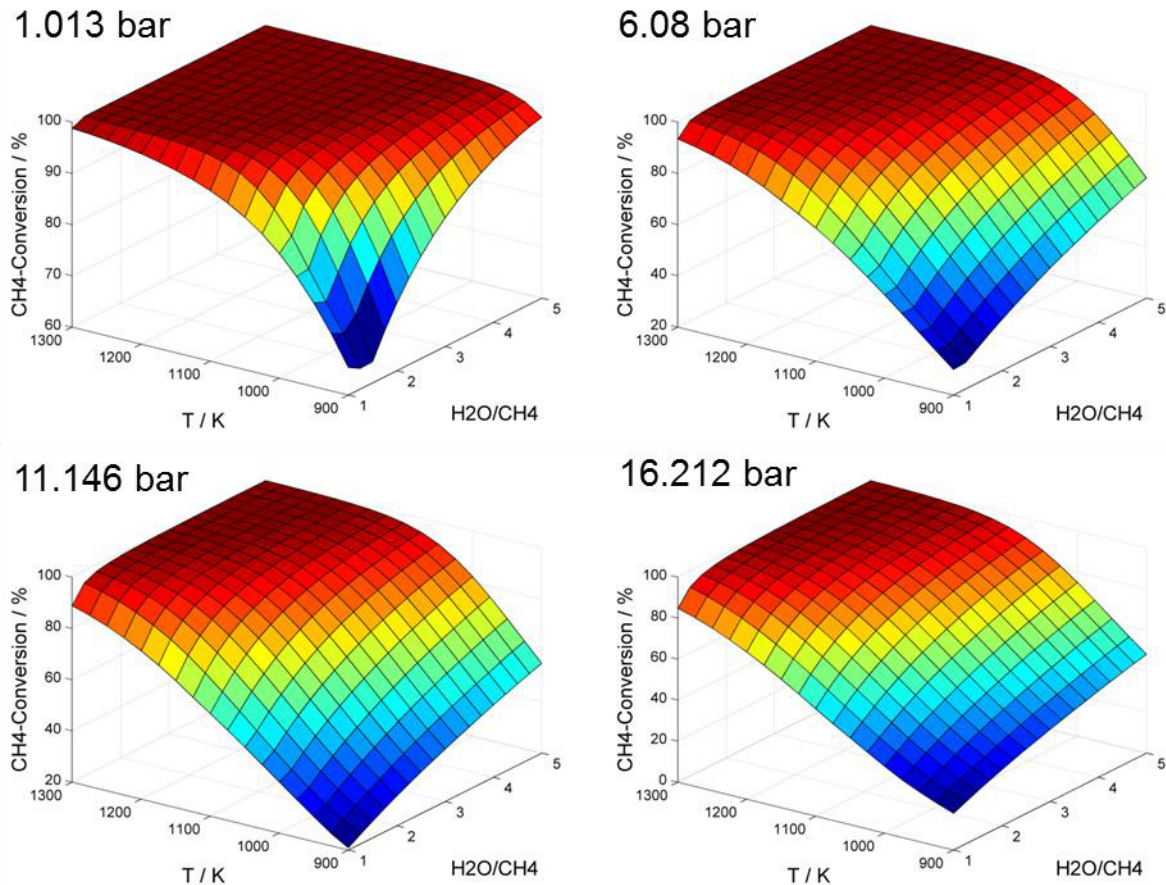
**Figure 7: CH$_4$-conversion by steam methane reforming with T=900 - 1300 K and an s/c ratio of 1-5 at four different pressure levels.**

At conventional large-scale hydrogen production an efficient heat integration and steam recovery are possible. Therefore, high overall efficiencies can be achieved also at high temperatures and s/c-ratios. For decentralised hydrogen production by the reformer-steam iron process an increase of temperature and especially an increase of the s/c-ratio are no options because of two limitations. Number one is the fact that an efficient heat-integration is more complex for smaller systems. Therefore, stricter limitations are given for the maximum operation temperature. While this challenge can be solved by innovative engineering solutions, such as catalytic combustion systems and micro-heat exchangers, the second limitation is a more fundamental one. The reactivity of the produced syngas is strongly influenced by the s/c-ratio. An increase of the s/c-ratio, as it is necessary to achieve high CH$_4$-conversion rates at high pressure, strongly decreases the H$_2$/H$_2$O and CO/CO$_2$ ratios of the syngas. Figure 8 shows the highest achievable H$_2$/H$_2$O and CO/CO$_2$ ratios of the produced syngas as a function of pressure at 1200 K and s/c=1 as well as CH$_4$-conversion as function of pressure and s/c-ratio at different temperatures. It can be seen that high amounts of hydrogen and carbon monoxide as well as high CH$_4$-conversion are only possible at ambient pressure while even a moderate pressure increase leads to a syngas of lower reactivity with high amounts of unreacted CH$_4$. High conversion rates of more than 99% are

possible at high pressure but temperature and s/c-ratio have to be increased. At a moderate system pressure of 16 bar even with a temperature of 1200 K and a s/c-ratio of 5 it is not possible to achieve full conversion. At a temperature of 1300 K the s/c-ratio of 2.75 is necessary for 99% $CH_4$-conversion.
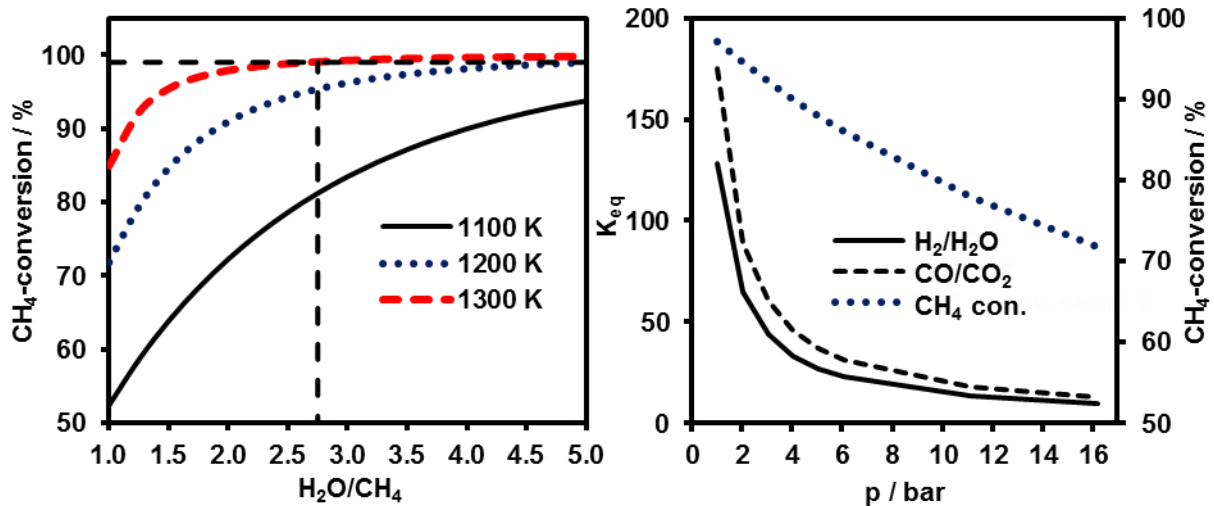


**Figure 8: $CH_4$-conversion as a function of the s/c-ratio at 16.212 bar (left) and as a function of pressure as well as ratios of $H_2/H_2O$ and $CO/CO_2$ at 1200 K and s/c=1 as a function of pressure (right).**

The formation of solid carbon via reaction (16) or the Boudouard reaction (17) only occurs at $H_2O/CH_4$ ratios below 1.5 and temperatures below 1100 K at ambient pressure. At a pressure of 16 bar coke formation can be avoided at temperatures higher than 1000 K and $H_2O/CH_4$ ratios higher than 1.25.

$$2CO \leftrightarrow C_s + CO_2 \tag{17}$$

Figure 9 shows the calculated syngas compositions, given for a $CH_4$-conversion of 99% at 1200 K reaction temperature. At ambient pressure almost complete conversion is achieved at the s/c-ratio of 1.25. This leads to a syngas that consists mainly of hydrogen and carbon monoxide with $H_2/H_2O$ and $CO/CO_2$ ratios of 14.8 and 20.2 respectively. At a pressure of 16 bar the s/c-ratio of 4 - 5 is necessary to achieve comparable conversion rates. This high s/c-ratio results in a syngas with much higher amounts of steam and carbon dioxide. Under these conditions the $H_2/H_2O$ and $CO/CO_2$ ratios are 0.9 and 1.3 respectively.
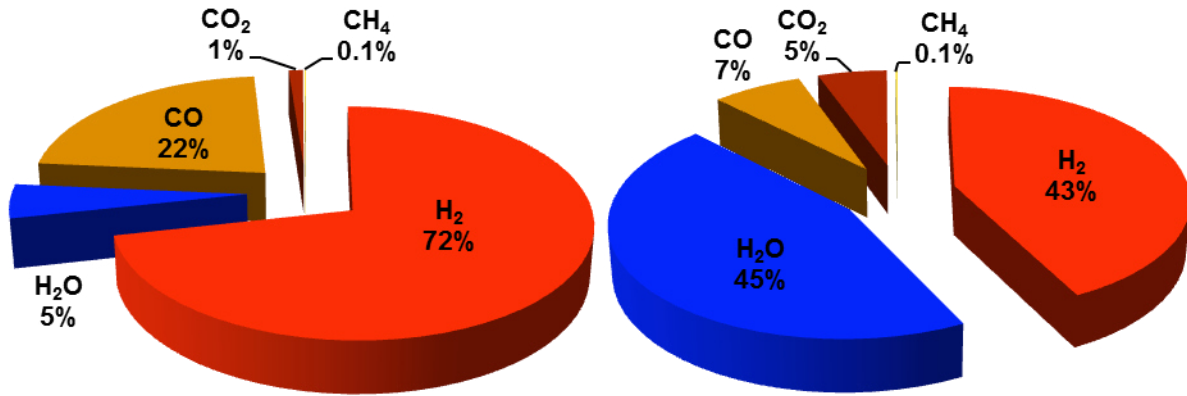
**Figure 9: Thermodynamic equilibrium concentration for ~99% CH$_4$-conversion at 1200 K; s/c=1.25 and 1.013 bar (left), at s/c=5 and 16.212 bar (right).**

In addition to the necessary dilution of the syngas at elevated pressure also the formation of CO and H$_2$O by the reversed water-gas shift reaction increases with pressure especially under conditions of a high CO$_2$ content such as dry-reforming. Oyama et al. investigated this effect in detail and pointed out that at elevated pressure the reversed water-gas shift reaction starts to dominate the dry reforming reaction and, therefore, CO and H$_2$O are produced [70]. Beside the negative effect of pressure on the thermodynamics of the reforming reaction also negative or at least non-positive kinetic effects of pressure on the reduction of iron based oxygen carriers for chemical looping combustion applications have been reported [58,71]. Therefore, syngas generation and reduction of the oxygen carrier at ambient pressure are clearly to favour.

### 2.4.2. Fixed bed reactor experiments

Figure 10 shows two reduction/oxidation cycles of the Fe$_2$O$_3$-Al$_2$O$_3$ sample. The reduction (a) showed three conversion levels which can be related to the different H$_2$/H$_2$O equilibrium concentrations for the reactions (7) - (9) [40,41]. The high conversion rate of almost 100% during the first 18 minutes was related to the reduction of Fe$_2$O$_3$ to Fe$_3$O$_4$. After the sharp drop of the conversion after 18 minutes, a non-stable H$_2$-conversion from minute 18 to minute 50 was measured. This region is related to the reduction from Fe$_3$O$_4$ to FeO. The fact that no stable conversion was measured might be related to a changing oxygen content of the non-stoichiometric compound FeO$_x$ which was formed and, therefore, changes the equilibrium concentrations. The stable conversion of 30% from minute 50 to minute 100 gives hint that the equilibrium concentration for the formation of Fe from FeO was reached in this period. From minute 100 to minute 200 the H$_2$ conversion slightly decreased which announced the end of the reaction. The very sharp decrease after 200 minutes signalised the

27

final step of the reduction and after 225 minutes only an insignificant low amount of hydrogen was converted. The consecutive oxidation which led to the formation of pressurised hydrogen is divided into three time periods. During the first period which ended after 50 minutes steam was fed into a closed system. Since a condenser removed the not reacted steam, which left the reactor, the pressure increase of the system was directly a function of hydrogen production. After 48 minutes a mass flow controller at the outlet of the condenser was opened in order to allow a constant $H_2$ volume flow of 10 ml·$min^{-1}$. During this period the pressure still increased from 9.5 bar(g) to 10.9 bar(g) which indicates a hydrogen production rate that is slightly higher than 10 ml·$min^{-1}$ and a steam conversion in the range of 21 - 30%. After 210 minutes the pressure decreased. This indicates a strong decrease of the amount of produced hydrogen and after 247 minutes the system pressure reached ambient conditions. The strong oscillation of the mass flow controller signal after 225 minutes is related to moisture reaching the device. For this reason only the first 225 minutes were used for the calculation of the amount of produced hydrogen. Since the oxidation with steam leads to the formation of magnetite, full hydrogen conversion according to reaction (7) could not be reached at reduction (b) but the oxidation showed the same rate of pressure increase as oxidation (a). Since the volume of the system is constant the pressure increase is directly related to the amount of produced hydrogen. Therefore, the constant rate of pressure increase also indicates a stable initial reactivity. Table 1 summarises the results of the series. The amount of produced or consumed hydrogen was calculated directly from the measured volume flows. The oxygen carrier conversion ($OC_{con}$) was calculated via Eq. (18) where $\Sigma H_2$ represents the molar amount of produced or consumed hydrogen, $n_{Fe}$ represents the molar amount of iron in the oxygen carrier and $OS_{Fe}$ represents the oxidation state of iron in its oxidised form at the given reaction (3 for haematite 8/3 for magnetite).

$$OC_{con}=\Sigma H_2/(0.5·n_{Fe}·OS_{Fe}) \tag{18}$$

At the first reduction, when haematite was present, 86 mmol of hydrogen were consumed which is equivalent to an oxygen carrier conversion of 84%. The consecutive oxidation led to the formation of 79 mmol of hydrogen which is equivalent to an oxygen carrier conversion of 87% to magnetite. A significant decrease of the amount of consumed or produced hydrogen from oxidation (a) to (b) is obvious and probably related to the sintering of the iron particles due to thermal stress.
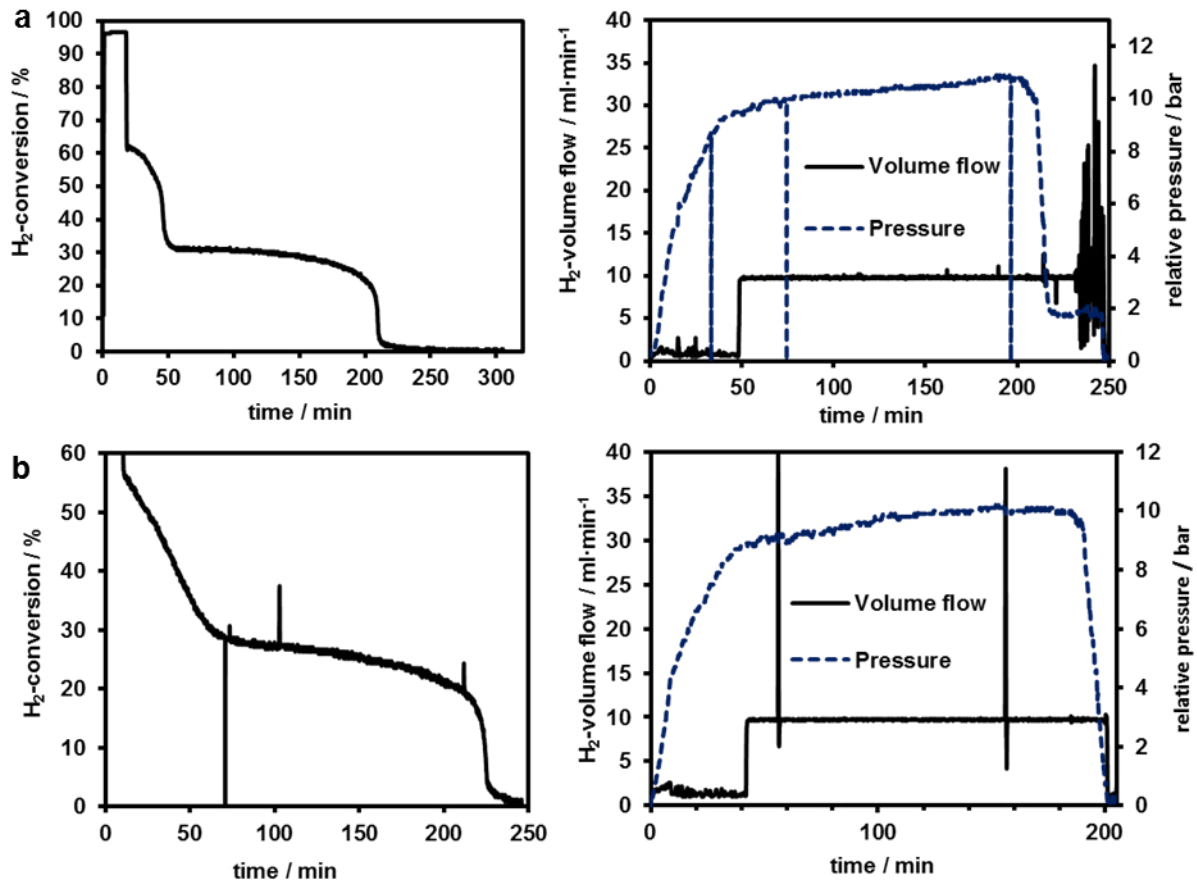
**Figure 10: Hydrogen conversion during the reduction (left), hydrogen-volume flow and pressure during the steam-oxidation (right) of the Fe$_2$O$_3$-Al$_2$O$_3$ sample.**

The slightly higher oxygen carrier conversions for the oxidation reactions compared to the corresponding reductions are in the range of 1 - 3% and can be seen as the error of measurement. The measurement of hydrogen with thermal mass flow controllers can be influenced by small amounts of moisture in the product gas which leads to a slightly higher amount of measured hydrogen during oxidation.

**Table 1: Experimental results of two reduction/oxidation cycles.**

| Reaction | OS$_{Fe}$ | ΣH$_2$ / mmol | OC$_{con}$ / % |
|----------|-----------|---------------|----------------|
| Reduction a | 3 | 86 | 84 |
| Oxidation a | 8/3 | 79 | 87 |
| Reduction b | 8/3 | 71 | 78 |
| Oxidation b | 8/3 | 72 | 79 |

Since it is reported that oxidation with air can have a positive effect on the stability of iron based oxygen carriers modified with Al$_2$O$_3$, such a step was performed prior to the reduction with synthesis gas [72]. Figure 11 shows the reduction of the air-oxidised oxygen carrier with

a dry synthesis gas mixture consisting of $H_2$, CO, $CO_2$ and $N_2$ followed by the oxidation with steam and $N_2$. Nitrogen was present during these experiments for analytic purpose and acted as an internal standard. Due to the higher overall gas flow and the presence of additional species this reduction experiment showed a different course as prior ones. It also has to be mentioned that the gas composition was measured using a micro gas chromatograph with a measuring interval of 3 minutes. Therefore, no region of 100% $H_2$- and CO-conversion was visible. However, the reduction experiment can be divided into four regions (a-d). In region (a) high amounts of hydrogen and carbon monoxide were converted (53% and 41%). This maximum conversion strongly decreased during the first 50 minutes. The hydrogen conversion reached an almost stable plateau between minute 50 and 150 in region (b) where it only decreased from 32% to 27% before a stronger decrease in region (c) to a final value of 13% in region (d) occurred. Carbon monoxide conversion showed a continuous decrease and after about 100 minutes a net production of carbon monoxide was measured while hydrogen and carbon dioxide were consumed. After 258 minutes the gas stream was switched to the bypass mode.
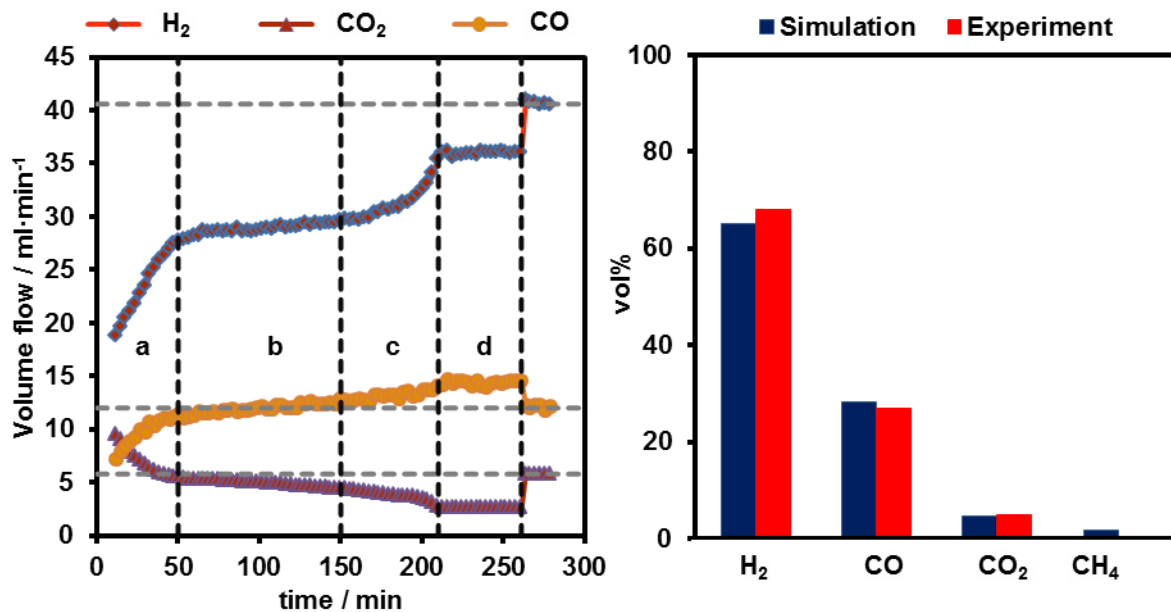


**Figure 11: Volume flow vs. time during the reduction experiment; vertical lines indicate different reaction periods, horizontal lines indicate the inlet flows (left), comparison of the measured dry gas flows in region (d) with the calculated equilibrium composition.**

The facts that stable hydrogen and carbon dioxide conversion as well as carbon monoxide production took place give raise to the assumption that side reactions occur, possibly catalysed by the oxygen carrier or the nickel based reactor itself. Three reactions, the reversed water-gas shift reaction (Eq. (19)), methanation (Eq. (20)) and coke formation (Eq. (21)) seem imaginable.

$$CO_2 + H_2 \rightarrow CO + H_2O \tag{19}$$

$$CO_2 + 4H_2 \rightarrow CH_4 + 2H_2O \tag{20}$$

$$CO + H_2 \rightarrow C_s + H_2O \tag{21}$$

The reversed water-gas shift reaction (19) which is favoured at high temperatures would lead to an increased amount of carbon monoxide by the conversion of hydrogen and carbon dioxide. The formation of methane (20) was measured during the reduction but its concentration was too low for quantification. Figure 11 shows the dry gas composition at the end of the reduction step which is in good accordance with the equilibrium composition calculated with the commercial software HSC chemistry 5.11 (Outokumpu). Although the formation of solid carbon was not predicted by the thermodynamic equilibrium calculations it occurred since the consecutive steam-oxidation lead to the formation of small amounts of carbon dioxide. The reaction was performed at 8 bar(g) and is presented in Figure 12.
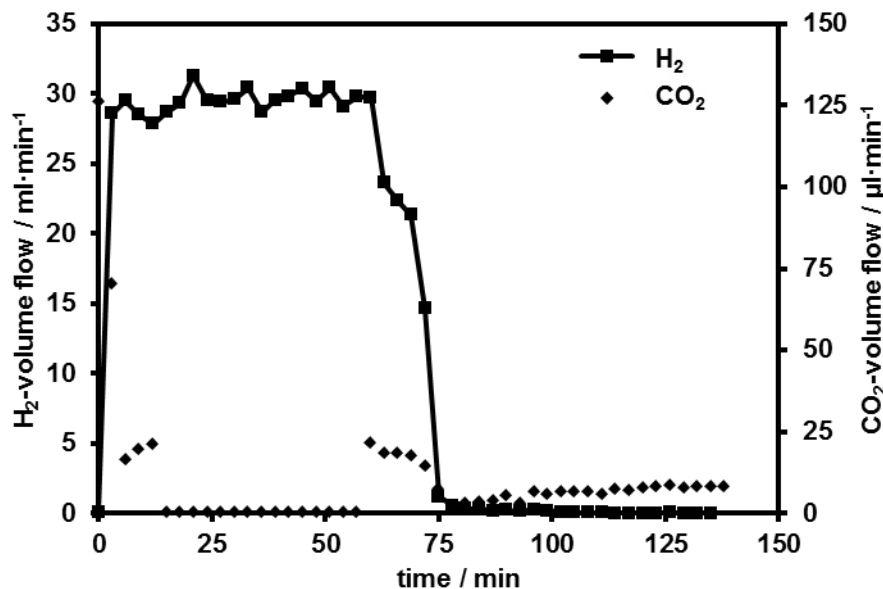


**Figure 12: Hydrogen and $CO_2$-volume flows during the steam-oxidation of a syngas reduced oxygen carrier vs. time; p=8 bar(g).**

The amount of produced hydrogen was 90 mmol which equals an oxygen carrier conversion of 99% and indicates a complete conversion during the prior reduction. The high oxygen carrier conversions gives hint to a regeneration effect caused by air-oxidation but additional experimental work is necessary to proof this. Carbon deposition during the reduction was detected during the oxidation, as $CO_2$ was produced by the steam-oxidation of solid carbon. The formation of solid carbon during the reduction is influenced by the reaction temperature. Therefore, the inlet and outlet regions of the reactor, where heating might be insufficient, are probably the regions with the highest amount of solid carbon. In this case the $CO_2$ produced during the first 15 minutes may be formed by the oxidation of solid carbon located at the inlet section of the reactor. At this point solid carbon which is located near the outlet section of the

reactor is not oxidised in measurable quantities since most of the steam is converted to hydrogen before it reaches this carbon containing region of the reactor. At the end of the oxidation phase, when most of the iron is already oxidised, more steam reaches the outlet region of the reactor and, therefore, a second phase of $CO_2$ formation is possible. An overall concentration of 700 ppm carbon dioxide was measured, while no signs of carbon monoxide were detected which illustrates the feasibility of the process for the production of hydrogen for fuel cell applications.

### 2.4.3. Thermogravimetric analysis

Figure 13 indicates moderate deactivation behaviour of the analysed oxygen carrier at 1023 K. The mass change between the reduced and oxidised state of the oxygen carrier is directly related to its conversion during the corresponding reaction. The mass change in the second cycle was 23% and decreased to 21% in the last cycle which equals a deactivation of 9% over 9 cycles. The constant decrease was mainly visible during the reduction period while no clear trend was visible during the steam-oxidation phase. One can say that with increasing cycle number the oxygen carrier cannot be fully reduced anymore and, therefore, also less hydrogen will be released during the consecutive oxidation.
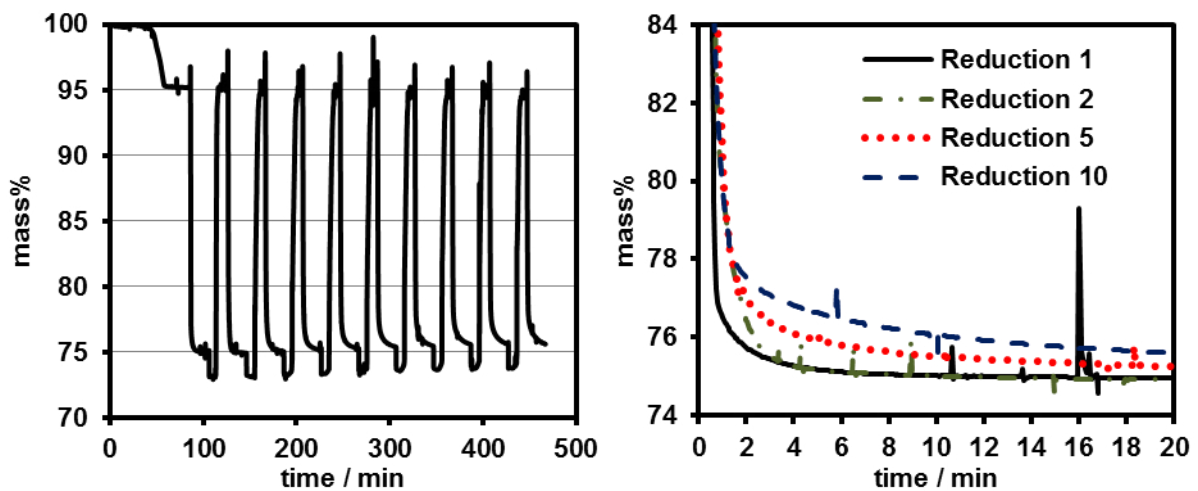


**Figure 13: Reduction and oxidation behaviour over 9 cycles of the Fe$_2$O$_3$-Al$_2$O$_3$ sample (left), detailed illustration of 4 reduction steps to point out the slowdown of reaction rate during the reduction reaction (right).**

### 2.4.4. Scanning electron microscopy

Figure 14 shows images of the fresh oxygen carrier (a) after 4 fixed bed reactor cycles (b, c and d) as well as an identical sample after 9 cycles in the thermogravimetric analysis system (e, f) at 1023 K each. Energy-dispersive X-ray spectroscopy (EDX) revealed regions of

almost pure $Fe_xO_y$ (region ux8930) and regions of almost pure $Al_2O_3$ (region ux8929) at image (b).
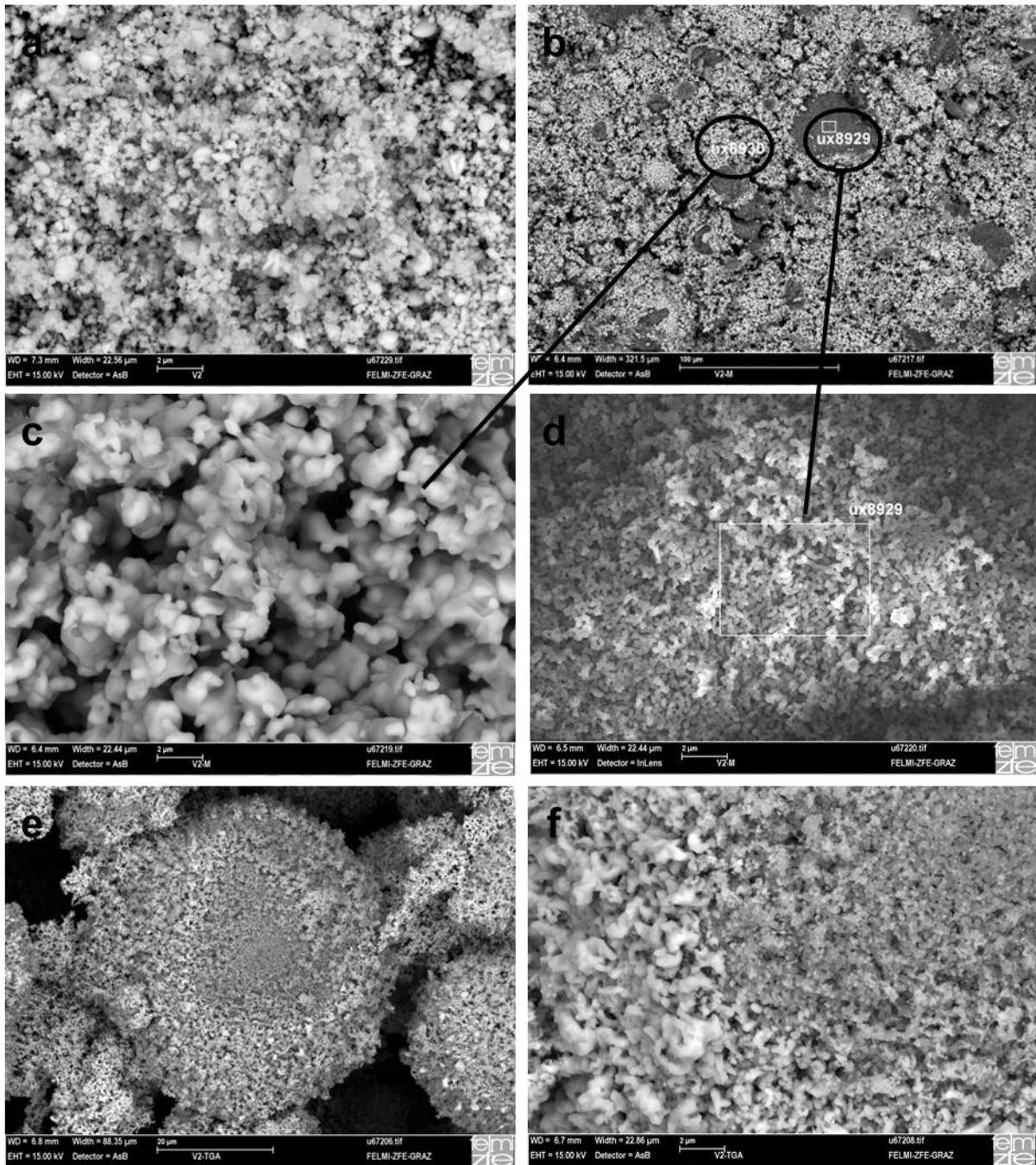


**Figure 14: SEM images of a fresh $Fe_2O_3$-$Al_2O_3$ sample (a) after four cycles in the fixed bed reactor (b, c and d) and after 9 cycles in the thermogravimetric analysis system (e and f).**

A comparison between region ux8930 (image c) and ux8929 (image d) shows a clear difference in the surface morphology between the $Al_2O_3$ area (d) and the $Fe_xO_y$ area (c). Images (e) and (f) clarify the existence of separate regions. A detector for backscattered electrons where aluminium appears darker compared with iron, due to the higher atomic mass of the latter, was used in order to distinguish between $Al_2O_3$ and $Fe_2O_3$ regions. $Al_2O_3$ is well known to improve the stability of iron based oxygen carriers but due to the preparation

technique of mechanical mixing this stabilisation effect is limited because of not ideal mixing of $Al_2O_3$ and $Fe_2O_3$ powder. Measurements by the BET-method revealed a decrease of the surface area from 7.5 $m^2 \cdot g^{-1}$ to 0.9 $m^2 \cdot g^{-1}$ after the fixed bed reactor experiments at 1023 K. The decrease of the surface area of a fresh sample (a) compared with the iron rich regions of the reacted oxygen carrier in (c) is clearly visible. Despite this decrease of the surface area only moderate deactivation was measured in the TGA and almost complete oxygen carrier conversion was achieved during the last oxidation cycle in the fixed bed reactor. Figure 14 (c) indicates that the porosity of the prepared oxygen carrier was preserved at a micrometre scale and is, therefore, still high enough to achieve this good conversion rates. Such an effect was also reported by Liu, Dennis and Scott for $ZrO_2$-based oxygen carriers [73].

### 2.4.5. Summary and conclusion

A thermodynamic analysis of the methane decomposition reaction has shown that the formation of solid carbon is unavoidable if iron oxide is reduced with pure methane, at fixed bed operation over the whole investigated temperature and pressure range. Therefore, a syngas generation step has to be conducted in order to produce pure hydrogen by the steam iron process. This syngas generation step was evaluated at different pressure levels. The generation of a syngas with high amounts of carbon monoxide and hydrogen but low amounts of excess steam and carbon dioxide is not possible at elevated pressure. For CLC-applications, where the focus lies on efficient $CO_2$-recovery, reduction at elevated pressure might be to favour but for the reformer-steam iron process it has to be avoided. From a thermodynamic point of view the operation pressure has to be as low as possible in order to reach high conversion rates and a favourable product distribution. Therefore, the separation of fixed-bed chemical looping hydrogen production into an ambient pressure reforming/reduction step and a high pressure oxidation step as an ideal process for the decentralised production of pure pressurised hydrogen is proposed. Reduction experiments with pure hydrogen as well as with a syngas mixture showed the feasibility of the developed process for pressurised hydrogen production. A reduction experiment carried out using a syngas mixture led to the formation of hydrogen of high purity after the steam-oxidation step. An overall amount of 700 ppm carbon dioxide but no traces of carbon monoxide were detected. Stable hydrogen flow rates at 8 – 10 bar were achieved and showed the potential of the process for the production of pressurised hydrogen. Although a significant loss of active surface was observed, by BET and SEM characterisation, only moderate deactivation was measured in the TGA and fixed bed reactor system. These auspicious results clearly show the potential of the process for the decentralised production of pressurised hydrogen of highest purity without the need for additional compression and purification steps. The

potential of this process is extremely high and recently hydrogen pressure levels of up to 22 bar(g) were demonstrated by Voitic and the author [74].

# 3. Steam reforming of methane and biogas

Ruthenium and nickel based catalysts were used for screening experiments in order to investigate their capability for steam reforming of methane and biogas. The main purpose of these measurements was to answer the question if commercial SMR catalysts can be used for biogas reforming. Thermodynamic calculations were carried out in order to evaluate the gained data and to determine feasible operation conditions. The results of the reforming experiments using the ruthenium based catalyst were presented at the annual meeting of the American Institute of Chemical Engineers (AIChE) in 2012 [75].

## 3.1. Thermodynamic evaluation of hydrogen production

The commercial software HSC chemistry 5.11 (Outokumpu) was used to investigate the product distribution under different temperatures and steam to carbon ratios at ambient pressure by minimising the free Gibbs energy of the system. The aim of these simulations was to determine the effect of temperature and steam to carbon ratio on SMR and biogas reforming. The preliminary thermodynamic analysis helped to avoid unnecessary experimental effort and gave more detailed understanding of the reforming process. Figure 15 represents the calculated product distribution of the steam reforming process using methane and biogas (50 mol% methane + 50 mol% carbon dioxide) as a function of temperature and s/c-ratio. Methane, hydrogen, steam, carbon monoxide, carbon dioxide and solid carbon were considered as possible products.

It is obvious that at s/c=0 and at low temperatures almost no $CH_4$-conversion occurs when only methane is present (Figure 15 a). At elevated temperatures the methane decomposition reaction Eq. (16) becomes dominant and at a temperature above 850 °C almost complete conversion occurs. Methane decomposition is an interesting process for hydrogen production since it enables the production of pure hydrogen and avoids any risk of carbon monoxide impurities as well as carbon dioxide emissions [62,76]. On the other hand, the formation of solid carbon makes this process unusable for the generation of reductive species for the steam iron process. In the case of biogas (Figure 15 b), due to the presence of carbon dioxide and the dry reforming reaction (Eq. (22)), higher amounts of methane are converted to steam and solid carbon at low temperatures. At this point it has to be mentioned that the calculated results only represent the thermodynamic equilibrium which can be seen as the boundaries of the system.
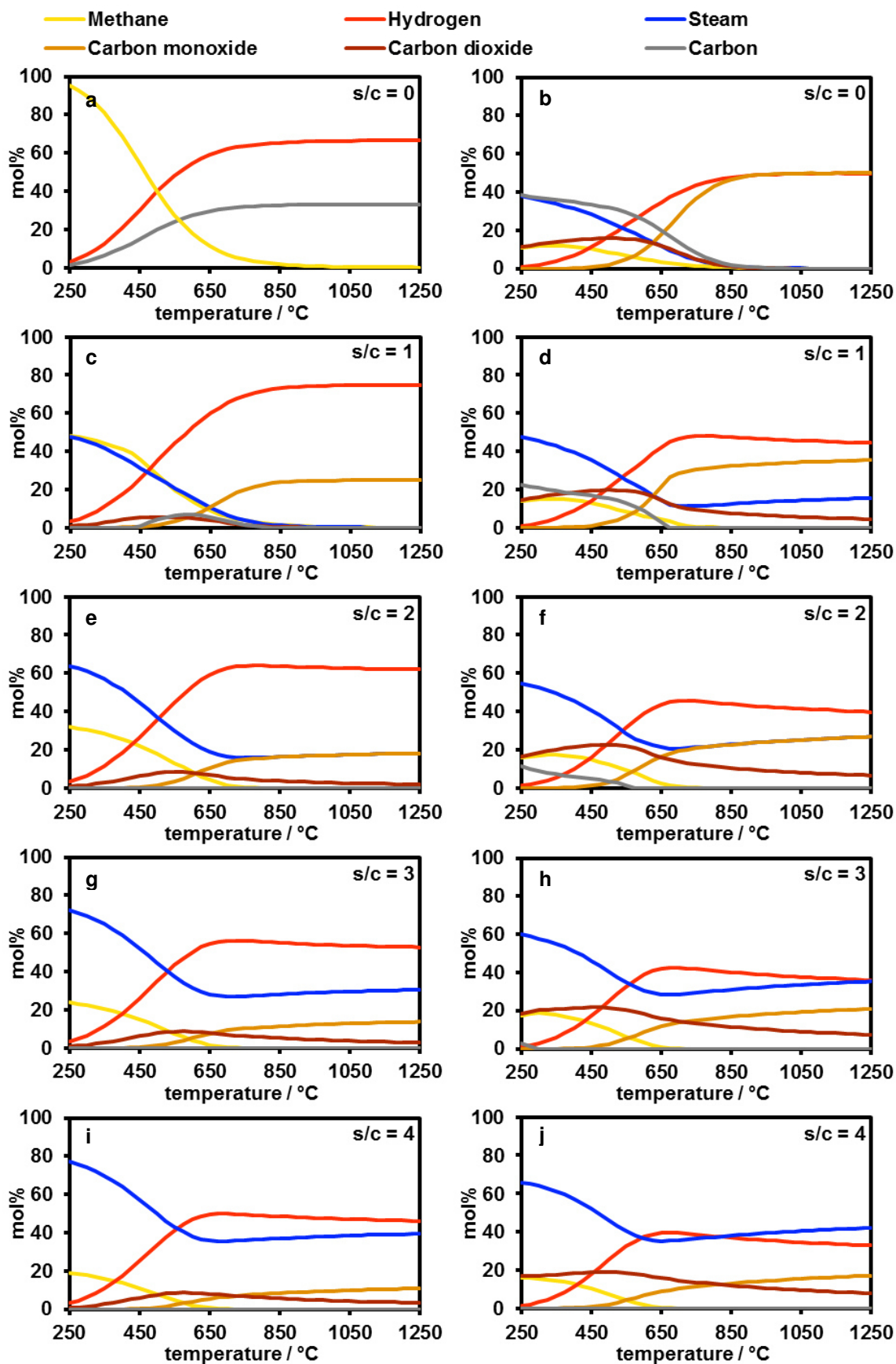
$$CH_4 + CO_2 \rightarrow 2H_2 + 2CO \tag{22}$$

**Figure 15: Product distribution of steam reforming of methane (left) and biogas (right) as a function of temperature and s/c-ratio.**

The composition given in Figure 15 b suggests that mixtures of methane and carbon dioxide decompose already at a moderate temperature of 250 °C and form steam and carbon. This, of course, completely ignores kinetics and, therefore, only represents the behaviour of the system after an infinite time span. Nevertheless, especially at higher temperatures when kinetic limitations become less dominant the calculations can give valuable information. If the measured gas composition is in accordance with the thermodynamic calculations the investigated catalyst can be seen as reactive enough to achieve the maximum conversion rate under the given conditions. Steam methane reforming (Figure 15 c, e, g, and i) is strongly influenced by temperature and s/c. Due to the endothermic nature of the process high temperatures shift the equilibrium towards higher methane conversion rates and, therefore, higher hydrogen production. At a certain temperature the reversed water-gas shift reaction becomes dominant and reduces the amount of produced hydrogen by increasing the amount of steam and carbon monoxide in the product gas. High amounts of steam increase the methane conversion especially at lower temperatures and avoid the formation of solid carbon. At s/c-ratios above 2, from a thermodynamic point of view, a carbon free operation is possible. Due to the higher overall amount of carbon species during steam reforming of biogas (Figure 15 d, f, h, and j) a higher amount of carbon monoxide is present in the syngas and the risk of coke formation is higher. At s/c=1 a temperature of 650 °C is necessary for carbon free operation, at s/c=2 the minimum temperature decreases to 550 °C. In terms of methane conversion a minimum temperature of at least 650 °C and a minimum s/c-ratio of 2 were identified for efficient processing of pure methane and biogas. On the other hand, temperatures above 750 °C and a s/c-ratio above 4 seems unnecessary since even the difference between s/c=3 and s/c=4 is negligible at appropriate temperature conditions. Therefore, temperatures of 650 °C, 700 °C and 750 °C as well as s/c-ratios of 2, 3 and 4 were chosen for the catalyst screening experiments.

## 3.2. Screening of Nickel and Ruthenium based catalysts

### 3.2.1. Experimental

Nickel and ruthenium based catalysts were used for screening experiments in order to investigate their capability for steam reforming of methane and biogas. The commercial catalyst FCR-70, kindly provided by Clariant International Ltd., is a nickel based catalyst immobilised on a mixture of strontium oxide, aluminium oxide and calcium aluminate. The pelletised catalyst was crushed and fractionised prior to the reforming experiments. 0.93 g of the 180 - 250 µm fraction of the catalyst was used for the experiments. The catalyst was reduced in a stream of 35 ml·min$^{-1}$ H$_2$ and 45 ml·min$^{-1}$ N$_2$ at 700 °C for 2 hours. 1.05 g of the 5% Ru/Al$_2$O$_3$ catalyst, kindly provided by ITRI-Taiwan, was used in pelletised form. Prior to

the reforming experiments the catalyst was reduced in a stream of 50 ml·min$^{-1}$ H$_2$ and 50 ml·min$^{-1}$ N$_2$ at 700 °C for 2 hours. The reforming reactions were carried out at temperatures between 650 °C and 750 °C, at steam to carbon ratios of 2, 3 and 4 and a CH$_4$ flow of 30 ml·min$^{-1}$. For the biogas reforming experiments a 1+1 mixture of CH$_4$ and CO$_2$ was used. The total flow was kept constant for all measurements at 210 ml·min$^{-1}$ by varying the N$_2$ flow. The N$_2$ flow was also used as an internal standard to calculate the gas flow of the products and the CH$_4$-conversion. The catalyst tests were performed using the microactivity-reference unit (PID Eng&Tech) already described in section 2. A steam generator (aDROP) was used for producing a constant steam flow. The dry gaseous products of the reaction were analysed with a micro gas chromatograph (Agilent 3000) every 3 to 4 minutes.

### 3.2.2. Results and discussion

The activity and the hydrogen production rate of the nickel and ruthenium catalysts were measured under different operation conditions. The results were calculated based on the measured gas concentrations at constant conditions. Figure 16 shows the measured gas flows at s/c=2 and 650 °C using the Ru/Al$_2$O$_3$ catalyst for steam reforming of methane as well as the calculated dry gas composition. It can be seen that after a short period of several minutes the gas flows are constant for the whole experiment. The dry gas composition was calculated from the averaged data excluding the first minutes of each experiment. Based on this data the CH$_4$-conversion was calculated using equation (23) with the inlet and outlet streams of CH$_4$ (CH$_{4, in}$ and CH$_{4, out}$). The hydrogen yield was calculated using equation (24) with the amount of produced hydrogen (H$_{2, out}$) and a stoichiometric factor (SF=4 for CH$_4$).

CH$_4$-conversion / % = 100*(CH$_{4, in}$ − CH$_{4, out}$)/CH$_{4, in}$          (23)

H$_2$-yield / % = 100*H$_{2, out}$/(CH$_{4, in}$ * SF)          (24)

The results of the SMR experiments using the ruthenium based catalyst in comparison to the values calculated via HSC-Chemistry 5.11 software are summarised in Table 2. The experimental results are in good accordance with the simulated ones. In general the measured CH$_4$-conversion is slightly lower than the calculated one which indicates a residence time which was too short to achieve the thermodynamic equilibrium. Only the experiments at s/c=2; 650 °C and 700 °C (a and b) show a slightly higher conversion rate than calculated. The reason for this deviating result might be found in an inaccurate water supply. As it can be seen in Figure 17 an increase of the s/c-ration from 2 to 3 significantly increases the CH$_4$-conversion at 650 °C and 700 °C. Therefore, even a minor oversupply with steam can cause a higher conversion than calculated.
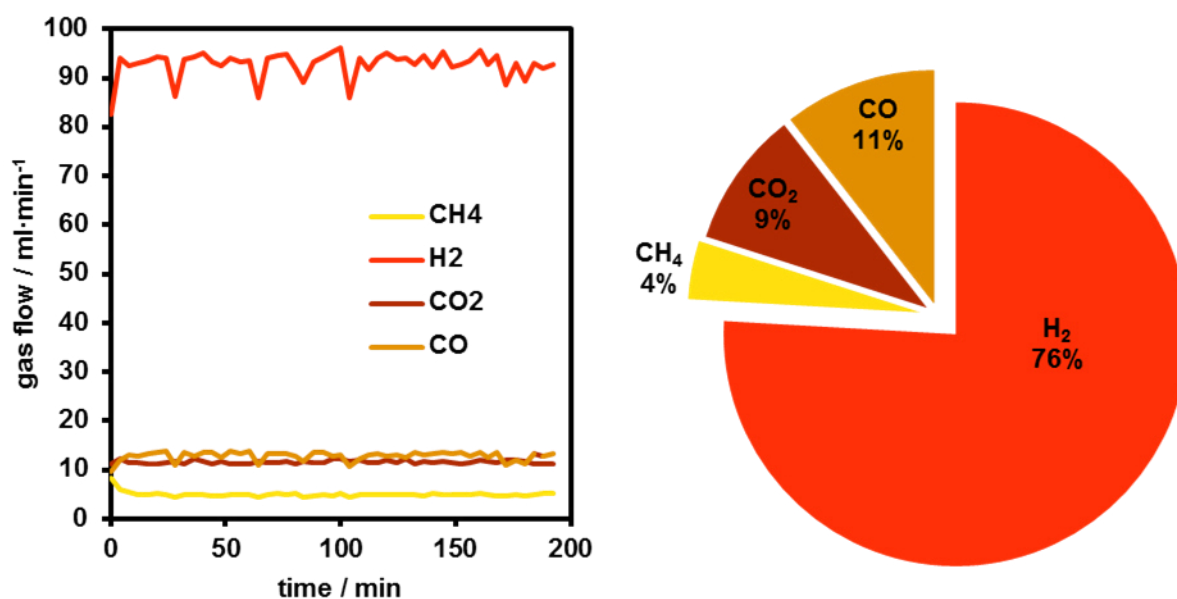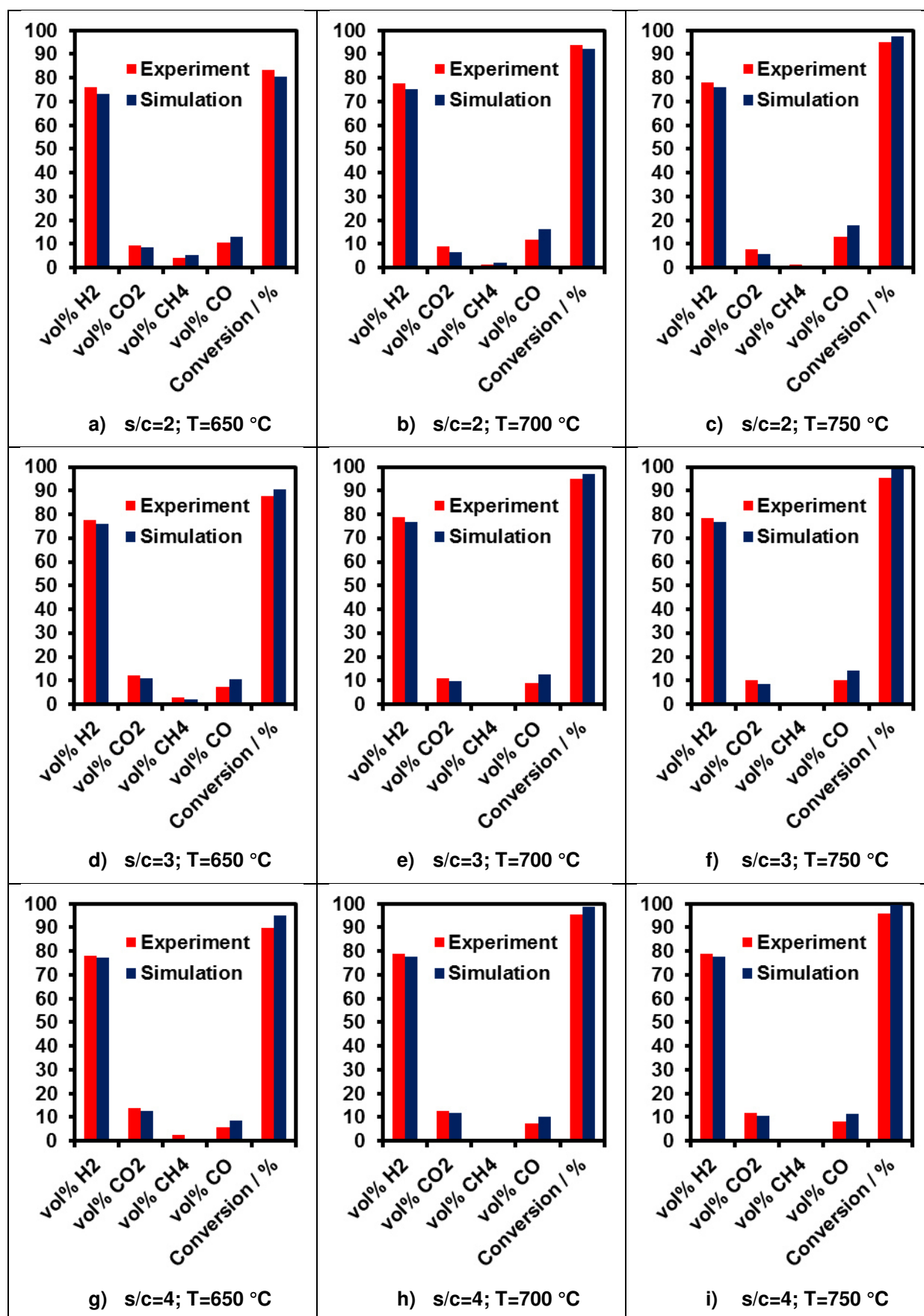
**Figure 16: Gas flow versus time (left) and composition of the gaseous products (right) for steam reforming of methane at s/c=2 and 650 °C.**

A general trend which can be observed in all experimental results is a higher amount of produced hydrogen than calculated. In all experiments more hydrogen and carbon dioxide than expected were produced while the amount of carbon monoxide was slightly below the equilibrium. This indicates a high water-gas shift activity in all experiments. Since low temperatures shift the equilibrium towards hydrogen and carbon dioxide a low temperature in the outlet section of the reactor might cause this result.

Table 3 summarises the results of the biogas reforming experiments for the ruthenium based catalyst in comparison to the values calculated via HSC-Chemistry 5.11 software. As observed for the SMR experiments the results are in good accordance with the calculations. All measurements show a slightly too low $CH_4$-conversion and a higher selectivity towards hydrogen and carbon dioxide. Due to the high initial amount of carbon dioxide also higher amounts of carbon monoxide and carbon dioxide are present in the product gas while the hydrogen content is lower compared to the dry SMR product gas.

**Table 2: CH₄-conversion and dry gas composition for steam reforming of methane using a Ru/Al₂O₃ catalyst.**



a)  s/c=2; T=650 °C

b)  s/c=2; T=700 °C

c)  s/c=2; T=750 °C

d)  s/c=3; T=650 °C

e)  s/c=3; T=700 °C

f)  s/c=3; T=750 °C

g)  s/c=4; T=650 °C

h)  s/c=4; T=700 °C

i)  s/c=4; T=750 °C

**Table 3: CH$_4$-conversion and dry gas composition for steam reforming of biogas using a Ru/Al$_2$O$_3$ catalyst.**



a) s/c=2; T=650 °C

b) s/c=2; T=700 °C

c) s/c=2; T=750 °C

d) s/c=3; T=650 °C

e) s/c=3; T=700 °C

f) s/c=3; T=750 °C

g) s/c=4; T=650 °C

h) s/c=4; T=700 °C

i) s/c=4; T=750 °C
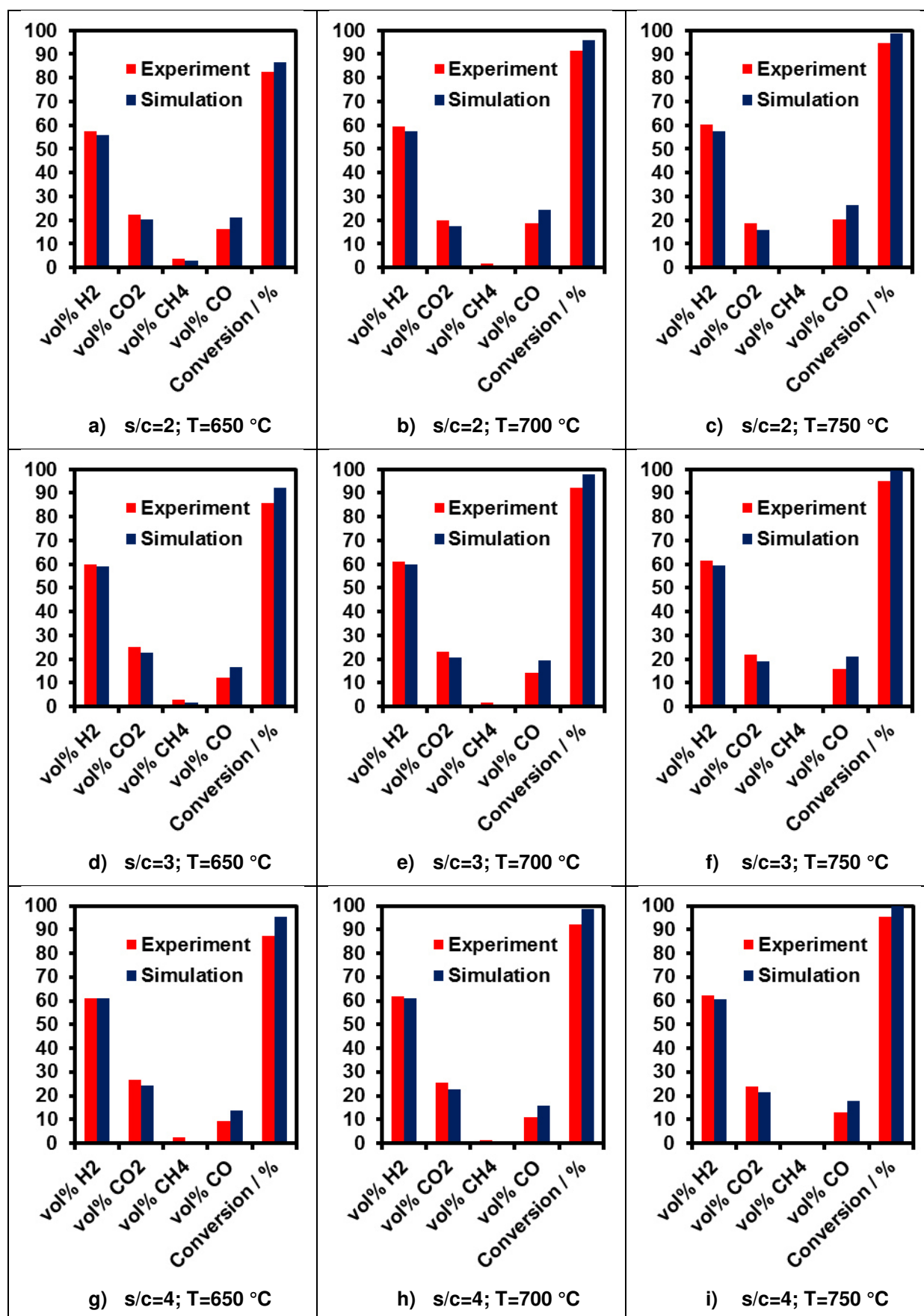
Figure 17 shows the comparison of $CH_4$-conversion by SMR and biogas reforming. At low temperatures and s/c-ratios, the conversion of biogas was lower than for pure methane. Especially at 650 °C the s/c-ratio strongly influenced the $CH_4$-conversion. An increase of the s/c-ratio from 3/1 to 4/1 at 700 °C did not lead to a significant increase of $CH_4$-conversion during SMR. At 750°C the conversion reached a maximum of 95% for each steam to carbon ratio (Figure 17-left). During the reforming of biogas, $CH_4$-conversion at lower temperatures was below the conversion of pure $CH_4$ but also reached a maximum of 95% at 750°C for each s/c-ratio (Figure 17-right).
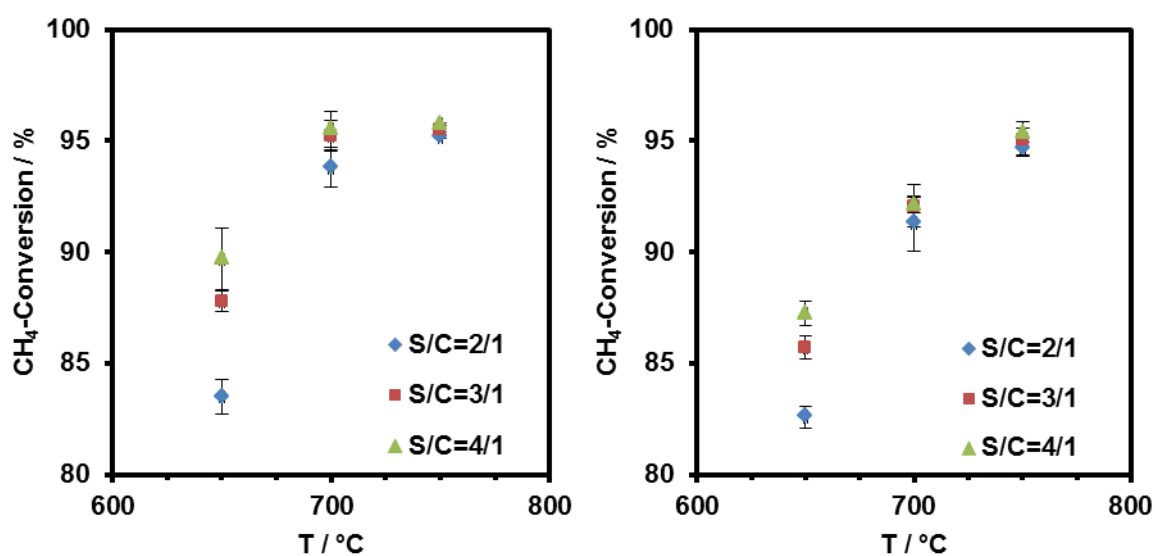


**Figure 17: $CH_4$-conversion during methane reforming (left) and biogas reforming (right) at different temperatures (T) and s/c-ratios, using a ruthenium based catalyst.**

While the effect of the s/c-ratio at temperatures of 700 °C and above was low for $CH_4$-conversion the hydrogen production rate was strongly influenced. During the SMR experiments a change of the s/c-ratio from 2/1 to 3/1 led to a strong increase in the hydrogen production rate at each temperature (Figure 18-left). A further increase of the s/c-ratio showed no significant effect on the hydrogen production rate at temperatures of 700 °C and 750 °C. For biogas reforming the influence of the steam to carbon ratio on the hydrogen production rate was high for each temperature (Figure 18-right). This can be explained by the higher amount of $CO_2$ in the product gas and therefore, the greater importance of the reversed water gas shift reaction. The reversed water gas shift reaction also leads to a slight decrease of the hydrogen production rate at 750°C during SMR. Based on theoretically possible 120 ml·min$^{-1}$, maximum hydrogen yields of 89% for SMR and 83% for biogas reforming were reached.
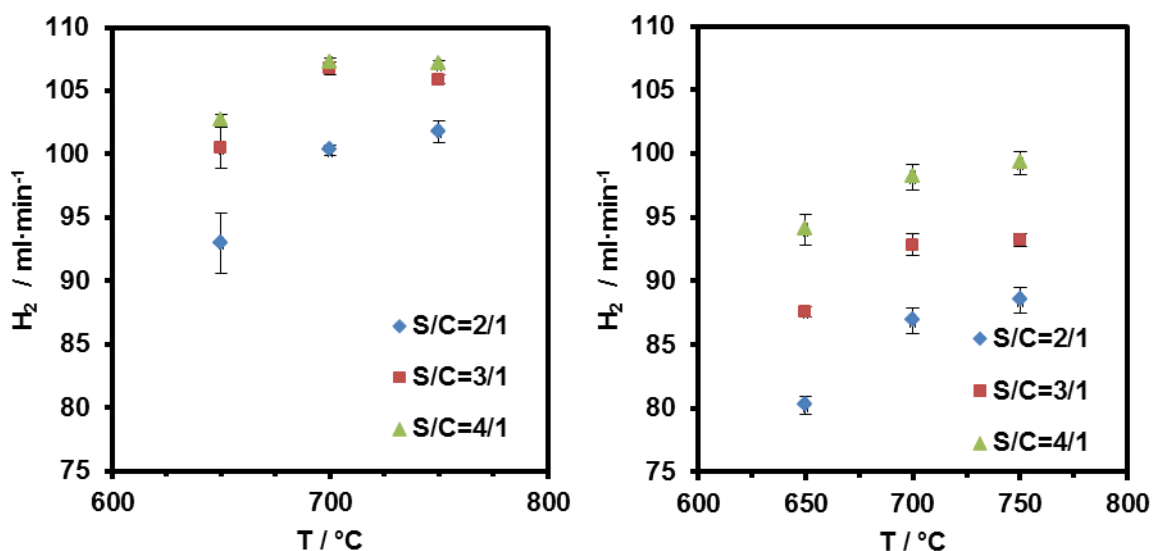
**Figure 18: H₂ production rate from SMR (left) and simulated biogas reforming (right) at different temperatures (T) and s/c-ratios, using a ruthenium based catalyst.**

Table 4 summarises the results of the SMR experiments for the nickel based catalyst in comparison to the values calculated via HSC-Chemistry 5.11 software. The $CH_4$-conversion is always significantly below the calculated values. Minor deviations from the simulated dry gas composition are also clearly visible. All experiments show an increased amount of carbon dioxide while carbon monoxide is decreased. This indicates a high water-gas shift activity of the catalyst. The fact that the hydrogen amount in the product gas is below the calculated value, while carbon dioxide is above, can be explained by the low $CH_4$-conversion. While the water-gas shift reaction increases the amount of produced hydrogen a major share of hydrogen is still chemically bound as methane and, therefore, the hydrogen concentration of the dry gas is below the expectation.

Table 5 shows the $CH_4$-conversion as well as the dry gas composition of the biogas steam reforming experiments in comparison to the simulated values. Following the trend of the SMR experiments also during biogas reforming a $CH_4$-conversion below the thermodynamic equilibrium is obvious. High amounts of carbon dioxide and low amounts of carbon monoxide also indicate high water-gas shift activity during biogas reforming using the nickel based catalyst.

**Table 4: CH$_4$-conversion and dry gas composition for steam reforming of methane using a Ni-based catalyst.**



a)  s/c=2; T=650 °C

b)  s/c=2; T=700 °C

c)  s/c=2; T=750 °C

d)  s/c=3; T=650 °C

e)  s/c=3; T=700 °C

f)  s/c=3; T=750 °C

g)  s/c=4; T=650 °C

h)  s/c=4; T=700 °C

i)  s/c=4; T=750 °C
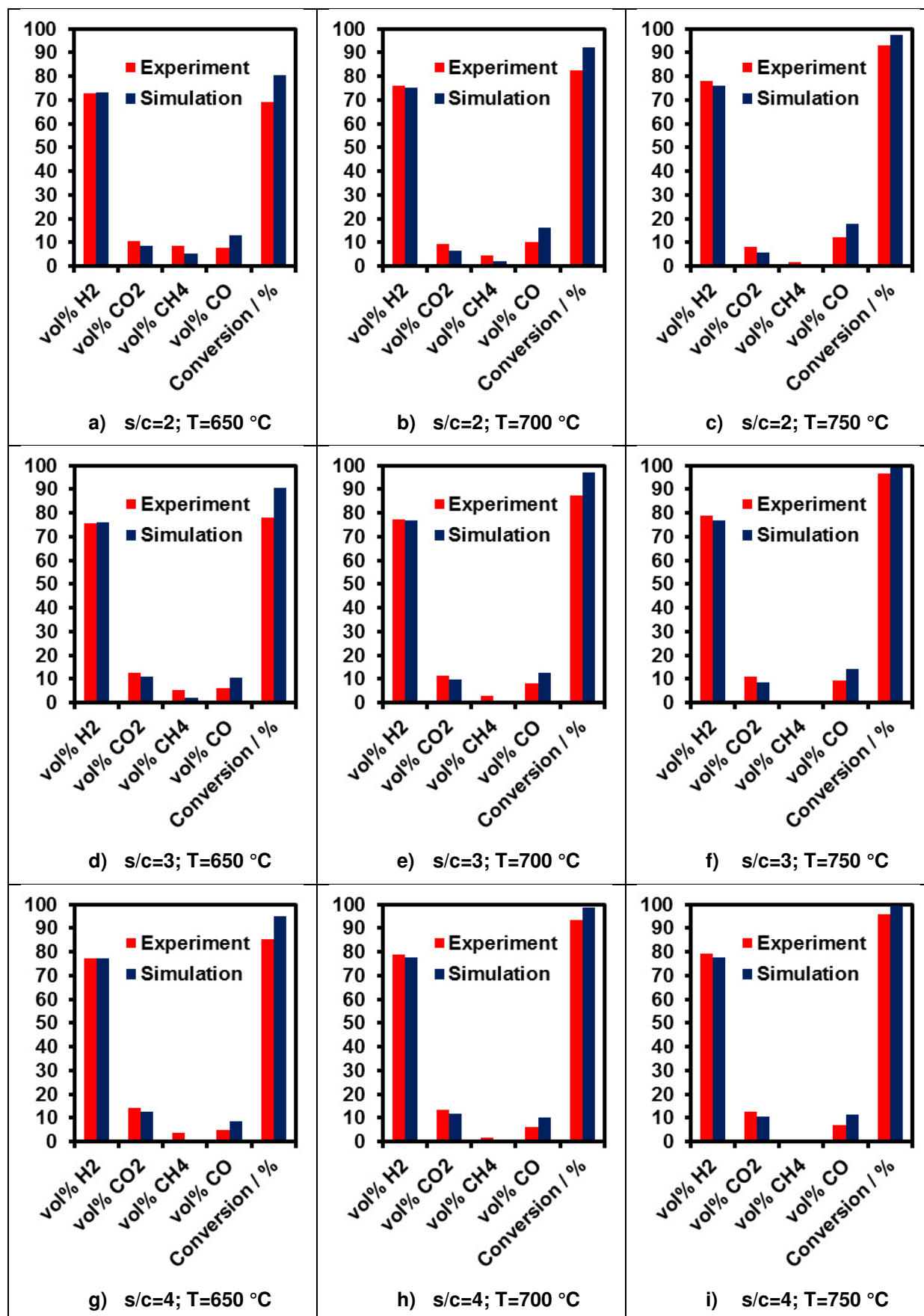
**Table 5: CH$_4$-conversion and dry gas composition for steam reforming of biogas using a Ni-based catalyst.**



a)   s/c=2; T=650 °C

b)   s/c=2; T=700 °C

c)   s/c=2; T=750 °C

d)   s/c=3; T=650 °C

e)   s/c=3; T=700 °C

f)   s/c=3; T=750 °C

g)   s/c=4; T=650 °C

h)   s/c=4; T=700 °C

i)   s/c=4; T=750 °C
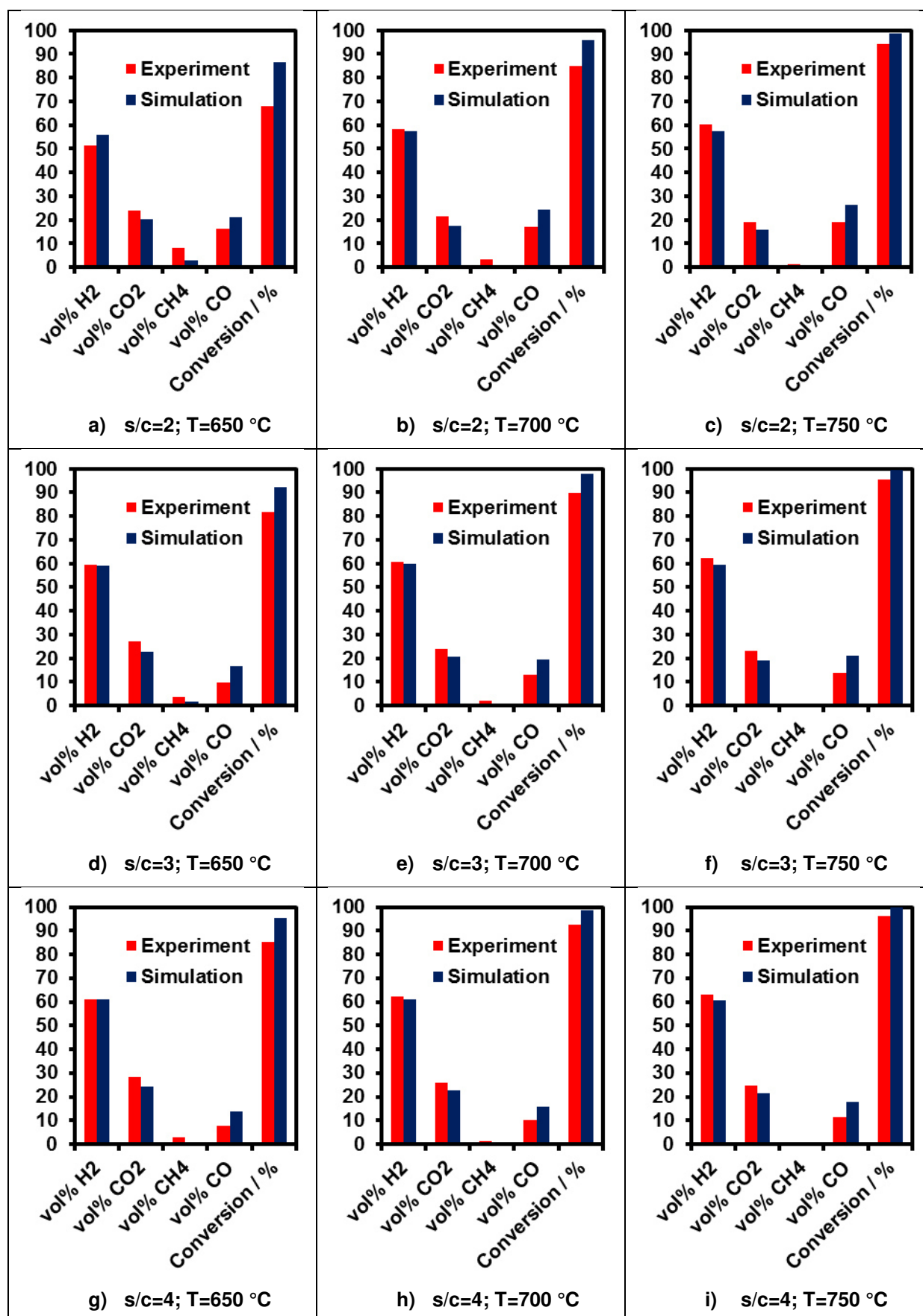
Figure 19 shows a distinct increase of the $CH_4$-conversion with temperature. At 650 °C and 700 °C also an increase of the s/c-ratio led to increased conversion. At 750 °C, an increase of the s/c-ratio from 3 to 4 did not lead to a higher conversion during methane reforming. During biogas reforming no significant influence of the s/c-ratio at all was measured at 750 °C. No clear difference in terms of $CH_4$-conersion can be seen between methane and biogas reforming and a maximum conversion of 96% - 97% was achieved at 750 °C for biogas and pure methane.
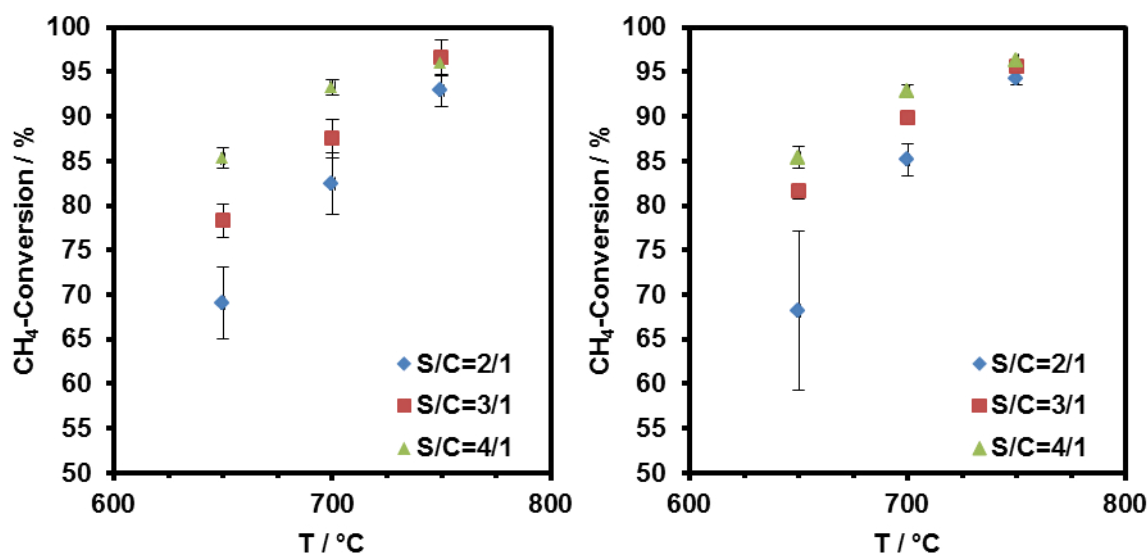


**Figure 19: $CH_4$-conversion during methane reforming (left) and biogas reforming (right) at different temperatures (T) and s/c-ratios, using a nickel based catalyst.**

Using the nickel based catalyst the difference between measured and simulated $CH_4$-conversion decreased with increasing temperature at all investigated parameters while no such a clear trend was found for the ruthenium based catalyst. Assuming that the simulation is correct the decreasing deviation can be explained with low kinetics respectively a too low residence time at the given temperature. At lower temperatures the kinetics of the nickel based catalyst are too low to achieve the equilibrium while at higher temperatures the kinetics are high enough to achieve almost the thermodynamic limit of the reaction. As it can be seen in Figure 20, hydrogen production increases with the temperature and the s/c-ratio. For SMR the influence of the s/c-ratio on the hydrogen production is almost the same as on the $CH_4$-conversion and decreases with increasing temperature (Figure 20-left). For biogas reforming the s/c-ratio shows a higher influence on hydrogen production also at 750 °C (Figure 20-right). Hydrogen production during biogas reforming was always lower than during SMR but the difference decreases with increasing temperature and s/c-ratio as it is in accordance with thermodynamic calculations. A maximum flow of 108 ml·min⁻¹ hydrogen ($H_2$-yield=90%), was achieved for SMR while the maximum hydrogen flow was 102 ml·min⁻¹ ($H_2$-yield=85%) for biogas reforming.
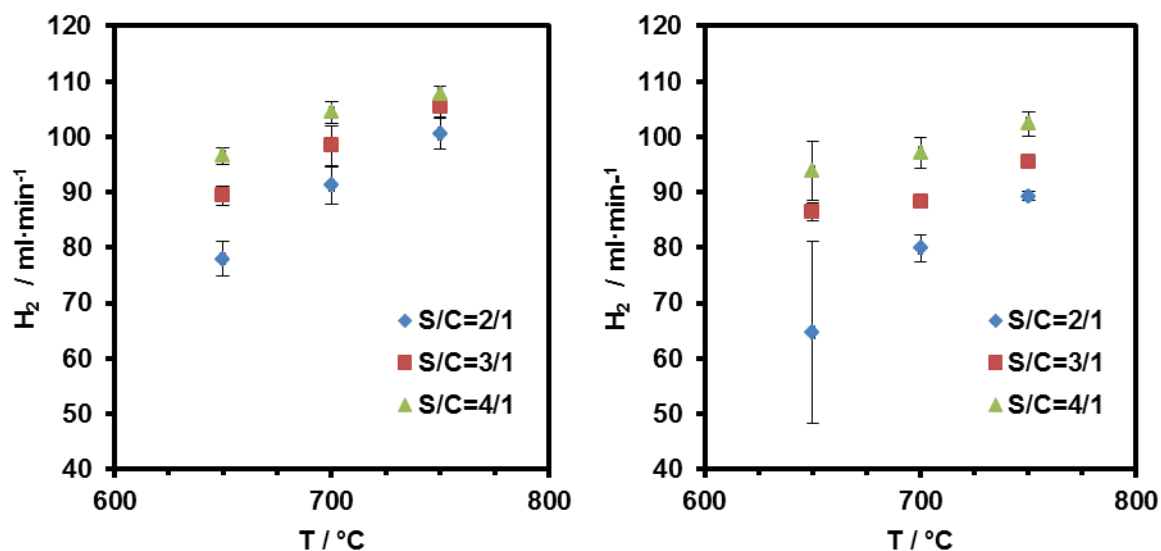
**Figure 20: H$_2$ production rate from SMR (left) and simulated biogas reforming (right) at different temperatures (T) and s/c-ratios, using a nickel based catalyst.**

### 3.2.3. Summary and conclusion

All measurements of the series in terms of CH$_4$-conversion are summarised in Table 6. The major findings are:

- The CH$_4$-conversion increases with temperature and s/c-ratio but the influence becomes less important at higher values. This is in good agreement with thermodynamic expectations.

- At low temperatures and s/c-ratios, the ruthenium based catalyst shows higher conversion rates than the nickel based one. This difference decreases with increasing temperature and s/c-ratio. At 750 °C the ruthenium based catalyst shows no clear advantage over the nickel catalyst in terms of reactivity.

- In general a higher reactivity was measured for the ruthenium based catalyst when pure methane instead of biogas was used as feedstock. For the nickel based catalyst no such a trend was found. Especially at low temperatures and s/c-ratios higher conversion were measured when biogas was used as feedstock.

**Table 6: Comparison of the CH$_4$-conversion of methane and biogas reforming using ruthenium and nickel based catalysts.**

| s/c | T / °C | CH$_4$-conversion / % | | | |
|-----|--------|----------|---------|---------|---------|
| | | methane | | biogas | |
| | | Ru-cat. | Ni-cat. | Ru-cat. | Ni-cat. |
| 2 | 650 | 83±1 | 69±4 | 83±0 | 68±9 |
| | 700 | 94±1 | 82±3 | 91±1 | 85±2 |
| | 750 | 95±0 | 93±2 | 95±0 | 94±1 |
| 3 | 650 | 88±0 | 78±2 | 86±1 | 82±1 |
| | 700 | 95±1 | 87±2 | 92±1 | 90±0 |
| | 750 | 95±0 | 97±2 | 95±1 | 96±0 |
| 4 | 650 | 90±1 | 85±1 | 87±1 | 85±1 |
| | 700 | 96±1 | 93±1 | 92±0 | 93±1 |
| | 750 | 96±0 | 96±0 | 95±0 | 96±0 |

All measurements of the series in terms of H$_2$-yield are summarised in Table 7. The major findings are:

- Since the ruthenium based catalyst shows a higher CH$_4$-conversion at low temperatures also the obtained H$_2$-yield is higher. At 750 °C and the s/c-ratio of 3 or 4 the nickel catalyst shows equal or higher H$_2$-yields compared to the ruthenium catalyst.
- An increase of the s/c-ratio from 3 to 4 shows no significant effect when the ruthenium catalyst is used for the reforming of pure methane but increases the H$_2$-yield during biogas reforming
- Biogas reforming always led to a lower H$_2$-yield than SMR. This can be explained with the higher CO$_2$ content in the stream which leads to increased reversed water-gas shift activity.

While the ruthenium catalyst outperformed the nickel based catalyst at low temperatures it did not show higher CH$_4$-conversions or H$_2$-yields than the nickel catalyst at higher temperatures and s/c-ratios under the given conditions. Both catalysts are capable of converting biogas and methane close to the thermodynamic limits of the reactions. Taking into account the price of ruthenium, which is several orders of magnitude higher, it does not seem to be reasonable to use this catalyst for the reformer-steam iron process even if higher conversion rates can be achieved. Compared to the amount of oxygen carrier the catalyst will only contribute to a minor extend to the total volume of the

complete system and, therefore, the nickel catalyst was chosen for consecutive experiments.

**Table 7: Comparison of the H$_2$-yield of methane and biogas reforming using ruthenium and nickel based catalysts.**

| s/c | T / °C | H$_2$-Yield / % | | | |
|---|---|---|---|---|---|
| | | methane | | biogas | |
| | | Ru-cat. | Ni-cat. | Ru-cat. | Ni-cat. |
| 2 | 650 | 77±2 | 65±3 | 67±1 | 54±14 |
| | 700 | 84±0 | 76±3 | 72±1 | 67±2 |
| | 750 | 85±1 | 84±2 | 74±1 | 74±1 |
| 3 | 650 | 84±1 | 74±1 | 73±0 | 72±1 |
| | 700 | 89±0 | 82±3 | 77±1 | 74±1 |
| | 750 | 88±0 | 88±2 | 78±0 | 80±0 |
| 4 | 650 | 85±0 | 80±1 | 78±1 | 78±4 |
| | 700 | 89±0 | 87±2 | 82±1 | 81±2 |
| | 750 | 89±0 | 90±1 | 83±1 | 85±2 |

# 4. Oxygen carrier development for the steam iron process

The work presented in this chapter was done during an extended research stay in the *Laboratory of Energy Science and Engineering* at *ETH-Zurich between* October and December 2014.

## 4.1.    Fundamentals

A key aspect for chemical looping hydrogen production and chemical looping combustion is the stability of the oxygen carrier. An ideal oxygen carrier must combine high reactivity and stability with low costs and low toxicity. In addition, it has to be insensitive for the formation of solid carbon. Since it is permanently exposed to high temperatures and has to undergo cyclic reduction and oxidation steps unmodified iron tends to deactivate rapidly during chemical looping operation especially if it is completely reduced to Fe [72,77]. Therefore, research activities are focusing on the improvement of the cyclic stability of oxygen carriers via the addition of high-melting point metal oxides such as $Al_2O_3$, CaO, MgO, $MgAl_2O_4$, $SiO_2$, $TiO_2$, YSZ and $ZrO_2$. A comprehensive review of chemical looping processes including also a detailed list of iron based oxygen carriers was written by Adanez et al. in 2012 [37]. Some metal oxides are known to form solid mixtures with different iron species during reduction or oxidation. Bohn et al. investigated the effects of Al, Cr, Mg, and Si oxides on chemical looping hydrogen production [72]. While $SiO_2$ had no positive effect, most likely due to the formation of low melting point silicates, Al, Cr, and Mg stabilised the amount of produced hydrogen. In order to achieve stable hydrogen yields with the Al-stabilised oxygen carrier an air-oxidation step was necessary to decompose hercynite ($FeAl_2O_4$) which has been formed. Kidambi et al. investigated the formation of $FeAl_2O_4$ in more detail and concluded that the presence of $FeAl_2O_4$ retards the rate of reduction [78]. Chen compared the effects of $Al_2O_3$ and $TiO_2$ addition on chemical looping hydrogen generation and reported the formation of ilmenite ($FeTiO_3$) under reaction conditions [79]. Ku et al. investigated $Fe_2TiO_5$ pellets as potential oxygen carriers for chemical looping hydrogen production [80]. $Fe_2O_3/TiO_2$ was found as the highest oxidation state after 30 cycles but $Fe_3O_4$ and $FeTiO_3$ were formed after the steam-oxidation step. In 2015 Lie et al. investigated the influence of $Na_2O$ and MgO on the formation of $FeAl_2O_4$ [81]. They found out that the interaction between FeO and $Al_2O_3$ can be mitigated in an oxygen carrier containing Mg with an Al/Mg ratio of 2 and measured stable hydrogen yields over 20 cycles regardless of the inclusion of air-oxidation. Cerium(IV)oxide is well known as support material for different types of catalytic and non-catalytic reactions such as dry reforming [82–84] steam methane reforming and gasification [85–88] catalytic combustion and off-gas treatment [89–91] or groundwater treatment [92]. Due to its high oxygen storage capacities and redox properties it is also an interesting material for chemical

looping applications and some research was carried out during the last years. Zhu et al. prepared a $CeO_2-Fe_2O_3$ complex oxide with a molar ratio of Ce/Fe=1 by co-precipitation and studied its redox properties in the chemical-looping steam methane reforming and hydrogen production process using a fixed-bed reactor [93]. They measured the formation of $CeFeO_3$ (cerium orthoferrite) during the methane conversion reaction at 850 °C. The re-oxidation of surface $CeFeO_3$ during the consecutive water-splitting step led to the formation of $CeO_2$ and $Fe_3O_4$. Gu et al. used a co-precipitation method to synthesise a series of $CeO_2$-modified $Fe_2O_3$ oxides with Ce/Fe molar ratios ranging from 5/95 to 50/50 [94]. They measured improved stability compered to pure $Fe_2O_3$ oxygen carriers after successive reduction/oxidation testing and concluded that the improved redox property of the $CeO_2$ modified samples was related with the formation of perovskite-type $CeFeO_3$. Miller and Siriwardane modified $Fe_2O_3$-based oxygen carriers with 5 - 25 wt% $CeO_2$ by a hot incipient wetness impregnation method and measured stable conversions over 15 reduction/oxidation cycles of chemical looping combustion [95]. Lee et al. prepared Fe-based mixed oxide mediums with Rh and $ZrO_2$ with a $CeO_2$ content ranging from 0 to 30 wt% and found out that the total amount of evolved hydrogen of the 0 wt% $CeO_2$ sample was maintained at a constant level during ten repeated redox cycles, but the required oxidation time for each oxidation was increased with increasing the number of redox cycles. The addition of $CeO_2$ preserved the reactivity of the oxygen carriers and led to stabilised hydrogen formation rates [96]. Fang et al. investigated the effect of $CeO_2$ on $Fe_2O_3$-$Al_2O_3$ oxygen carriers prepared via a freeze granulation method [97]. They did not find any influence of $CeO_2$ on the physical properties such as surface area or morphology and concluded that the increased reactivity of the material was related to the formation of oxygen vacancies in the $Fe_2O_3$-$CeO_2$ solid solution.

Different methods ranging from simple mechanical mixing of metal oxides to chemical synthesis methods such as co-precipitation and impregnation were used to synthesise stabilised oxygen carriers [37]. In order to achieve a well dispersed mixture of different metal oxides within the oxygen carrier particles and to optimise the nanostructure more sophisticated methods such as sol-gel techniques were developed [98,99]. Herein, an alternative approach to control the morphology of metal oxides was used, the usage of templates as structure-directing agents. This method, which was originally developed by Eckhardt et al. for the synthesis of films of ZnO, $Co_3O_4$, $ZnCO_3$, and $Al_2(CO_3)_3$ was applied for the synthesis of $Fe_2O_3$-$CeO_2$ mixed metal oxides [100].

## 4.2. Materials and experimental

### 4.2.1. Sample preparation

The used precursor substances iron(III) nitrate nonahydrate (99+%), ceria(III) nitrate hexahydrate (99.5%) and alumina(III) nitrate nonahydrate (99+%), all Acros Organics, were used without any further purification. In a typical synthesis the precursors were dissolved together with anhydrous citric acid (99%), Acros Organics, and pluronic® p123, Sigma-Aldrich, in a 1 + 1 mixture of absolute ethanol and Milli-Q water. Detailed sample information is given in Table 8. The resulting solution was stirred at room temperature overnight and afterwards the solvent was evaporated at ambient pressure at 100 °C. The produced solid was heated in air at a rate of 5 °C per minute to the calcination temperature of 800 °C and kept at this temperature for 3 hours. Pure $CeO_2$ was synthesised the same way but with a pre-heating step at 300 °C using a hotplate and a 500 ml beaker before heating the sample to 800 °C in the calcination oven. This pre-heating step was necessary since ceria nitrate undergoes a rapid combustion reaction which otherwise would lead to a significant loss of product.

**Table 8: Weights and volumes of compounds used for the synthesis of oxygen carriers.**

| Sample name | $Fe(NO_3)_3$ $9H_2O$ / g | $Ce(NO_3)_3$ $6H_2O$ / g | $Al(NO_3)_3$ $9H_2O$ / g | p123 / g | Citric acid / g | solvent / ml |
|---|---|---|---|---|---|---|
| 100% $Fe_2O_3$ | 5.09 | - | - | 0.59 | 1.23 | 25 |
| 100% $CeO_2$ | - | 2.53 | - | 0.28 | 0.57 | 12 |
| 10% $CeO_2$ | 4.57 | 0.25 | - | 0.56 | 1.14 | 24 |
| 20% $CeO_2$ | 4.10 | 0.50 | - | 0.52 | 1.06 | 24 |
| 30% $CeO_2$ | 3.55 | 0.76 | - | 0.49 | 1.01 | 21 |
| 30% $Al_2O_3$ | 3.54 | - | 2.21 | 0.69 | 1.41 | 30 |

### 4.2.2. Material characterisation

Basic physical and chemical data for all oxygen carrier species can be found in Table 9. Prior to the TGA measurements all calcined samples were fractionised and only the 300 - 425 μm fraction was used for characterisation. TPR profiles were measured using a thermogravimetric analyser (Mettler-Toledo) coupled with a gas analyser for hydrogen detection (ABB-EL3020). During a typical TPR-experiment 10 mg of oxygen carrier was heated in a mixture of 5 ml·min⁻¹ hydrogen and 95 ml·min⁻¹ nitrogen from room temperature to 1050 °C at a heating rate of 10 °C·min⁻¹ and kept at this temperature for 45 minutes. Cycling experiments in order to analyse the stability of the developed oxygen carriers were performed using the same thermogravimetric analyser but without a gas analysis system.

The calcined oxygen carrier samples were heated to 800 °C at a heating rate of 10 °C min$^{-1}$ in a constant nitrogen flow of 100 ml·min$^{-1}$. Each cycle consisted of a reduction phase (5 ml·min$^{-1}$ H$_2$ + 95 ml·min$^{-1}$ N$_2$; 50 min) a CO$_2$-oxidation phase (15 ml·min$^{-1}$ CO$_2$ + 85 ml·min$^{-1}$ N$_2$; 25 min) and an air-oxidation phase (25 ml·min$^{-1}$ air + 75 ml·min$^{-1}$ N$_2$; 15 min).

**Table 9: Physical and chemical properties of investigated materials [101].**

| Name | Molecular formula | Molecular weight g mol$^{-1}$ | Melting point °C |
|---|---|---|---|
| Haematite | Fe$_2$O$_3$ | 159.7 | 1539 |
| Magnetite | Fe$_3$O$_4$ | 231.53 | 1538 |
| Iron(II) oxide | FeO | 71.85 | 1360 |
| Iron | Fe | 55.85 | 1535 |
| Aluminium oxide | Al$_2$O$_3$ | 101.96 | 2050 |
| Cerium(IV) oxide | CeO$_2$ | 172.12 | 2000 |

The first oxidation phase was performed using CO$_2$ instead of steam in order to simplify the experimental procedure (Eq (25)).

$$3Fe + 4CO_2 \rightarrow Fe_3O_4 + 4CO \tag{25}$$

To investigate the ability for chemical looping processing of natural gas seven cycles consisting of a CH$_4$-reduction phase (5 ml·min$^{-1}$ CH$_4$ + 95 ml·min$^{-1}$ N$_2$; 50 min), a purge phase (60 ml·min$^{-1}$ N$_2$; 5 min) a CO$_2$-oxidation phase (15 ml·min$^{-1}$ CO$_2$ + 85 ml·min$^{-1}$ N$_2$; 15 min), an air-oxidation phase (25 ml·min$^{-1}$ air + 75 ml·min$^{-1}$ N$_2$; 15 min) and a second purge phase (50 ml·min$^{-1}$ N$_2$; 5 min) were performed. Selected samples were additionally characterised using scanning electron microscopy (Zeiss Gemini 1530 FEG) and X-ray diffraction (XRD; Bruker, AXS D8 Advance).

## 4.3.    Results and discussion

TPR experiments:

Figure 21 shows the results of the TPR experiments. The pure CeO$_2$ sample showed no significant hydrogen consumption peak but a fast weight loss between room temperature and 120 °C. This mass loss of 0.4 wt% might be attributed to moisture or carbon dioxide adsorbed at the sample. Afterwards a constant weight loss to 700 °C was observed, followed by a fast weight loss between 700 °C and 900 °C and a constant weight loss between 900 °C and 1050 °C. Overall the mass decreased to a value of 97.3% of the initial mass which equals a reduction from CeO$_2$ to CeO$_{1.71}$. If the initial weight loss is taken into account

$CeO_{1.75}$ can be calculated as the reduced species. This value is lower than the one found by Laachir et al. who investigated the reduction of $CeO_2$ by hydrogen at temperatures between 300 K and 1200 K (26.85 °C – 926.85 °C) and identified $CeO_{1.83}$ as the final product [102]. On the other hand, Moog et al. reduced pure $CeO_2$ in hydrogen/argon mixtures and measured a weight loss of approx. 2.25% at 700 °C which is in accordance with the measured value [103]. The pure $Fe_2O_3$ sample showed three hydrogen consumption peaks that can be attributed to the three consecutive reduction steps from $Fe_2O_3$ to Fe (Ep. (7) – (9)). The first maximum of hydrogen consumption was measured at 450 °C. The second reduction step did not show a clear peak but maximum hydrogen consumption was measured at a temperature range from 630 °C to 660 °C followed by the third maximum at 735 °C. The maxima of the 10 wt% $CeO_2$ sample were measured at temperatures of 430 °C, 620 °C and 700 - 710 °C which is always lower than the corresponding values of the pure $Fe_2O_3$ sample. The magnetite to wustite reduction peak at 620 °C was very weak compared to the corresponding peak of the pure $Fe_2O_3$ sample and impossible to identify in the 20 wt% and 30 wt% $CeO_2$ samples. Maximum consumption rates of the 20 wt% sample were measured at 430 °C and 720 - 730 °C, of the 30 wt% $CeO_2$ sample at 450 °C and 705 °C. Therefore, no clear influence of $CeO_2$ on the hydrogen consumption rates could be identified. Onset temperatures as well as maxima seem to be shifted to lower temperatures but the effect cannot be clearly attributed to the changing amount of $CeO_2$. The fact that always the same total amount of oxygen carrier was analysed implies a changing amount of reducible species at the different measurements and impedes the identification of small influences of $CeO_2$ on the reduction behaviour of the investigated samples. The mass changes of the pure $Fe_2O_3$ sample and the different $CeO_2$-$Fe_2O_3$ mixtures show similar behaviour. No clear influence of $CeO_2$ on the reduction rate could be identified and all samples are in good agreement with the theoretic values of mass change. The 10 wt% $CeO_2$ samples showed fast reduction to Fe and at temperatures higher than 750 °C only an insignificant mass change occurred which is in good agreement with the $H_2$-consumption results. The 20 wt% and 30 wt% $CeO_2$ samples showed a slight mass decrease even at temperatures above 750 °C which can be related to a slow reduction of $CeO_2$ or iron oxide. The pure $Fe_2O_3$ sample did not reach a stable weight at 1050 °C, but after keeping it at this temperature for additional 45 minutes no further weight loss was measured. This gives rise to the assumption that a sintering effect of the pure $Fe_2O_3$ led to reduced reactivity of the sample while no such effect was measured for $CeO_2$ stabilised $Fe_2O_3$ samples. As a reference experiment also a 30 wt% $Al_2O_3$ sample was analysed. The sample showed in general a lower apparent hydrogen consumption rate compared to the $Fe_2O_3$-$CeO_2$ samples and two maxima at 440 °C and 650 °C were visible. The mass change during the reduction was significantly slower compared to all other samples except the pure $CeO_2$ material. At 1050 °C the reduction was still not

completed while after 45 minutes at this temperature a constant weight in good agreement with the calculated values was reached. The low reduction rate is in agreement with the finding of Kidambi et al. [78] and might be caused by the formation of $FeAl_2O_4$.
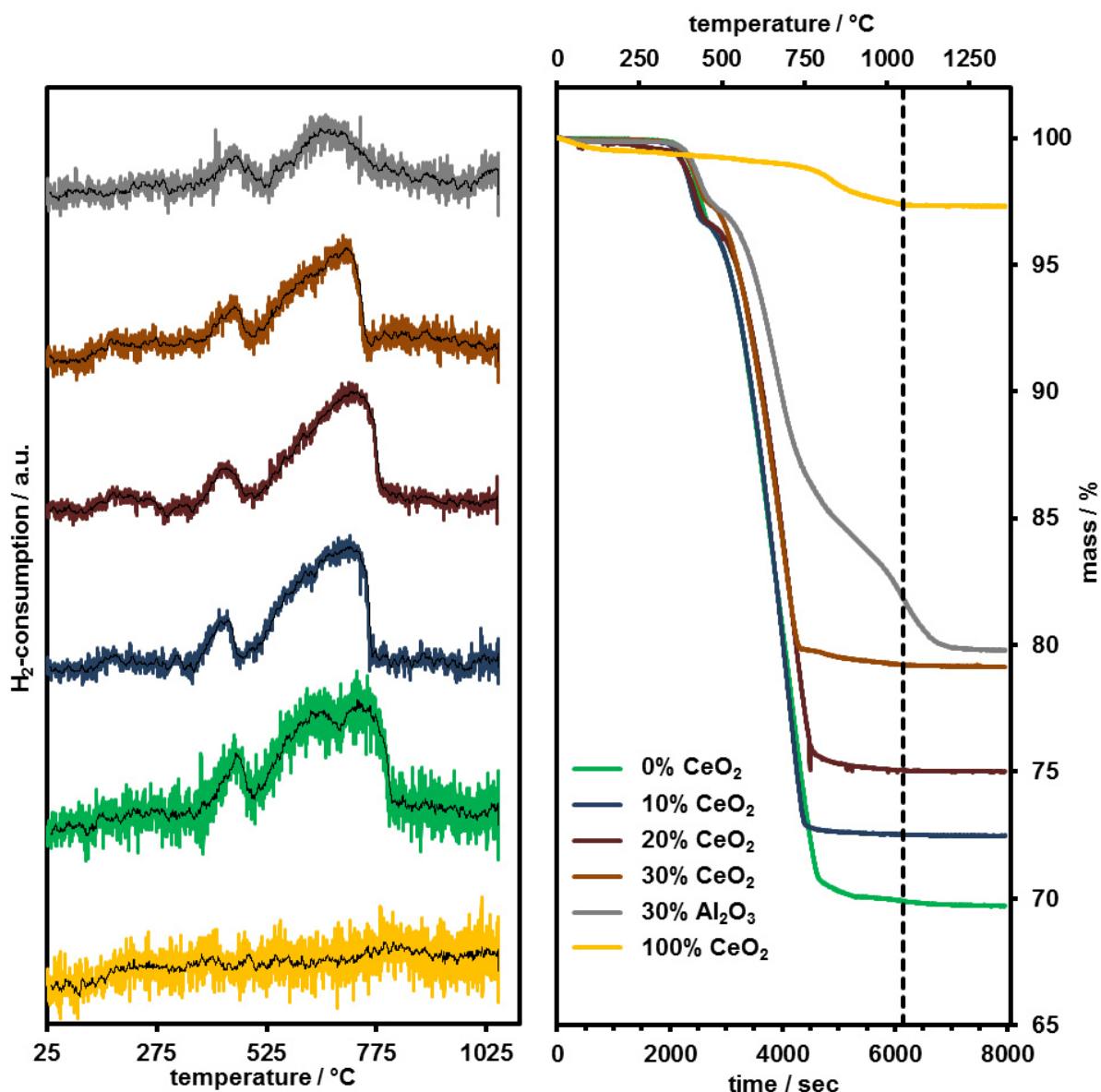


**Figure 21: TPR-profiles of $Fe_2O_3$-based oxygen carriers modified with different amounts of $CeO_2$ and $Al_2O_3$; the dashed vertical line in the right diagram indicates the beginning of the isothermal process step.**

Cycling experiments:

Figure 22 shows the results of seven consecutive reduction and oxidation cycles of three $CeO_2$-$Fe_2O_3$ oxygen carriers. During the heating-up all samples showed a slight mass decrease although each sample was calcined at 800 °C. Therefore, the mass after the first oxidation with air was defined as 100% for all experiments. All samples showed promising results in terms of stability. Full oxidation could be achieved in all seven air-oxidation steps and also the weight changes related to reduction and $CO_2$-oxidation stayed almost constant.
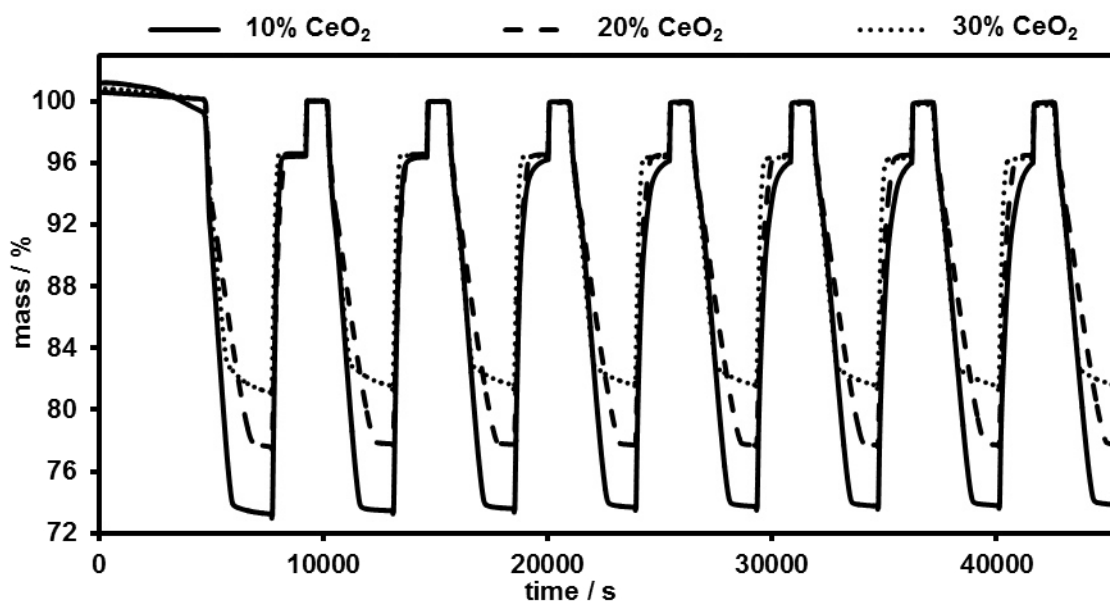
**Figure 22: Seven consecutive cycles consisting of reduction with hydrogen, oxidation with carbon dioxide and oxidation with air.**

Figure 23 gives detailed information about the stabilising effect of different amounts of $CeO_2$ added to the oxygen carriers. Figure 23 (A) compares three complete cycles of the 10 wt% $CeO_2$ oxygen carrier. The overall mass change only showed minimal changes during 7 cycles but the reaction rates for reduction and $CO_2$-oxidation were clearly reduced after several cycles. The time needed for the reduction of the oxygen carrier was almost doubled after 7 cycles. An even higher degradation effect was identified for the $CO_2$-oxidation step. While it took only 10 minutes during the first cycle to oxidise the material even after 25 minutes no constant mass level was reached during cycle number 7. No negative effect was measurable for the air-oxidation step which stayed constant for 7 cycles. Samples with increased amounts of $CeO_2$ showed better performance in terms of stability (Figure 23 B and C). The reaction rates during reduction and $CO_2$-oxidation still slightly decreased during 7 cycles but it is obvious that higher amounts of $CeO_2$ increase the stability and stable conversion rates can be achieved. It has to be mentioned that no complete reduction was achieved during the cycling experiments since slight mass decrease was measured also at the end of each reduction step. The TPR experiments (Figure 21) showed that complete reduction of the developed oxygen carriers is possible at a temperature of 800 °C but the reduction time of 50 minutes seemed to be too short for full reduction. In order to quantify the stability of the different oxygen carriers the oxygen storage capacity (OSC / mmol·g$^{-1}$) was calculated from the measured mass change of the oxygen carrier ($\Delta m_{OC}$ / g), the molecular mass of oxygen ($MW_O$=15.999 g·mol$^{-1}$) and the initial sample mass ($m_{OC}$ / g) following equation (22).

$$OSC = \Delta m_{OC} / MW_O / m_{OC} \tag{22}$$
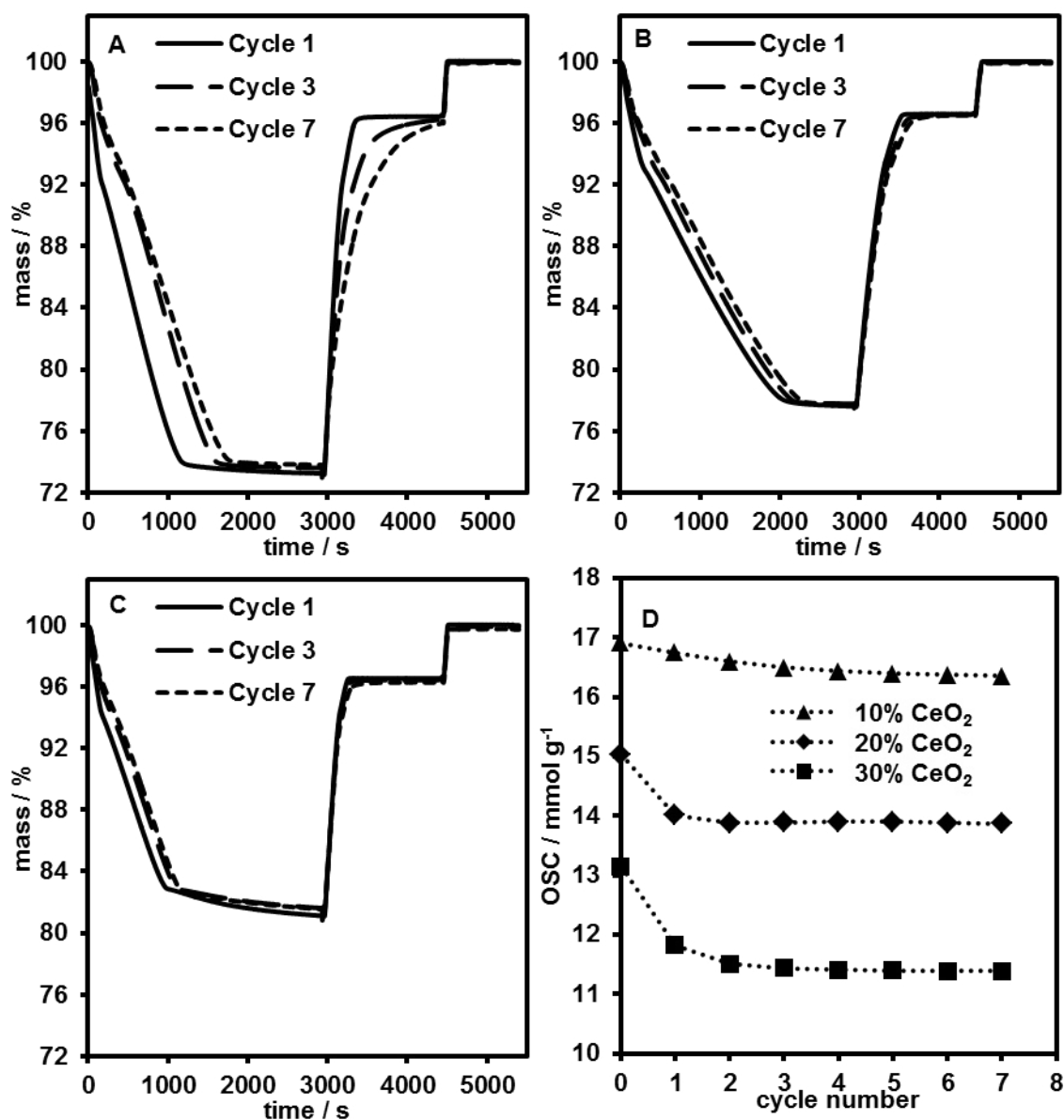
**Figure 23: Comparison of redox cycles of 10 wt% $CeO_2$ (A), 20 wt%$CeO_2$ (B), 30 wt% $CeO_2$ (C) and change of oxygen storage capacity OSC over seven cycles (D).**

Figure 23 (D) shows the change of the OSC during 7 cycles for all $Fe_2O_3$-$CeO_2$ oxygen carriers. Cycle "0" represents the theoretical maximum of the samples which is always slightly higher than the experimental values, since complete reduction was not achieved during the cycling experiments. An initial value of 99.1% of the theoretic OSC could be achieved for the 10 wt% $CeO_2$ sample which decreased to 96.7% after 7 cycles, giving a reduction of 0.3% per cycle. Only 93.2% of the maximum OSC were reached for the 20 wt% $CeO_2$ sample which decreased to 92.3%, giving a reduction of only 0.1% per cycle. The lowest OSC was reached with the 30 wt% $CeO_2$ sample. Only 89.8% were measured for the first cycle and the OSC decreased to 86.5%, giving a reduction of 0.5% per cycle. The phenomenon that the samples with higher contents of $CeO_2$ show lower OSCs compared to the theoretical maxima can be attributed to the incomplete reduction during the experiment,

and therefore a lower reduction rate is expected for samples with high content of $CeO_2$. A slightly lower reaction rate of the 20 wt% and 30 wt% $CeO_2$ samples compared to the 10 wt% $CeO_2$ and pure $Fe_2O_3$ samples was also measured at the TPR experiments. The 20 wt% $CeO_2$ sample showed the best OSC stability over 7 cycles while the highest decrease was measured for the 30 wt% $CeO_2$ sample. The change of OSC only gives information about the overall stability of the investigated samples but gives no information about the suitability of the material for chemical looping hydrogen production.

The $CO_2$-oxidation step is strongly affected by the $CeO_2$ content. The 10 wt% $CeO_2$ sample (Figure 23-A) showed a significantly decreased $CO_2$-oxidation rate after 7 cycles, compared to the samples with a higher $CeO_2$ content. Therefore, higher $CeO_2$ contents are preferred for chemical looping hydrogen production.

Material characterisation:

In order to get more information about the crystal structure of the different oxidation stages of the oxygen carrier the 20 wt% $CeO_2$ sample was further analysed with XRD. Figure 24 shows the XRD patterns of the fresh sample after calcination in air as well as after $H_2$-TPR, $CO_2$-oxidation and after air-oxidation. As expected the fresh sample consisted only of $Fe_2O_3$ and $CeO_2$. $Fe_2O_3$ was completely reduced to iron in hydrogen atmosphere. After $CO_2$-oxidation magnetite and $CeFeO_3$ were identified as products. Amounts of iron formed $CeFeO_3$ and this leads to a magnetite structure with some iron deficit. It was identified as $Fe_{2.91}O_4$ but further characterisation would be necessary to prove the exact composition. Only very weak signals for $CeO_2$ were measurable after the $CO_2$-oxidation step which indicates an almost complete conversion of $CeO_2$ to $CeFeO_3$ at 800 °C. After the air-oxidation step no more $CeFeO_3$ was present and magnetite was completely oxidised to $Fe_2O_3$. Since $CeO_2$ was the only cerium species present after the $H_2$-reduction step as well as after the air-oxidation step it is obvious that $CeFeO_3$ is formed during the $CO_2$-oxidation step and decomposed to $Fe_2O_3$ and $CeO_2$ after air treatment at high temperatures. Sample (d) was analysed after 10 complete cycles each consisting of $H_2$-reduction $CO_2$-oxidation and air-oxidation. Therefore, the fact that no $CeFeO_3$ was present proves that it is completely decomposed during the air-oxidation step and no accumulation of $CeFeO_3$ within the oxygen carrier occurs even after several cycles. Figure 25 shows scanning electron microscopy images of fresh samples as well as of the 20 wt% $CeO_2$ sample after cyclic treatment. All images of the fresh samples were taken after calcination at 800 °C for 3 hours in air. The 10 wt% $CeO_2$ sample (Figure 25-a) showed a highly sintered structure containing a large number of pores with a diameter between 10 and 100 nm. The sintering of the sample can be easily explained by the high calcination temperature of 800 °C which is far below the melting points of the $Fe_2O_3$ and $CeO_2$ but still high enough for sintering.
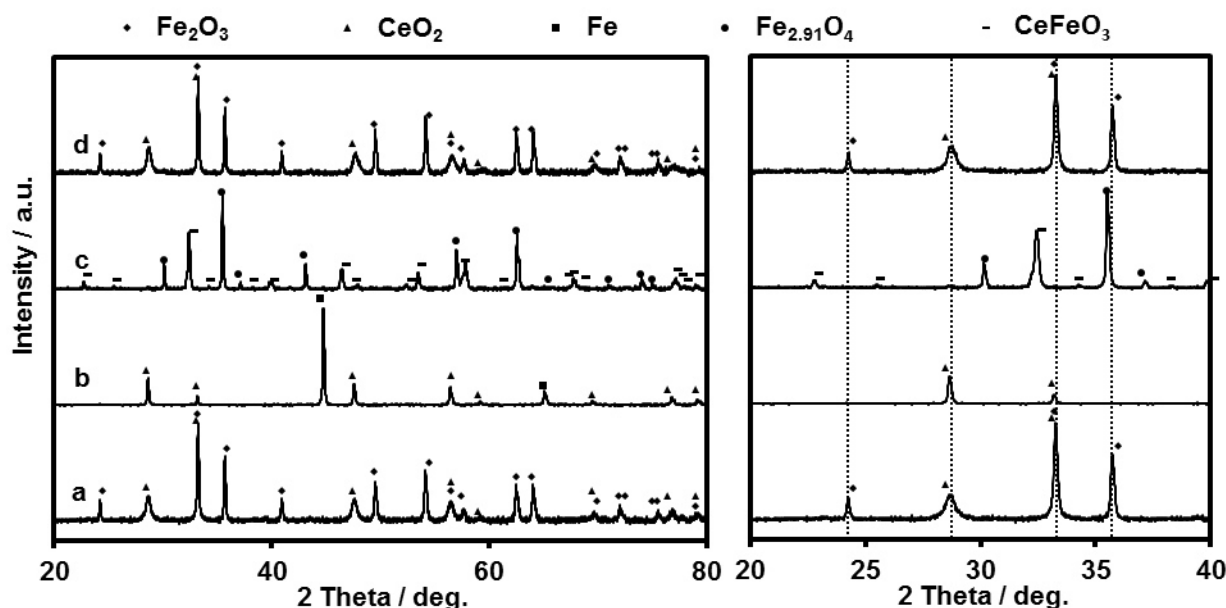
**Figure 24: XRD patterns of a fresh 20 wt% CeO$_2$ sample (a), after TPR (b), after CO$_2$-oxidation (c) and after 10 reduction/oxidation cycles (d).**

The small particles of approximately 10 - 50 nm on the surface of the material are supposed to be CeO$_2$ since they are present at all CeO$_2$ containing samples (Figure 25 a-c), but not in the pure Fe$_2$O$_3$ sample (Figure 25-d) and their amount increases with growing CeO$_2$ content of the sample. Compared with the pure Fe$_2$O$_3$ sample the grain size of the 10 wt% CeO$_2$ stabilised sample is smaller and the porosity higher which is in good accordance with the proposed stabilising effect of CeO$_2$. The 20 wt% CeO$_2$ sample (Figure 25-b) differs significantly from the 10 wt% sample as well as from the pure Fe$_2$O$_3$ sample. Two regions of different grain size and porosity are visible. In the region on the left side of the image the CeO$_2$ content seems lower than on the right side and, therefore, less but bigger pores are present due to stronger sintering of the particles. The preparation technique used for material synthesis should lead to highly uniform samples and, therefore, the non-uniform distribution of CeO$_2$ is unexpected and cannot be explained for sure. One possible explanation might be a lower solubility of iron(III) nitrate compared to ceria(III) nitrate in the used water/ethanol mixture. In this case during the drying of the sample, when a certain amount of solvent is already evaporated, parts of iron(III) nitrate crystallise prior to the ceria(III) nitrate. This would lead to the formation of an iron rich solid and a ceria(III) nitrate enriched solution. After further evaporation of the solvent the residual amount of iron(III) nitrate crystallises together with most of the ceria(III) nitrate and forms an ceria enriched solid. Deganello et al. investigated the effect of the pH value on the citrate-nitrate auto-combustion synthesis of CeO$_2$ and stated that at low pH values citric acid does not form stable metal complexes with ceria [104].
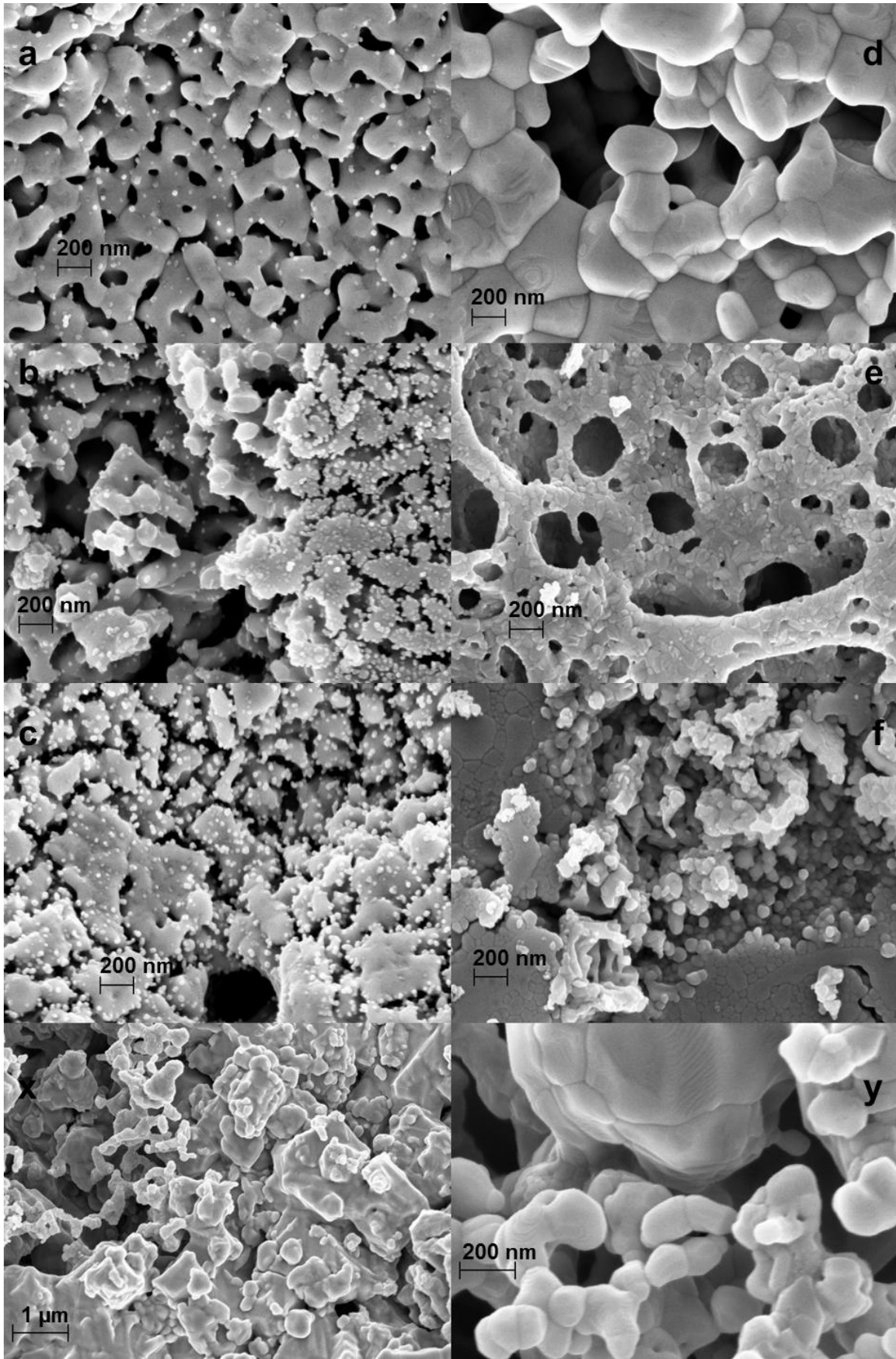
**Figure 25: SEM images of the calcined oxygen carriers: 10% CeO$_2$ (a), 20% CeO$_2$ (b), 30% CeO$_2$ (c), pure Fe$_2$O$_3$ (d), pure CeO$_2$ (e) and 30% Al$_2$O$_3$ (f) and of the 20% CeO$_2$ oxygen carrier after 10 reduction/oxidation cycles (x and y).**

The influence of the pH value was also found as contributing factor for citrate-nitrate based synthesis of $SrFeC_{0.5}O_y$ [105]. The 30 wt% $CeO_2$ sample (Figure 25-c) showed the highest porosity, the smallest grain size and a uniform $CeO_2$-$Fe_2O_3$ distribution was achieved. The lower concentration of iron(III) nitrate and the higher concentration of ceria(III) nitrate within the solution might be the explanation why a uniform $CeO_2$ distribution was achieved for the 30 wt% $CeO_2$ sample but not for the 20 wt% $CeO_2$ sample. The pure $CeO_2$ reference material (Figure 25-e) showed a completely different morphology than the $CeO_2$-$Fe_2O_3$ mixtures and the pure $Fe_2O_3$ sample. A foam-like structure with pores ranging from a few nanometres to micrometres was gained as product. This structure can be explained by the very fast formation of gaseous compounds during the calcination step which made it necessary to perform a two-step calcination process due to safety issues. This behaviour is well known for solutions of ceria(III) nitrate and citric acid and is used for the preparation of ceria based materials for various applications [104,106]. Due to the low ceria(III) nitrate concentration no such rapid gas formation was noticed during the calcination of the other samples. Compared to the $Fe_2O_3$ material the grain size of pure $CeO_2$ is smaller. The higher melting point of $CeO_2$ leads to reduced sintering behaviour and, therefore, finer grains are preserved also after the calcination procedure. Although the same synthesis route was chosen the structure of the 30% $Al_2O_3$ sample (Figure 25-f) is completely different from all $CeO_2$ containing samples. A densely sintered material almost without any pores was produced. Beside the possible formation of $FeAl_2O_4$ also this structure gives an explanation for the low reactivity at the $H_2$-TPR-experiment compared to the $CeO_2$ containing samples. A dense structure inhibits the reaction of hydrogen with surface oxygen and only the slower reaction driven by bulk-phase diffusion of oxygen can occur. To investigate structural changes of the oxygen carrier samples SEM images of the 20% $CeO_2$ oxygen carrier were taken after 10 complete reduction and oxidation cycles (Figure 25 x and y). As already seen in the images of the fresh sample (Figure 25-b) regions of high porosity as well as sintered areas can be found but in general a reduction of surface area and porosity after repeated cycling was obvious. Nevertheless, only moderate OSC losses were measured during the TGA experiments indicating that most of the oxygen carrier is still accessible for reaction gases. This phenomenon is was already described for $ZrO_2$-based samples by Liu, Dennis and Scott [73].

In order to investigate the suitability of the developed $CeO_2$-$Fe_2O_3$ oxygen carriers for chemical looping combustion of natural gas cyclic experiments were performed using methane, instead of hydrogen, for the reduction. Figure 26 shows the results of seven consecutive reduction/oxidation cycles (left) as well as details of the first cycle (right). At the beginning of each reduction period a fast mass decrease was observed due to the reduction of $Fe_2O_3$ with methane (Eq. (10)).
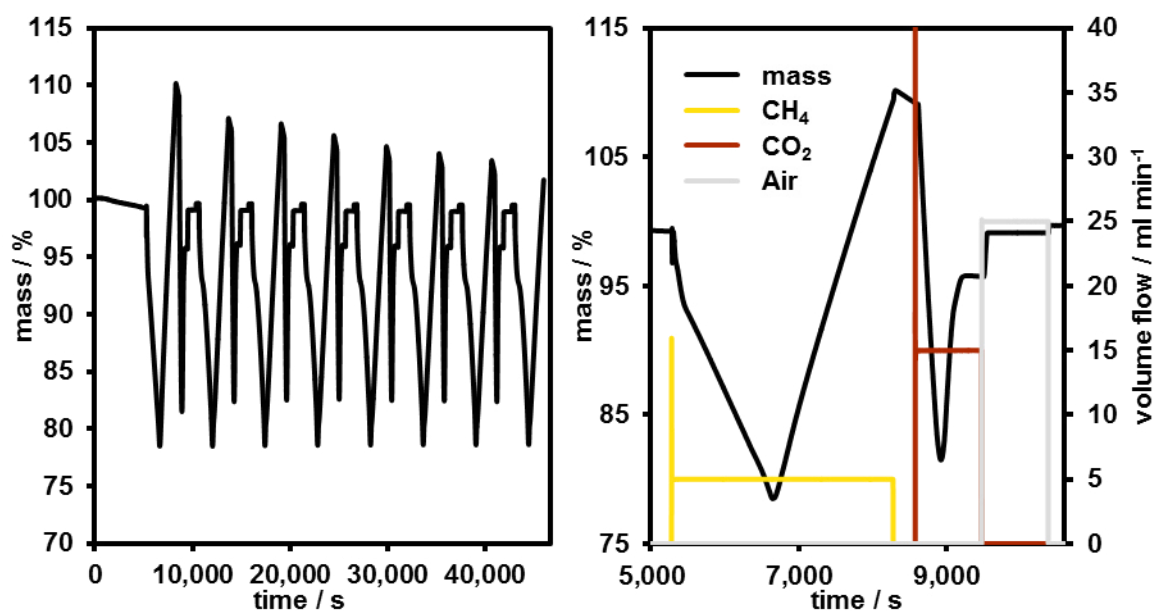
**Figure 26: 7 reduction/oxidation cycles (left) and detailed view of the first cycle using methane, carbon dioxide and air (right).**

At a certain point the mass decrease stopped and turned into a mass increase. This behaviour can be explained by the increasing amount of reduced iron which catalyses the methane decomposition reaction (Eq. (16)) and, therefore, leads to the formation of solid carbon [62–65]. After a short purge phase to remove methane from the system carbon dioxide was used to re-oxidise the sample. At the beginning of the oxidation reaction the oxygen carrier mass decreased due to the oxidation of carbon by the Boudouard reaction (Ep. (17)). At a certain point most of the solid carbon is removed from the oxygen carrier and the mass increases until iron is re-oxidised to magnetite. The $CO_2$-oxidation is followed by a final air-oxidation step which regenerates the oxygen carrier and leads to the formation of haematite. In all cycles the minimum mass, which was reached before the formation of solid carbon, was constant. This indicates a constant degree of reduction before the formation of solid carbon becomes dominant. The maximum mass reached at the end of the reduction decreased slightly with increasing cycle number. Since the methane decomposition reaction is catalysed by iron a decrease of reactive surface of the oxygen carrier can lead to lower catalytic activity and, therefore, also the observed decrease of carbon formation. No significant effect of methane compared to hydrogen as reducing agent was found concerning the overall stability of the oxygen carrier. Figure 27 compares the fresh 30 wt% $CeO_2$ oxygen carrier after calcination (a) with the $CH_4$-reduced sample (b) as well as with a reference sample after $H_2$-reduction and $CO_2$-oxidation (c). Nano-sized whiskers can be found at the surface of the $CH_4$-reduced sample which might be solid carbon. This is accordance with the finding of Tang et al. who investigated the catalytic activity of different $CeO_2$-$Fe_2O_3$-based catalysts for the methane decomposition reaction [64].
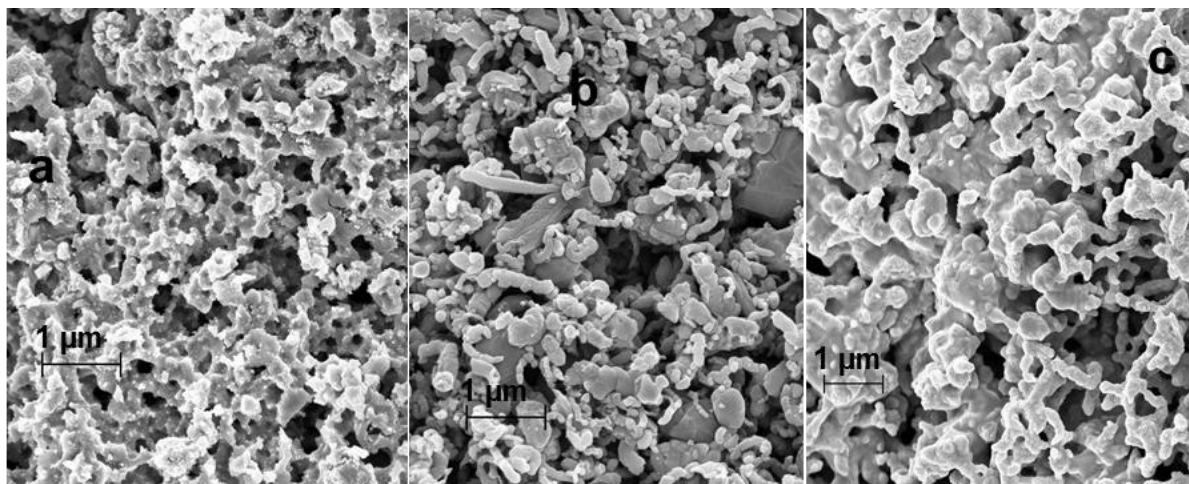
**Figure 27: Image of the fresh 30 wt% CeO$_2$ oxygen carrier (a), after 7 CH$_4$-reduction cycles at reduced state (b) and after CO$_2$-oxidation (c).**

## 4.4.     Summary and conclusion

The obtained results clearly show the suitability of Fe$_2$O$_3$-CeO$_2$ oxygen carriers for chemical looping combustion and chemical looping hydrogen production. All investigated oxygen carriers showed high stability over seven cycles. The OSC only decreased between 0.1% and 0.5% per cycle. Especially the reduction reaction and the CO$_2$-oxidation step turned out to be significantly influenced by the CeO$_2$ content of the oxygen carrier. The apparent rates of these reactions decreased strongly with increasing cycle number for the 10 wt% CeO$_2$ sample. The same trend, but only to a minor extend, was also found for the 20 wt% CeO$_2$ sample whereas the 30 wt% CeO$_2$ samples showed almost stable rates. XRD patterns after H$_2$ TPR experiments showed complete reduction of the oxygen carrier leading to Fe and CeO$_2$. The formation of CeFeO$_3$ after the CO$_2$-oxidation step was proven by XRD. Only Fe$_2$O$_3$ and CeO$_2$ but no CeFeO$_3$ were found after the air-oxidation step and no evidence for an accumulation of CeFeO$_3$ after repeated reduction and oxidation cycles was found. SEM images showed the stabilising effect of CeO$_2$ addition in order to keep high porosity even after repeated cycling. The cycling experiment using methane as reducing agent indicated high reactivity in terms of iron reduction but also in terms of methane decomposition. Up to 10 wt% of solid carbon was deposited on the oxygen carrier during the CH$_4$-reduction experiments. During the consecutive CO$_2$ and air-oxidation steps the re-oxidation of carbon was observed. Since the formation of solid carbon has to be avoided in order to produce pure hydrogen and for efficient CO$_2$ sequestration the reduction period has to be adjusted. Fe-CeO$_2$ mixtures are known to catalyse the methane decomposition reaction and the formation of solid carbon. Therefore, the amount of fully reduced oxygen carrier has to be minimised if methane is directly used as feedstock. No significant influence of methane compared to hydrogen in terms of stability was found with the cycling experiments.

# 5. The Flex Fuel Reformer prototype

The main objective of this thesis was the development of a stand-alone prototype for the production of pure hydrogen using a hydrocarbon feedstock. Based on the previously presented data a prototype of the reformer-steam iron process was developed: *The flex fuel reformer*. The working-principle of the prototype and the multi fixed bed reactor configuration are included in the patent application A50526/2014.

## 5.1. Working principle

Figure 28 shows the reactor as well as the complete prototype. A detailed plan of the whole assembly as well as a list of the main components can be found in the appendix (Table-A I). The core-element of the prototype is the multi-fixed-bed reactor in which a section for catalytic syngas generation and a section for the cyclic reduction and oxidation of iron oxide are integrated (Figure 29).



**Figure 28: The multi-fixed-bed reactor (1), top section of the prototype (2), gas burner (3) and the complete flex fuel reformer prototype (4).**

The reactor is made of high performance stainless steel (1.4841; X15CrNiSi25-21) and operated in reversed flow mode. Gases are fed into the system from the bottom during the reforming and reduction step while steam for the oxidation is provided from the top section of the reactor. During the reforming step a mixture of steam and fuel (e.g. $CH_4$) is fed into the system from the bottom of the reactor and streams in a region of inert material for preheating. Afterwards the preheated mixture reaches the catalyst region and reacts to syngas (Eq. (1)). This syngas streams through a second zone containing inert material before it reaches the oxygen carrier region for reduction (Eq. (5)). This design guarantees the highest possible inlet temperature and, therefore, helps to avoid the formation of solid carbon via the Boudouard reaction (Eq. (17)) near the inlet of the catalyst zone.
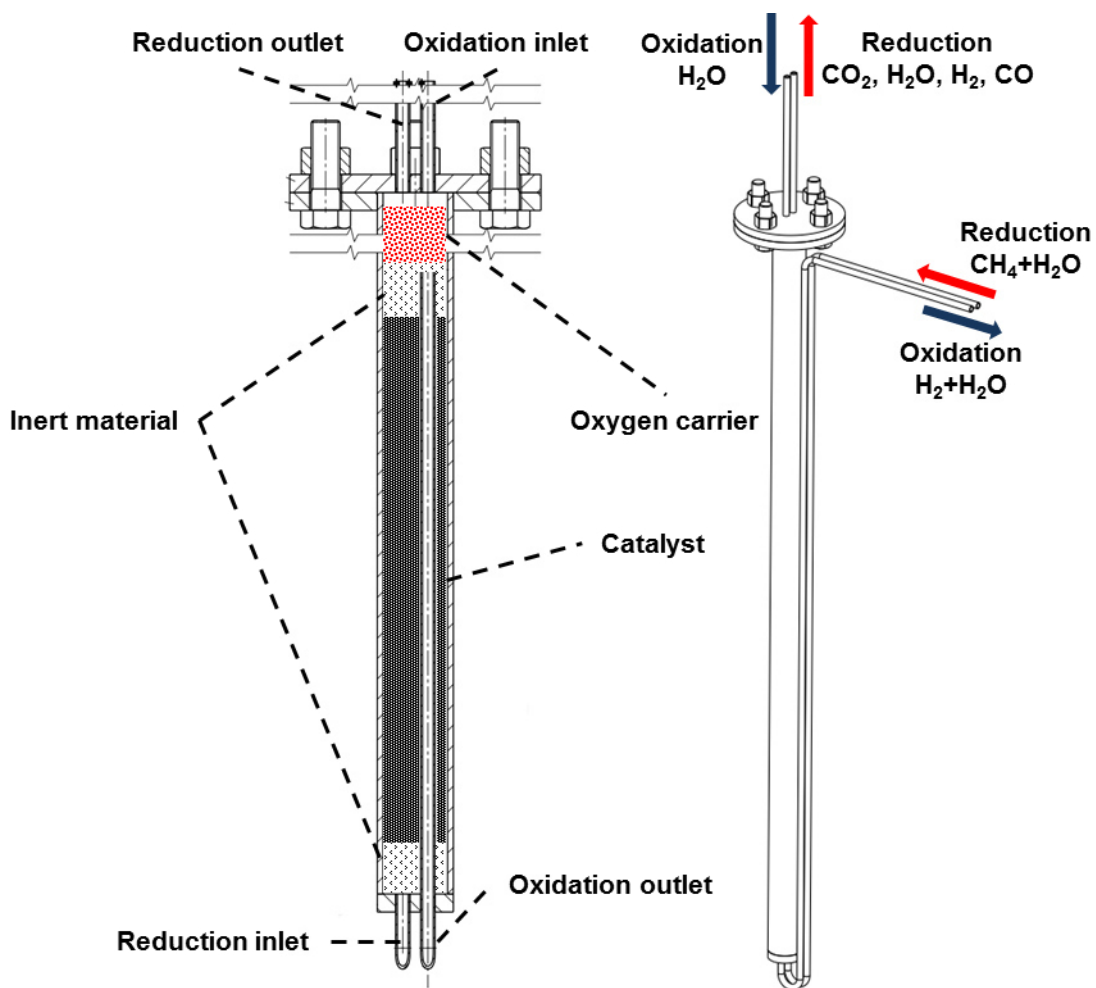


**Figure 29: Working principle of the flex fuel reformer reactor, drawn by M. Kühhas.**

After the oxygen carrier is reduced steam is fed into the system from the opposite side of the reactor. This configuration is expected to increase the efficiency of the system, especially if the oxygen carrier is not fully converted after the reduction. In this case different species of iron oxides are present within the reactor. Figure 30 shows a simplified concept of the formation of regions of different species within the fixed bed. Thermodynamic equilibrium

concentrations are assumed as 70% $H_2$ + 30% $H_2O$ for the reaction iron ↔ wustite and 35% $H_2$ + 65% $H_2O$ for the reaction wustite ↔ magnetite (see also Figure 2). During the reduction, near the inlet section of the reactor iron oxide is fully reduced and no further reaction can occur (a). Therefore, the hydrogen concentration equals the inlet concentration. The hydrogen concentration decreases to 65% within the wustite → iron reaction zone (b) and further decreases to the outlet concentration of 30% hydrogen within the magnetite → wustite reaction zone (c). If the reduction is stopped before magnetite is completely reduced to wustite three species are present in the reactor at the beginning of the consecutive oxidation. In this case, at the beginning of the oxidation, near the inlet section magnetite is formed immediately. When iron is completely oxidised to magnetite no additional hydrogen is produced in this region (d). A concentration of 30% hydrogen is present in the first wustite region because of the wustite → magnetite equilibrium (e) and a concentration of 65% of hydrogen is reached in the iron zone because of the iron → wustite equilibrium (f). After a complete reduction of the oxygen carrier this would be the outlet concentration of the reactor. After incomplete reduction the steam hydrogen mixtures flows through the zone of not fully reduced wuestite (g) without any reaction occurring, due to the fact that gas and solid are in thermodynamic equilibrium. When the mixture reaches the zone of fresh magnetite, near the outlet of the reactor, the hydrogen content of this mixture is high enough for the reduction of magnetite to wustite (h). In other words a major share of the produced hydrogen is converted during the oxidation step for the reduction of magnetite near the outlet section of the reactor. Only after the reduction of this compound to wustite a mixture of 65% hydrogen and 35% steam reaches the outlet of the reactor.
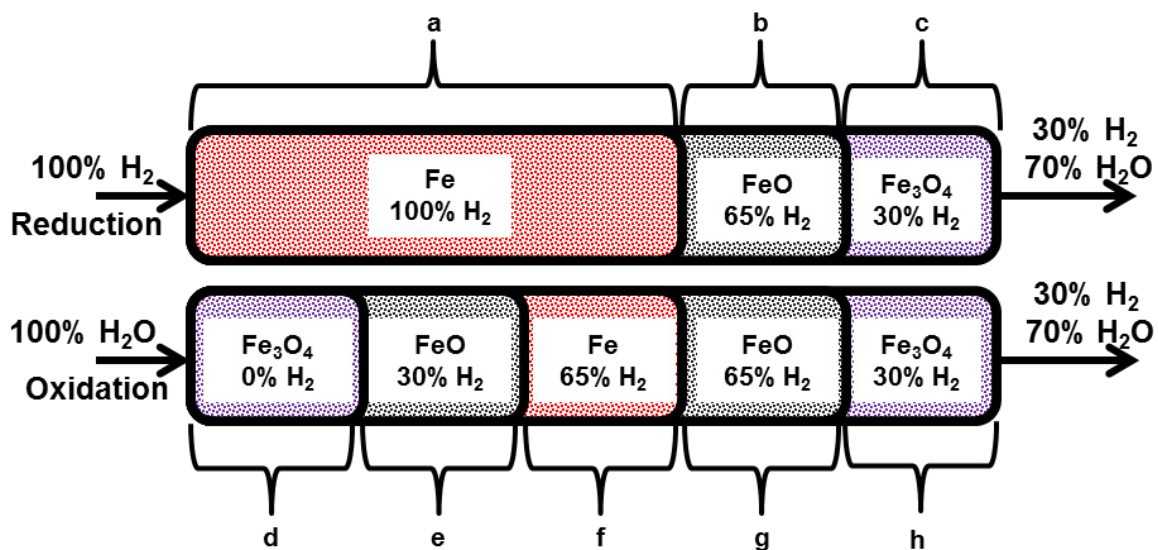


**Figure 30: Simplified schema of steam and hydrogen concentration during reduction and during oxidation after incomplete reduction; solid species in the illustration represent the educts of the corresponding reaction.**

Even though the total amount of produced hydrogen is not influenced, the oxidation time as well as the amount of steam that is needed for the complete oxidation of the oxygen carrier increases. The reversed flow operation of the reactor as it is realised in the flex fuel reformer prototype avoids this problem (Figure 31). When steam is supplied to the system it streams through the magnetite region near the former outlet region (i) and no reaction takes place. In the wustite $\rightarrow$ magnetite zone (j) a concentration of 30% hydrogen is present and the hydrogen concentration increases to 65% in the iron $\rightarrow$ wustite reaction zone (k). Therefore, the reversed flow operation increases the flexibility of the process in terms of cycle length and oxygen carrier conversion rate.



**Figure 31: Simplified schema of steam and hydrogen concentration during oxidation after incomplete reduction in reversed flow operation; solid species in the illustration represent the educts of the corresponding reaction.**

An important aspect of the reactor design is the position of the different tubes for gas supply and product removal. A tube positioned after the catalyst zone enables the removal of the produced steam/hydrogen mixture without passing the catalyst region. This design is expected to increase the purity of the produced hydrogen. If unfavourable reaction conditions such as low temperatures or steam to carbon ratios cause the formation of solid carbon this will primary happen in the catalyst zone. Contact of these carbon species with steam or hydrogen during the oxidation leads to the formation of impurities (Figure 6) but is avoided due to the reactor design.

## 5.2.    Preliminary experiments and proof of concept

In order to investigate the feasibility of the reactor design some proof of concept experiments were conducted using a tubular reactor containing two fixed beds. The results of the experiments were presented at the 4th European PEFC & $H_2$ Forum (2013, Lucerne, Switzerland), at the 2013 AIChE Annual Meeting (2013, San Francisco, USA) and at the 3rd International Conference on Chemical Looping (2014, Gothenburg, Sweden) [107–109]. These experiments investigated the concept of using two different fixed beds in one tubular reactor. The evaluation was focused on the hydrogen quality in terms of carbon monoxide and carbon dioxide content.

### 5.2.1. Experimental

An oxygen carrier based on haematite was prepared by mechanical mixing with $Al_2O_3$. A dry mixture of 90 wt% $Fe_2O_3$ (325 mesh, Alfa-Aesar) + 10 wt% $Al_2O_3$ (20-50 µm, Alfa-Aesar) was homogenised using an intensive mixer (Maschinenfabrik Gustav Eirich GmbH & Co KG). Deionised water was added slowly in order to produce stable granulated material. After drying and fractionating, the 2 - 3.15 mm fraction was used for reduction/oxidation experiments with methane and steam. The mixer for sample preparation, fresh and used samples are shown in Figure 32.
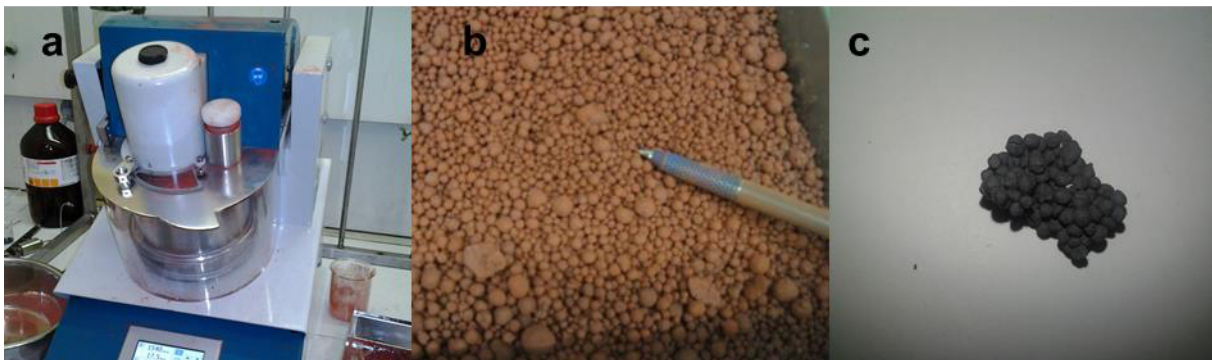


**Figure 32: Mixer for sample preparation (a), fresh sample (b) and sample after several cycles (c).**

Figure 33 shows a schematic illustration of the experimental setup. Gases were supplied using thermal mass flow controllers (Bronkhorst) and steam was generated using a steam generator (aDrop). Methane was preheated and mixed with steam at the desired s/c-ratio. A constant volume flow of 100 ml·min$^{-1}$ of nitrogen was used for analytical purposes as an internal standard. The gas mixture was injected into the reactor and preheated in a region of $SiO_2$ (1/8" pellets, Alfa-Aesar). 48 g of the Ni-based catalyst, which was investigated in chapter 3, were used for syngas generation. Prior to the reforming experiments the catalyst was reduced in a stream of 1500 ml·min$^{-1}$ $H_2$ at 750 °C for 5 minutes in order to form catalytically active nickel. The generated syngas was used for the reduction of 189 g of the oxygen carrier. A 1 cm layer of ceramic wool was used to separate the catalyst from the oxygen carrier. A condenser was used to remove non-reacted water from the gas mixture. After the condensation of steam, the dry gas composition was measured using a micro gas chromatograph (Agilent Micro-GC3000) equipped with a Molesieve and a PlotU column using argon and helium as carrier gases. The analysed gases were nitrogen, methane, carbon monoxide, carbon dioxide and hydrogen. After reduction the system was purged for several minutes using nitrogen to remove unreacted gases. Afterwards the oxygen carrier was re-oxidised with steam. The micro gas chromatograph or an assembly of a mass flow controller (Bronkhorst) and a gas analyser (ABB) for carbon monoxide detection was used. The reactor-system was made of high-performance stainless steel and was heated

electrically. The temperature was measured using an N-type thermocouple placed in the preheating zone of the reactor. For SMR and reduction the temperature was fixed to 800 °C, the oxidation was carried out at 600 °C or 800 °C.
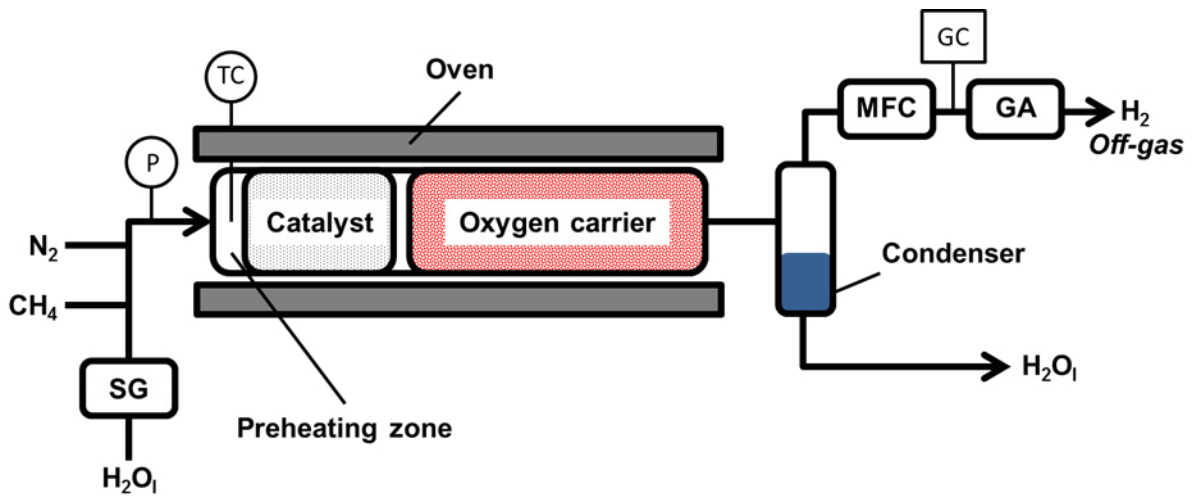


**Figure 33: Schematic illustration of the experimental system consisting of a steam generator (SG), pressure and temperature sensors (P, TC), a mass flow controller (MFC), a gas chromatograph (GC) and a gas analyser (GA).**

As a reference for the SMR-reaction, the equilibrium concentration of the reaction was calculated using the commercial software HSC-chemistry 5.11® and the minimisation of the free Gibbs-energy method.

### 5.2.2. Results and Discussion

Figure 34 shows the changing gas composition during the reduction experiment. During the first minutes low amounts of carbon monoxide and hydrogen but a high carbon dioxide concentration was detected. The amount of hydrogen strongly increased during the first 20 minutes and increased slightly during the following 100 minutes before it reached an almost stable plateau. Carbon monoxide showed the same behaviour while carbon dioxide showed the opposing trend. Although fresh haematite was used for this experiment no period of complete syngas conversion was detected. This indicates a kinetic limitation of the reaction due to the high amount of reactive gases. The methane concentration slightly decreased during the first 80 minutes. This behaviour cannot be explained for sure but an incomplete reduction of the nickel oxide during the catalyst activation step might be the reason. If a significant amount of the catalyst is still oxidised at the beginning of the reaction this would lead to a reduced catalytic activity. In this case the hydrogen and carbon monoxide of the produced syngas would reduce the nickel oxide to catalytic active nickel and, therefore, the methane conversion increases because of the increasing amount of catalyst. This behaviour is well known for chemical looping combustion using nickel based oxygen carriers [37].
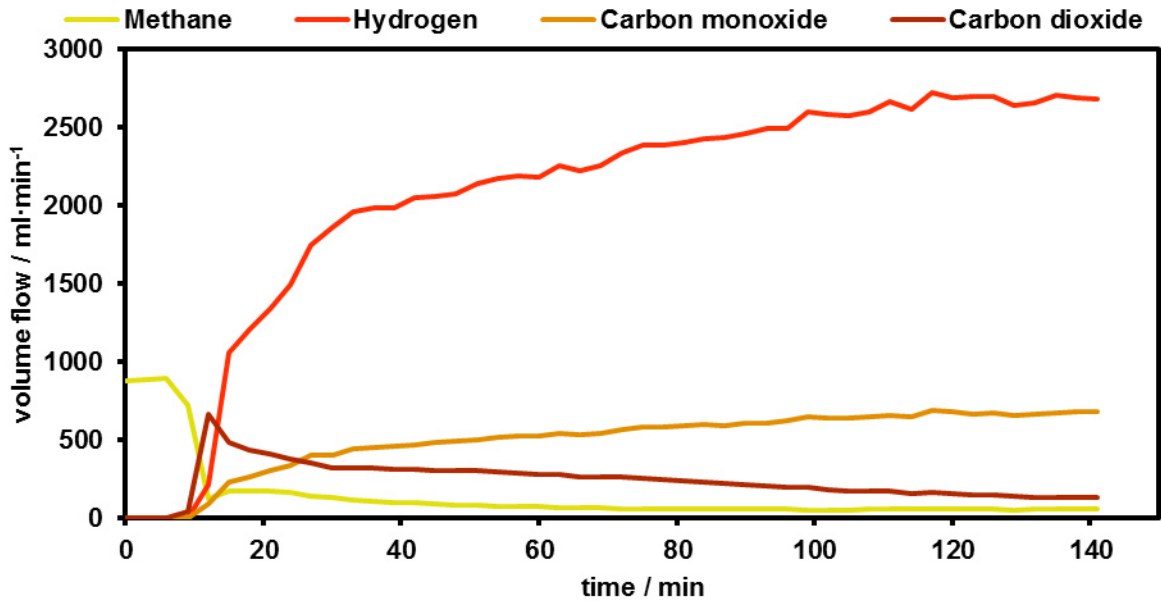
**Figure 34: The off-gas composition of the reformer-steam iron reactor during the reduction; $T_{Red}$=800°C, CH$_4$=880 ml· min$^{-1}$ s/c=1.2.**

Figure 35 gives the comparison between the thermodynamic equilibrium concentration of the SMR reaction and the measured gas composition at the end of the reduction experiment after 140 minutes. The measured data is in good accordance with the thermodynamic predictions. Methane conversion and carbon monoxide content are slightly below the calculation while carbon dioxide and hydrogen are slightly above. Figure 35 also represents the data from the consecutive steam-oxidation step. A maximum hydrogen production of 1170 ml·min$^{-1}$ was measured at the beginning of the reaction. The hydrogen production decreased continuously and after 140 minutes no further hydrogen formation was measured. Small amounts of carbon monoxide and carbon dioxide were measured during the oxidation experiment and indicate coke formation during the prior reduction. Since the detection of carbon monoxide is limited at low concentrations and the micro-GC was only calibrated for concentrations between 1% and 100% an additional two-point calibration was performed (Figure-A I). The amount of carbon monoxide and carbon dioxide was below 500 ppm during the first 80 minutes. Then their concentration increased while the hydrogen concentration decreased. Several effects can cause this behaviour. At the end of the oxidation, when most of the oxygen carrier is oxidised, the overall amount of gases is lower since almost no hydrogen is formed anymore. High quantities of unreacted steam are present to oxidise solid carbon and, therefore, the amount of produced carbon monoxide and carbon dioxide increases. The volume flow of carbon monoxide and carbon dioxide is given in Figure-A I in the appendix. Since the amount of hydrogen decreases the measured concentrations of carbon monoxide and carbon dioxide are further increased. A second explanation for the increase of carbon monoxide and carbon dioxide formation at the end of the reaction might be an uneven distribution of carbon within the reactor. If solid carbon is mainly present near

the outlet of the reactor it can only be oxidised when sufficient steam reaches the outlet section of the reactor which is the case at the end of the oxidation. The results of the steam-oxidation are summarised in Table 10.
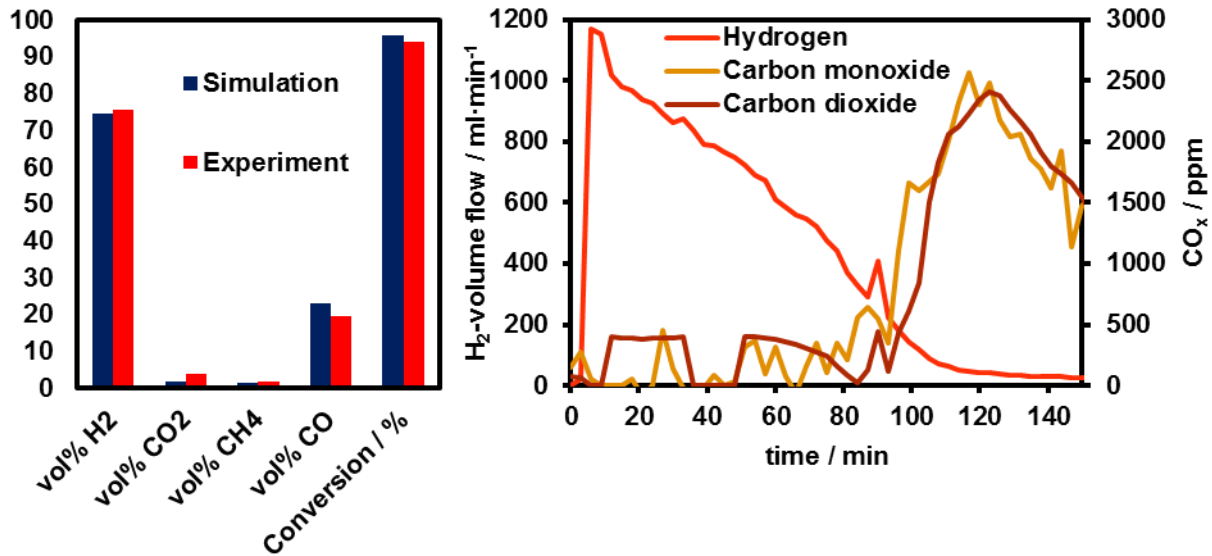


**Figure 35: The off-gas of the reformer-steam iron reactor after completed reduction (left), oxidation reaction vs. time (right); $T_{Ox}$=600 °C, $H_2O$=0.7 g·min$^{-1}$.**

**Table 10: Total volumes and concentrations of the steam-oxidation experiment.**

| Species | Total volume / ml | Concentration / % |
|---|---|---|
| Hydrogen | 67274 | 99.91 |
| Carbon dioxide | 34 | 0.05 |
| Carbon monoxide | 28 | 0.04 |

The measured hydrogen volume of 67 litres is too high since the calculated amount of consumed syngas equivalents (Eq. (23)-(25)) was only 55 litres.

$$SEQ_{in} / ml = 4*CH_{4,\,in} / ml \tag{23}$$

$$SEQ_{out} / ml = 4*CH_{4,\,out} + CO_{out} + H_{2,\,out} \tag{24}$$

$$SEQ\,con / ml = SEQ_{in} - SEQ_{out} \tag{25}$$

The used 189 g of the 90 wt% $Fe_2O_3$ oxygen carrier enable the formation of only 63.6 litre of hydrogen. This represents the maximum volume of hydrogen that can be produced. The measured 67 litres are 6% above this value and 23% higher than the amount of consumed syngas equivalents. The difference between consumed and produced species and the more than 100% oxygen carrier conversion are explained as an over-detection of hydrogen. If the measured hydrogen value is too high it has two effects. The amount of consumed syngas

equivalents is calculated from the measured volume flow rates of unreacted gas. Therefore, an over-detection of hydrogen during the reduction leads to a lower amount of consumed syngas equivalents. During the oxidation, when the amount of produced hydrogen is measured, the over-detection leads to an increased hydrogen value. Therefore, the errors during reduction and oxidation do not abolish each other but add up. The phenomenon of over-detection of hydrogen was proven by a reference measurement using an electrochemical method for hydrogen quantification. A detailed study of the method was published in the International Journal of Hydrogen Energy [110]. The difference between the two measurement methods is shown in Figure-A II in the appendix. Due to the fact that this electrochemical method is not suitable for the detection of other species than hydrogen it was no alternative to the used micro GC for the experiments. The peak value of hydrogen production was 1170 ml·min$^{-1}$ but the 0.7 g·min$^{-1}$ water which were evaporated enable the formation of only 890 ml·min$^{-1}$ hydrogen. This difference cannot be explained by the over-detection of hydrogen. A possible explanation is a drift of the water pump. The amount of pumped water was not measured online. Only the weight of the water supply tank was measured at the beginning and at the end of the reaction and a decrease of steam generation during the oxidation might have happened. This would mean that a steam flow higher than 0.7 g·min$^{-1}$ was pumped at the beginning.

In order to evaluate the effect of the steam to methane ratio on the performance of the system an additional cycle was performed.
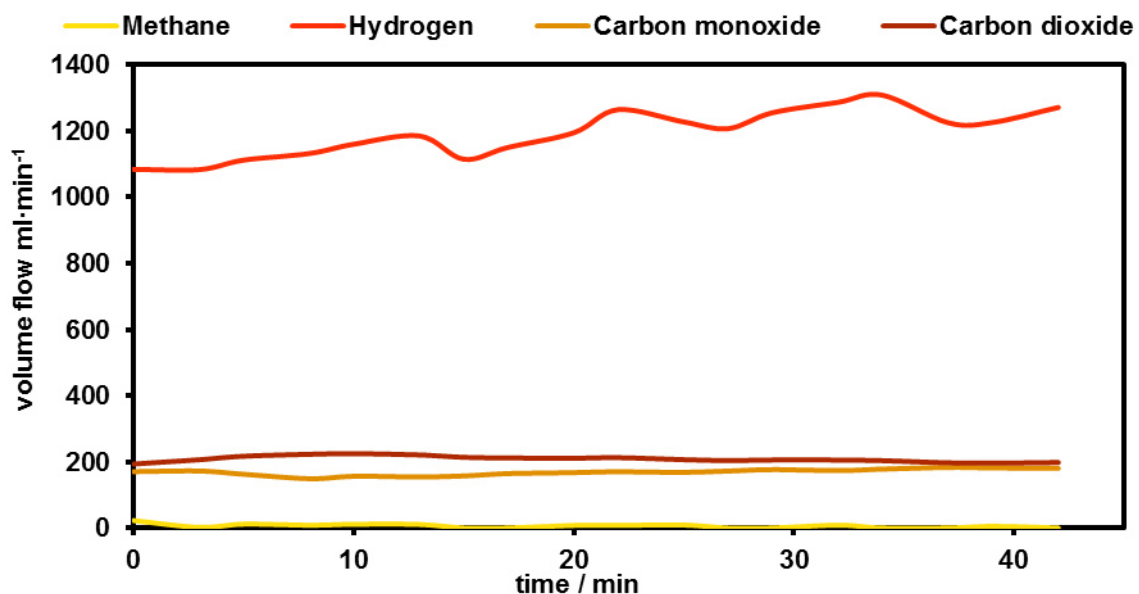


**Figure 36: The off-gas composition of the reformer-steam iron reactor during the reduction; T$_{Red}$=800 °C, CH$_4$=380 ml·min$^{-1}$ s/c=2.8.**

Figure 36 shows the results of the reforming and reduction experiment. At this experiment the carbon monoxide and carbon dioxide concentrations stayed almost constant. Only a very

small increase of carbon monoxide occurred. Also the hydrogen flow was almost constant compared to the results given in Figure 34. This indicates low reactivity caused by massive degradation of the oxygen carrier. Figure 37 shows the results of the reduction and oxidation experiments. The off-gas composition at the end of the reduction experiment (left) is in good accordance with the equilibrium concentration of the SMR-reaction, which indicates full conversion of the accessible parts of the oxygen carrier during the reduction. The oxidation experiment led to the formation of hydrogen with minor impurities of carbon monoxide (right). In order to get more valid data the gas measurement was changed for the oxidation reaction. To get better information on the purity of the produced hydrogen a gas analyser, with lower carbon monoxide detection limits (ABB), was used to determine the quality of the produced hydrogen. For better hydrogen quantification a thermal mass flow controller was used as a gas flow meter. A maximum amount of 1000 ml·min$^{-1}$ hydrogen was produced at the beginning of the reaction which equals 59% of steam conversion.
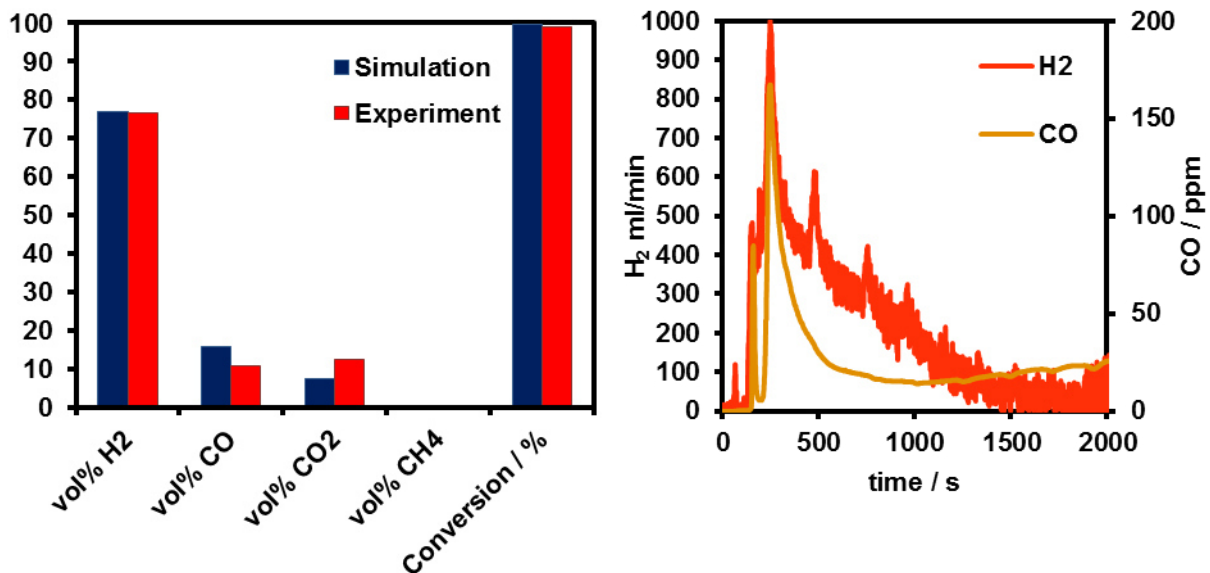


**Figure 37: The off-gas of the reformer-steam iron reactor after completed reduction (left) and oxidation reaction vs. time; $T_{Ox}$=800 °C, $H_2O$ = 1.4 g·min$^{-1}$ (right).**

A peak of 167 ppm carbon monoxide was detected at the beginning of the oxidation which indicates the deposition of solid carbon during the reduction via the decomposition of non-reacted methane or the Boudouard-reaction (Eq. (17)). The high amount of carbon monoxide at the end of the reaction can easily be explained by the experimental setup. At the end of the reaction no further hydrogen is produced and, since no nitrogen was used as an internal standard during the oxidation, the product gas only consisted of steam which was condensed before it reached the gas analyser. Therefore, no further gas flow arrived at the analyser and the carbon monoxide content stayed almost constant when no further hydrogen was produced. The results of the steam-oxidation are summarised in Table 11.

**Table 11: Total volumes and concentrations for the steam-oxidation experiment.**

| Species | Total volume / ml | Concentration / % |
|---------|-------------------|-------------------|
| Hydrogen | 6982 | 99.996 |
| Carbon monoxide | 0.29 | 0.004 |

The total amount of produced hydrogen was 6982 ml and the consumed syngas equivalents were 6372 ml which equals a difference of 9.6%. The reason for this deviation again can be found in the hydrogen over-detection by the micro-GC during the reduction. While the total amount of produced hydrogen was rather low a high purity of only 42 ppm carbon monoxide was achieved. Carbon dioxide was not measured during this experiment since the gas analyser was not calibrated for this species but thermodynamic calculations predict an equimolar ratio of carbon monoxide and carbon dioxide at the given temperature (Figure-A III in the appendix). Two reasons for the low amount of impurities can be found. Number one is the higher s/c-ratio which reduces the risk of coke formation in general. The second factor is the reaction time. At the beginning of the reduction step sufficient oxidised iron is present and the oxidation of syngas and unreacted methane can occur (Eq. (5) and (10)). During the reduction the amount of oxidised solid decreases and, therefore, a higher risk of coke formation is given. Thus, a shorter reaction time should decrease the amount of solid carbon. This effect was already pointed out in section 2 of this thesis. Figure 38 and Figure 39 show the equilibrium composition for SMR as a function of the reformer temperature at the investigated s/c-ratios of 1.2 and 2.8. At s/c=1.2 the reaction temperature of 800 °C should be high enough to avoid the formation of solid carbon and at s/c=2.8 the formation of solid carbon should not occur in general. Nevertheless, during both oxidations the formation of solid carbon could not be avoided completely and led to carbon monoxide and carbon dioxide impurities in the produced hydrogen. Beside the Boudouard reaction (Eq. (17)) the formation of solid carbon can be caused by catalytic decomposition (Eq. (16)) of non-reacted $CH_4$ at iron particles, which are well-known to catalyse this reaction[62,63]. If the reactions (16) or (17) are catalysed but the re-oxidation of carbon with steam or $CO_2$ is not, a net production of solid carbon occurs even if it is not favoured by the thermodynamic equilibrium. An insufficient temperature distribution can be excluded at least at the s/c-ratio of 2.8 since carbon formation is not favoured over the whole temperature range from 250 - 1250 °C. A drift or pulsation of the steam generation system might be an additional explanation for the formation of solid carbon during the reduction reaction since insufficient steam supply causes the direct decomposition of methane at high temperatures.
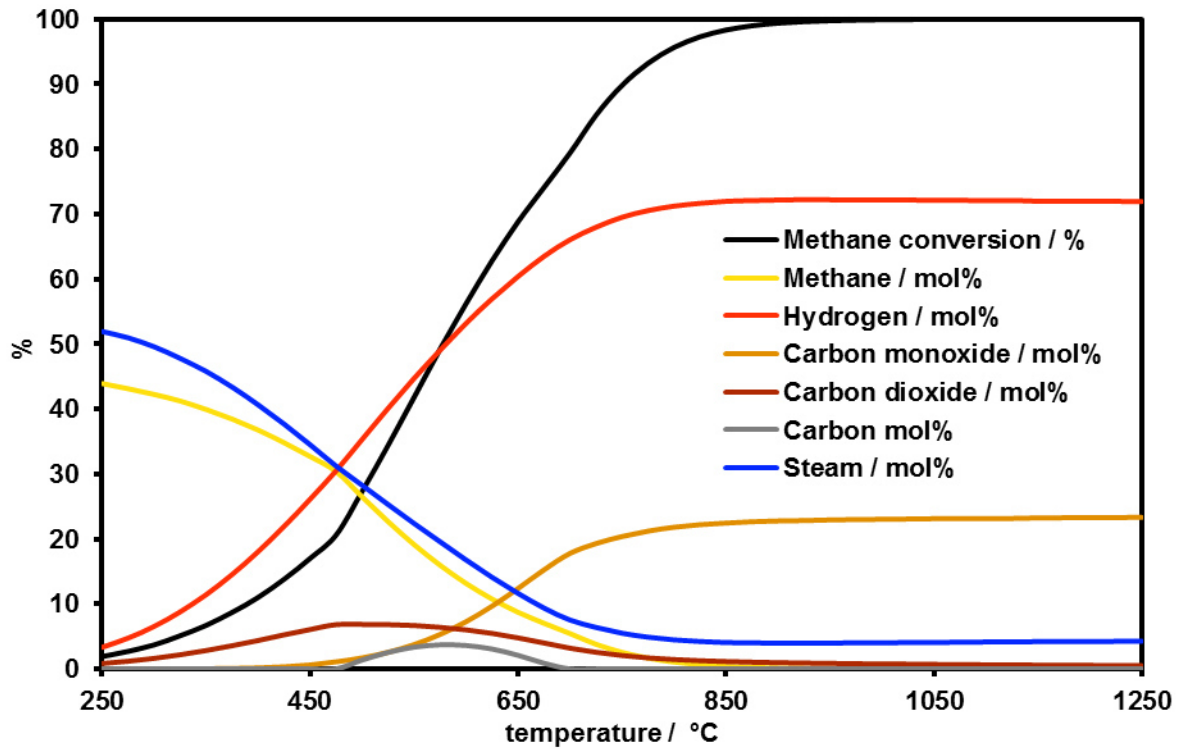
**Figure 38: Equilibrium composition and CH₄-conversion for SMR at an s/c-ratio of 1.2 as a function of temperature.**
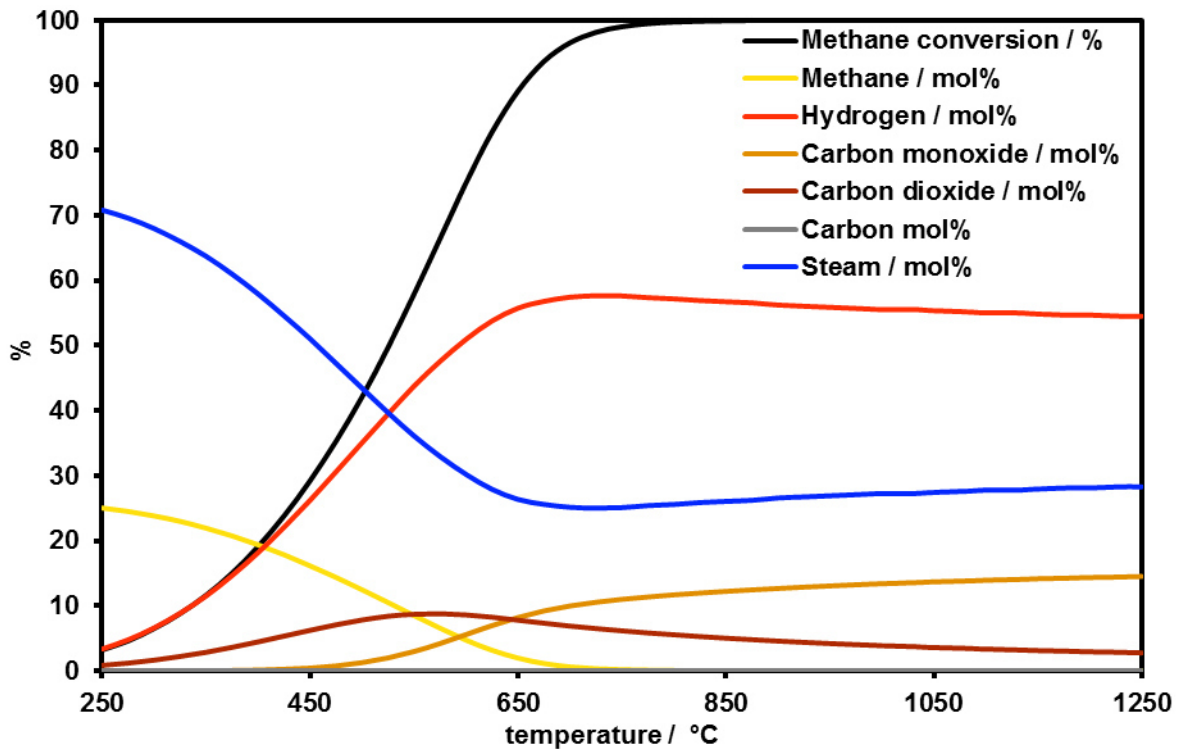


**Figure 39: Equilibrium composition and CH₄-conversion for SMR at an s/c-ratio of 2.8 as a function of temperature.**

The presented results show the proof of concept of the novel reactor configuration for steam reforming and the steam iron process. Possible sources of errors were identified during the experiments. The CO content is on the limit of the detection system and the micro GC showed an over-estimation of hydrogen. Nevertheless, the experiments proved the feasibility of the approach of using a multi fixed bed reactor for the production of pure hydrogen in one compact device. The nickel based catalyst which was investigated in section 3 of this thesis showed an excellent performance at 800 °C and low steam to carbon ratios and the quality of the produced hydrogen was high. Based on these promising results the prototype for the production of pure hydrogen was developed.

## 5.3.     Prototype operation

### 5.3.1.  Experimental

The multi-fixed bed reactor developed for the flex fuel reformer consists of 5 different layers of solid material (Table 12, Figure 29 and Figure 40). The commercial available nickel based catalyst, already described in the sections 3.2.1 and 5.2 of this thesis was used for the conversion of methane and artificial biogas mixtures to syngas. 300 g of an 80 wt% $Fe_2O_3$ (325 mesh, Alfa-Aesar) + 20 wt% $Al_2O_3$ (20-50 µm, Alfa-Aesar) oxygen carrier were prepared by the procedure described in section 5.2.1 and used for syngas conversion. Three layers of inert material ($Al_2O_3$, 1/8" pellets, Alfa-Aesar) were used to separate catalyst and oxygen carrier as well as for gas mixing and preheating.

**Table 12: Reactor filling of the flex fuel reformer prototype.**

| Layer | Material | Length / mm | Volume / ml | Mass / g |
|:-----:|:--------:|:-----------:|:-----------:|:--------:|
| 1 | Inert | 100 | 91 | 66 |
| 2 | Catalyst | 105 | 96 | 96 |
| 3 | Inert | 195 | 178 | 129 |
| 4 | Oxygen carrier | 212 | 204 | 300 |
| 5 | Inert | 388 | 373 | 270 |

The dry gas composition was measured with a micro gas chromatograph (Agilent Micro-GC 3000) equipped with a Molesieve and a PlotU column using argon and helium as carrier gases or with a gas analyser (ABB) for carbon monoxide detection. Nitrogen was used as an internal standard for quantification purpose. The analysed gases were nitrogen, methane, carbon monoxide, carbon dioxide and hydrogen. Between reduction and oxidation the system was purged for several minutes with nitrogen or hydrogen.
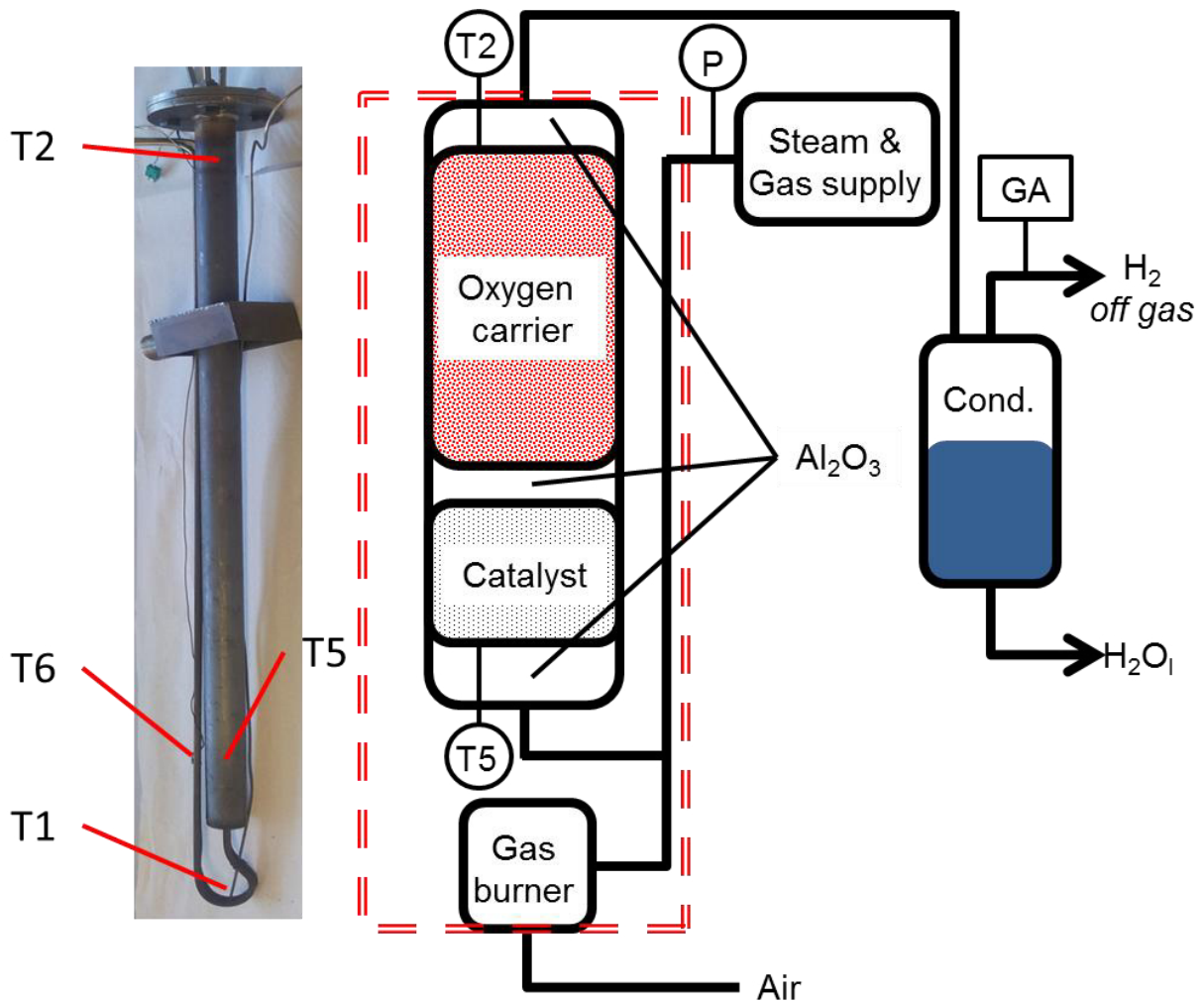
**Figure 40: Photography and simplified illustration of the multi-fixed bed assembly, thermocouples (T1-6) pressure sensor (P) condenser (Cond.) and gas analysis (GA); the heated region is highlighted red.**

Six thermocouples (type K and type N) were used to investigate the heat distribution and the off-gas temperature of the flex fuel reformer prototype (Figure 40 and Figure-A V-appendix). The thermocouples were placed at the lowest point of the reactor near the flame (T1), in the outlet section of the oxygen carrier (T2), in the insulation of the reactor (T3), in the off-gas stream of the burner (T4) in the inlet section of the catalyst region (T5) and at the outer reactor wall (T6) at the same height as (T5). Temperatures above 900 °C were avoided to prevent the reactor from taking damage. 700 °C were defined as the minimum temperature of the system in order to achieve high conversion rates. Gases were supplied using thermal mass flow controllers (Bronkhorst). Prior to the reforming experiments the catalyst was reduced in a stream of 100 ml·min$^{-1}$ H$_2$ for several minutes. Five cycles consisting of a reforming and reduction step followed by a steam-oxidation step were performed. The experiments were carried out in order to determine the power output of the prototype, to

measure the purity of the produced hydrogen and to evaluate the overall performance of the system. Table 13 summarises the basic characteristics of the 80 + 20 wt% oxygen carrier as well as the theoretically consumed respectively produced amounts of hydrogen and carbon monoxide. Table 14 summarises the experimental conditions of the cycles.

**Table 13: Oxygen carrier characteristics and gas demand respectively production for the different reactions.**

| Oxygen carrier characteristics | g | mol | ml |
|---|---|---|---|
| total mass | 300 | - | - |
| $Fe_2O_3$ / g | 240 | 1.50 | - |
| $Fe_3O_4$ / mol | 232 | 1.00 | - |
| Fe / mol | 168 | 3.01 | - |
| $H_2$/CO consumption resp. generation | | | |
| $Fe_2O_3 \rightarrow$ Fe | - | 4.51 | 100989.4 |
| $Fe_3O_4 \leftrightarrow$ Fe | - | 4.01 | 89768.3 |

**Table 14: Experimental conditions of four cycles.**

| Cycle | Species | Flow rate |
|---|---|---|
| Reduction 1 | $CH_4$ | 236±6 ml·min$^{-1}$ |
| | $H_2O$ | 0.5 g·min$^{-1}$ |
| Oxidation 1 | $H_2O$ | 1.1 g·min$^{-1}$ |
| Reduction 2 | $CH_4$ | 275±4.5 ml·min$^{-1}$ |
| | $CO_2$ | 250 ml·min$^{-1}$ |
| | $H_2O$ | 0.6 g·min$^{-1}$ |
| Oxidation 2 | $H_2O$ | 1.1 g·min$^{-1}$ |
| Reduction 3 | $CH_4$ | 459.4±12.9 ml·min$^{-1}$ |
| | $H_2O$ | 0.9 g·min$^{-1}$ |
| Oxidation 3 | $H_2O$ | 0.9 g·min$^{-1}$ |
| Reduction 4 | $CH_4$ | 529.4±11.5 ml·min$^{-1}$ |
| | $CO_2$ | 692.5 ml·min$^{-1}$ |
| | $H_2O$ | 0.45 g·min$^{-1}$ |
| Oxidation 4 | $H_2O$ | 0.9 g·min$^{-1}$ |

At the fifth cycle the methane flow was changed several times during the experiment in order to determine the maximum conversion rate of the system. The corresponding data for this cycle is given in Table 15 in section 5.3.2.

### 5.3.2. Results and Discussion

**Cycle 1:**

The first cycle was conducted in order to prove the operational capability of the prototype and to get basic performance data of the system. The temperature profile of the prototype is given in Figure 41. The temperature measured directly above the flame at the lowest point of the reactor (T1) rose to 850 °C within 45 minutes. The desired inlet temperature (T5) of 800 °C was reached after 80 minutes while it took 160 minutes to reach the defined minimum temperature of 700 °C in the outlet section (T2). Off-gas and insulation temperatures of over 600 °C were measured (T3 and T4) which indicates the high potential of heat recovery to improve the system. This issue will be addressed in section 5.4 of this thesis.
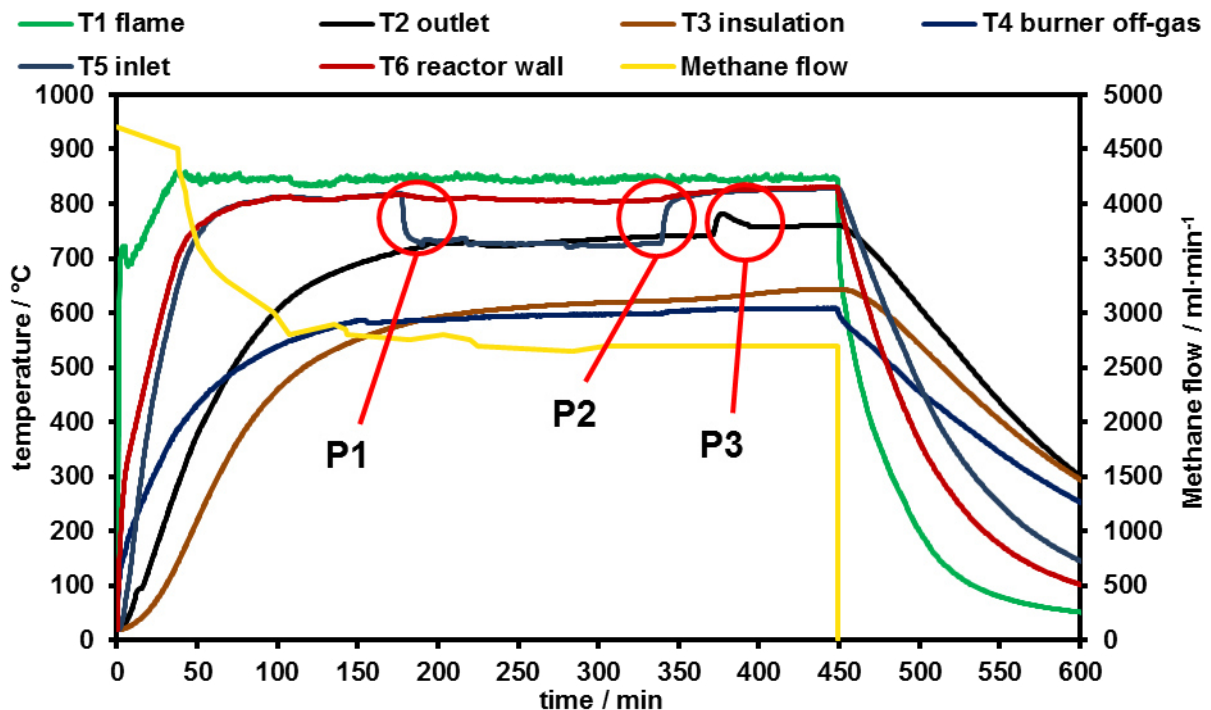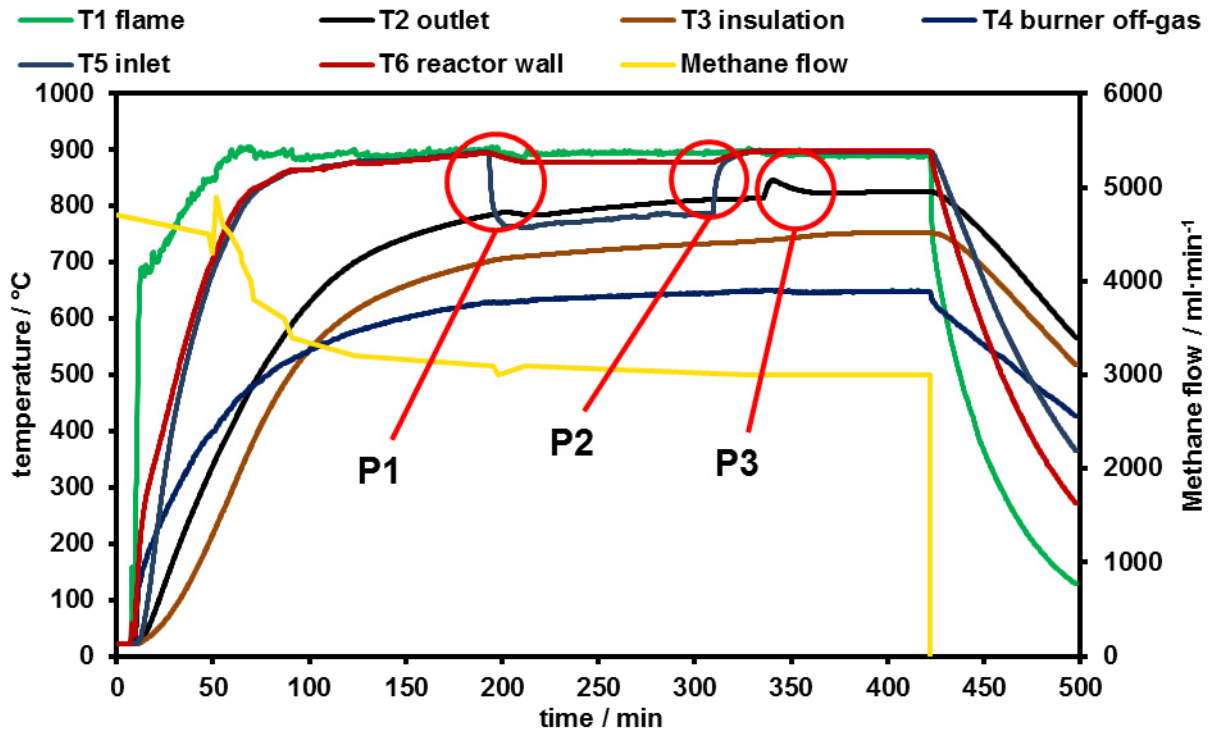


**Figure 41: Temperature profile and methane flow of the complete cycle 1; highlighted points are: P1-start of the reforming reaction, P2-end of the reforming reaction and P3-start of the oxidation reaction.**

Before the start of the reforming reaction (P1) the reactor wall temperature (T6) was at the same level as T5 which indicates an almost equal temperature distribution inside and outside the reactor. After the start of the reforming reaction the temperature in the catalyst region (T5) decreased to 725 °C within a few minutes. This temperature drop was directly caused by the highly endothermic SMR reaction taking place within the catalyst region of the reactor since the outlet temperature of the reactor was not influenced and T2 stayed at a constant temperature. At the end of the reforming reaction (P2) methane and steam were switched off and T5 returned to 820 °C. The methane flow to supply the gas burner was decreased several times to optimise the fuel consumption while keeping all temperatures within the

80

specifications. After a short purging phase steam was fed into the system. Since reforming/reduction and oxidation are conducted at reversed flow mode T2 represents the steam inlet section during the oxidation. At the beginning of the oxidation phase (P3) temperature T2 increased from 740 °C to 780 °C because of the exothermic steam-oxidation reaction. After 450 minutes the experiment was stopped and methane supply was turned off. During the cooling phase the system was purged with nitrogen in order to avoid contamination of the oxygen carrier with air. Figure 42 shows the dry gas flows measured during the first cycle. During the heating-up step the system was purged with nitrogen and a stream of 100 ml·min$^{-1}$ H$_2$ was used for the activation of the catalyst before CH$_4$ was fed into the reactor. During the whole reduction experiment methane was completely consumed. In the first period of the reduction experiment carbon dioxide was the only detected product because of the presence of sufficient haematite for complete syngas conversion. After 20 minutes the carbon dioxide concentration decreased while carbon monoxide and hydrogen were detected which indicates the almost complete reduction of haematite.
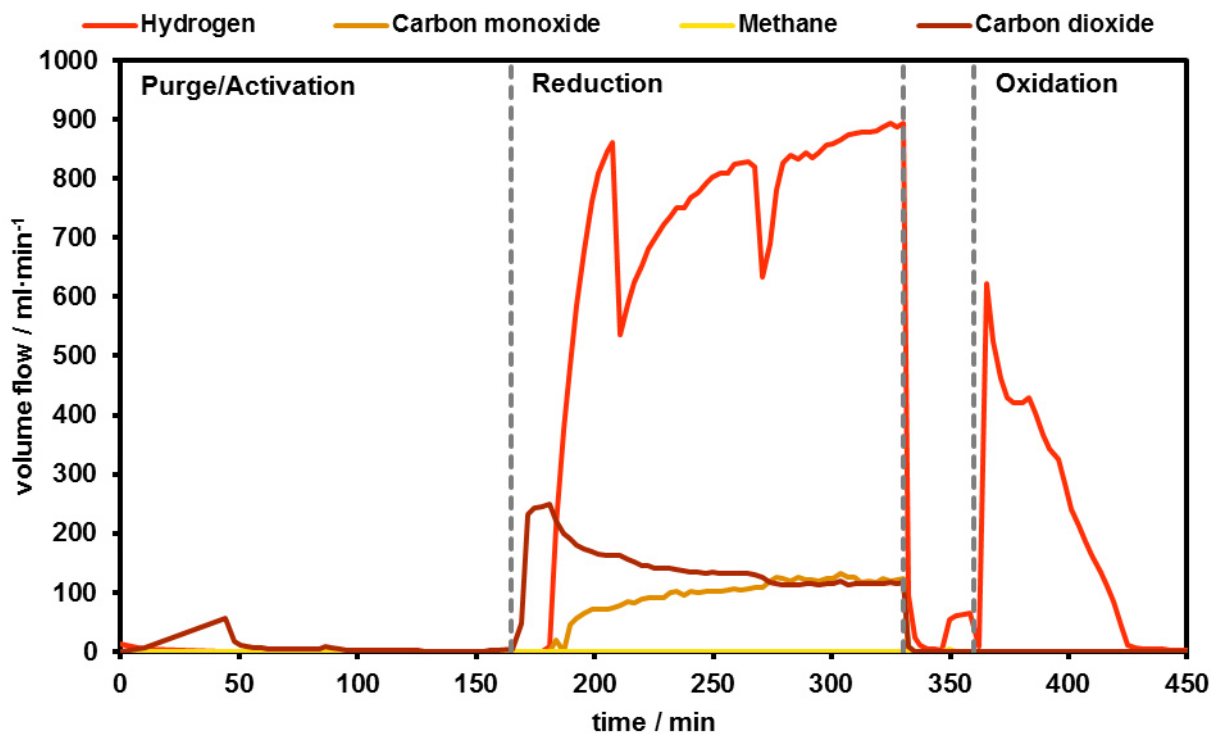


**Figure 42: Dry gas composition during the first cycle measured with a micro GC; note that the time is not synchronised with Figure 41.**

For the next 150 minutes carbon dioxide slightly decreased while carbon monoxide and hydrogen increased. The two discontinuities in the hydrogen signal are caused by insufficient steam supply which also affected the carbon monoxide and dioxide signals to some minor degree. No stable plateaus and, therefore, no distinct regions for magnetite → wustite or wustite → iron transitions were identified during the reduction experiment. After 330 minutes

steam and methane were turned off. Afterwards the system was purged with nitrogen and hydrogen in order to remove unreacted components from the system. Then steam and nitrogen were fed from the opposite side into the system in order to produce hydrogen. A total amount of 18,689.9 ml hydrogen (99.89% purity) was produced. Only carbon dioxide was detected as contaminant but the micro GCs detection limit for carbon monoxide is high and, therefore, the formation of carbon monoxide cannot be excluded for sure. The maximum hydrogen flow was 621.5 ml·min$^{-1}$ (0.111 kW based on the lower heating value of hydrogen) which equals a maximum steam conversion of 45%.

**Cycle 2:**

Figure 43 shows the temperature profile of the prototype during the second cycle. A mixture of methane and carbon dioxide was mixed with steam in order to investigate the capability of the system for biogas reforming. A higher methane flow for the burner was applied in order to reach a higher reaction temperature than the 725 °C achieved in cycle 1. The maximum temperature (T1) was still slightly below 900 °C but now also T5 and T6 reached this value. The catalyst inlet temperature (T5) decreased at the beginning of the reforming/reduction reaction from 890 °C to below 760 °C and a slightly increasing reaction temperature between 760 °C and 785 °C was reached. Also the temperature of the reactor wall slightly decreased during the reforming/reduction reaction and increased afterwards. The higher decrease especially of T5 can be explained by the higher amount of methane and the presence of carbon dioxide. Higher amounts of methane also lead to a higher energy demand of the reforming reaction. In addition, the presence of carbon dioxide further increased the energy demand since the dry reforming reaction (Eq. (22)) is of higher endothermicity than the steam methane reforming reaction. A higher amount of carbon dioxide also increases the reversed water-gas shift reaction (Eq. 4) which also leads to an increased heat demand. Figure 44 shows the dry gas composition measured during the second cycle. Complete methane conversion was achieved also at cycle 2 but no region of full syngas conversion was present since steam-oxidation at cycle 1 only led to the formation of magnetite. As seen at cycle 1 no stable plateau occurred. The consecutive oxidation led to the formation of 17960.2 ml hydrogen (99.79% purity). Also at this cycle carbon dioxide was identified as the only contaminant. The maximum hydrogen flow was 641.3 ml·min$^{-1}$ $H_2$ (0.115 kW based on the lower heating value of hydrogen) which equals a maximum steam conversion of 47%. No increased amount of impurities was detected during the biogas reforming experiments compared to the experiments conducted with pure methane.

**Figure 43: Temperature profile and methane flow of the complete cycle 2; highlighted points are: P1-start of the reforming reaction, P2-end of the reforming reaction and P3-start of the oxidation reaction.**
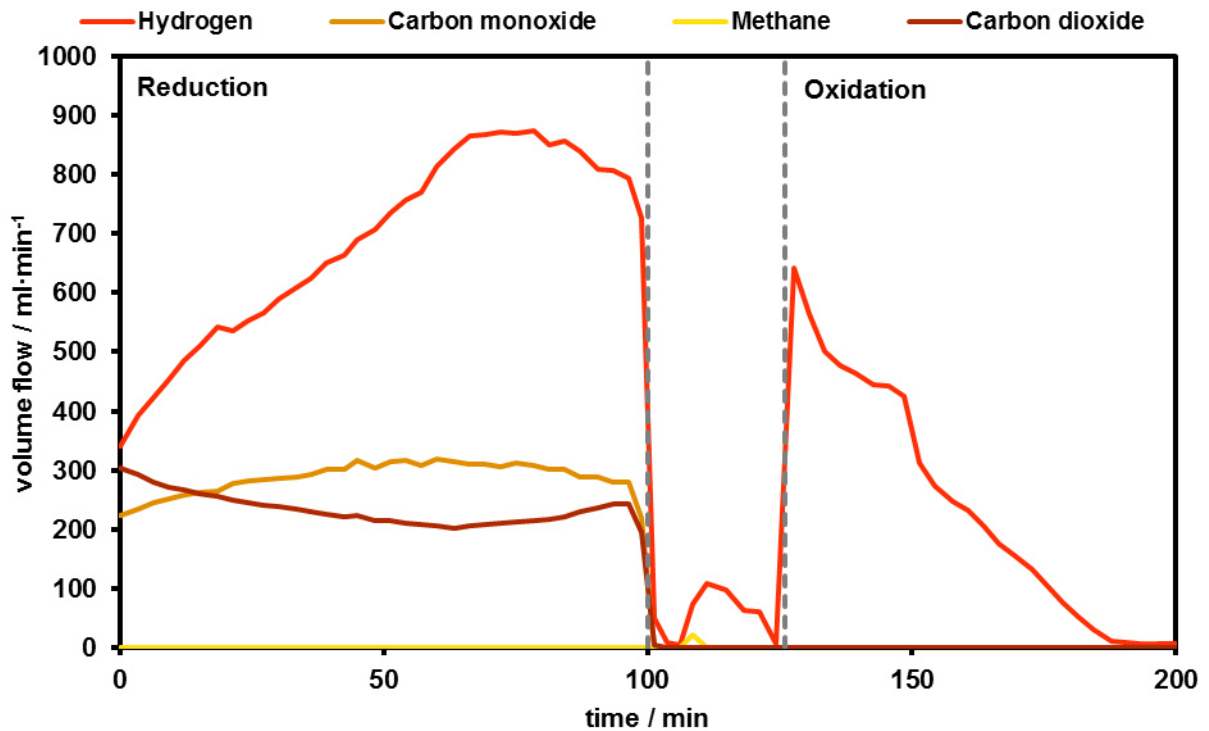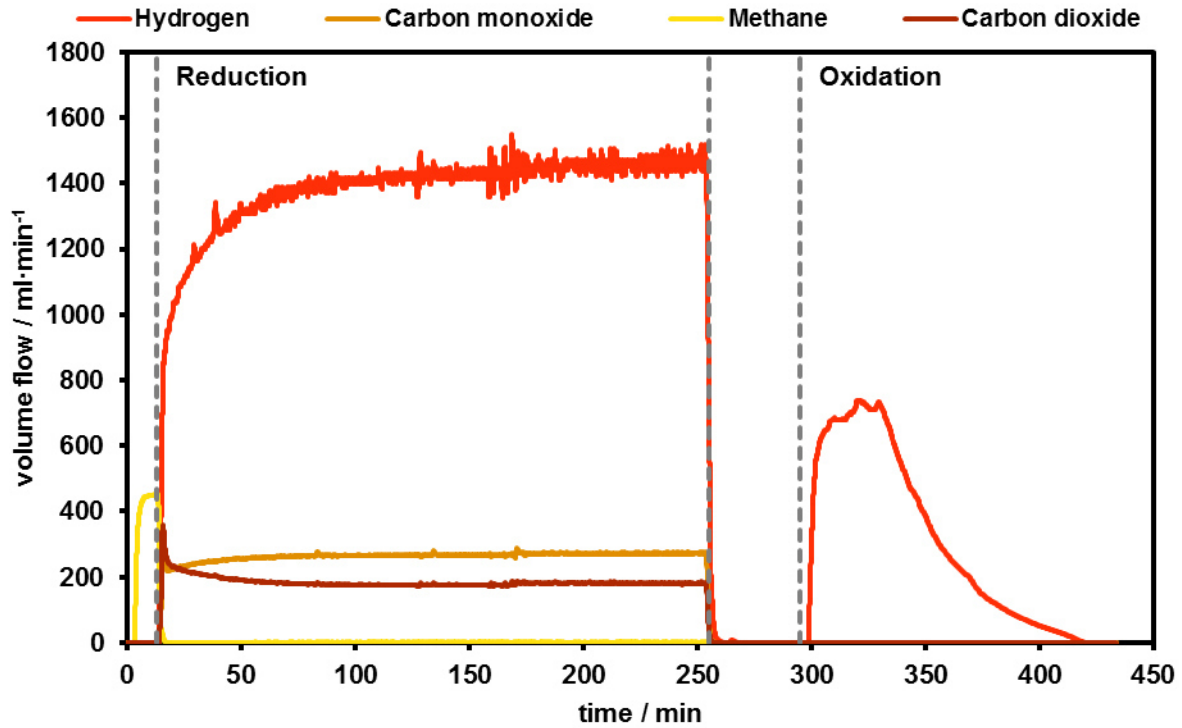


**Figure 44: Dry gas composition during the second cycle measured with the micro GC; note that the time is not synchronised with Figure 43.**
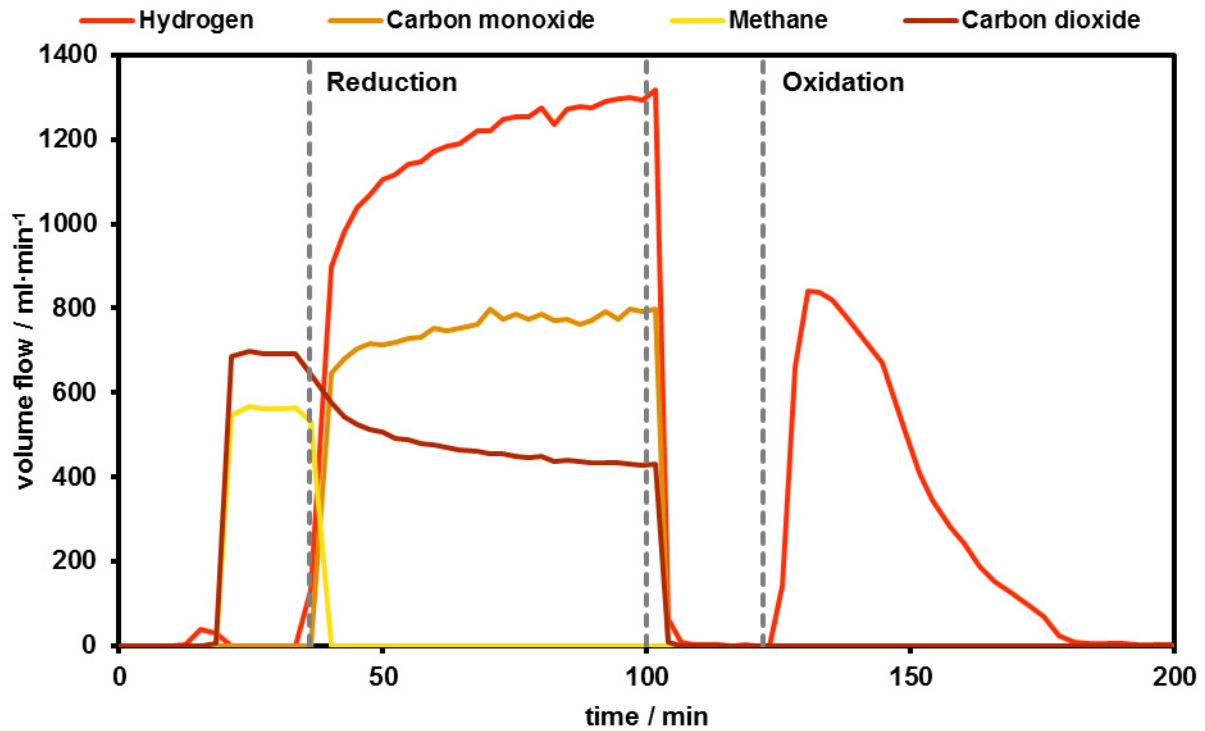
**Cycle 3:**

Figure 45 shows the temperature profile of the third cycle. The reaction temperature (T5) decreased from 895 °C to below 735 °C and also T6 slightly decreased during the reforming/reduction step. Due to the higher amount of methane the temperature drop during this reduction cycle was higher compared to the previous ones. The significantly lower insulation temperature (T3) is caused by an unintentionally changed position of the corresponding thermocouple.
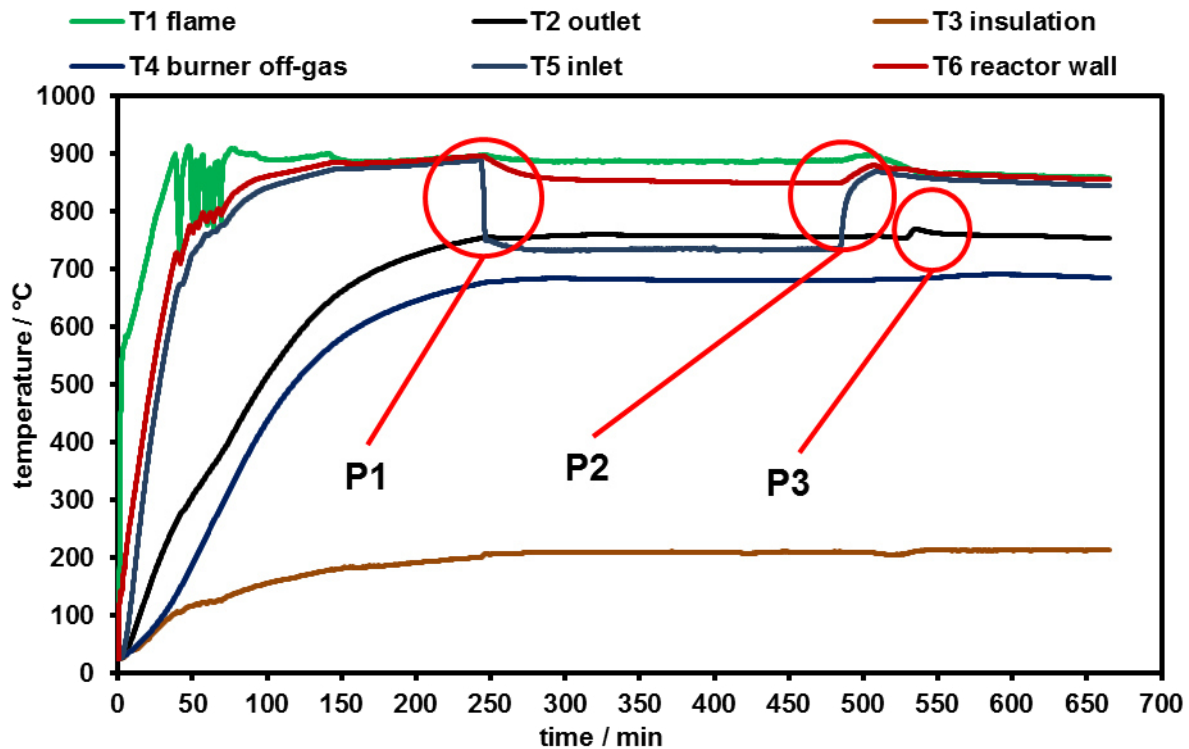


**Figure 45: Temperature profile of the complete cycle 3; highlighted points are: P1-start of the reforming reaction, P2-end of the reforming reaction and P3-start of the oxidation reaction.**

In order to improve the detection limit for impurities during the oxidation and to verify the results in general, a gas analyser (ABB) was used in addition to the micro GC. Figure 46 and Figure 47 show the dry gas flow rates of cycle 3 measured via the different gas analysis systems. In general it can be said that both diagrams show the same trends but differ in detail. The major difference between the two systems is the interval of measurement. While the gas concentration is only measured every 2.5 minutes with the micro GC, one value per second is measured with the gas analyser. Comparing Figure 46 with Figure 47 it can be seen that several peaks or spikes were measured with the GC while at the same time no such values were identified with the gas analyser. This is clearly visible in the purge phase between oxidation and reduction. At the first glance this is unexpected since the shorter measuring interval of the gas analyser should make it more sensitive for such effects but it can be explained by the assembly of micro GC and gas analyser within the experimental

setup. The gas analyser is placed downstream the micro GC. Therefore, pulsations of the system might influence the micro GC more compared to the gas analyser. The cycle is characterised by a very fast increase of hydrogen flow at the beginning followed by only small changes of concentration versus time. This indicates a very slow conversion of oxygen carrier and might be attributed to aging effects of the oxygen carrier. The oxidation led to the formation of 39801.6 ml hydrogen (99.55% purity) measured by the micro GC, respectively 40387.0 ml hydrogen (99.94% purity) measured by the gas analyser. The maximum hydrogen flow was 720.1 ml·min$^{-1}$ (0.129 kW) measured by the micro GC, respectively 739.5 ml·min$^{-1}$ (0.132 kW) measured by the gas analyser. These values equal maximum steam conversion rates of 64% and 66% respectively.
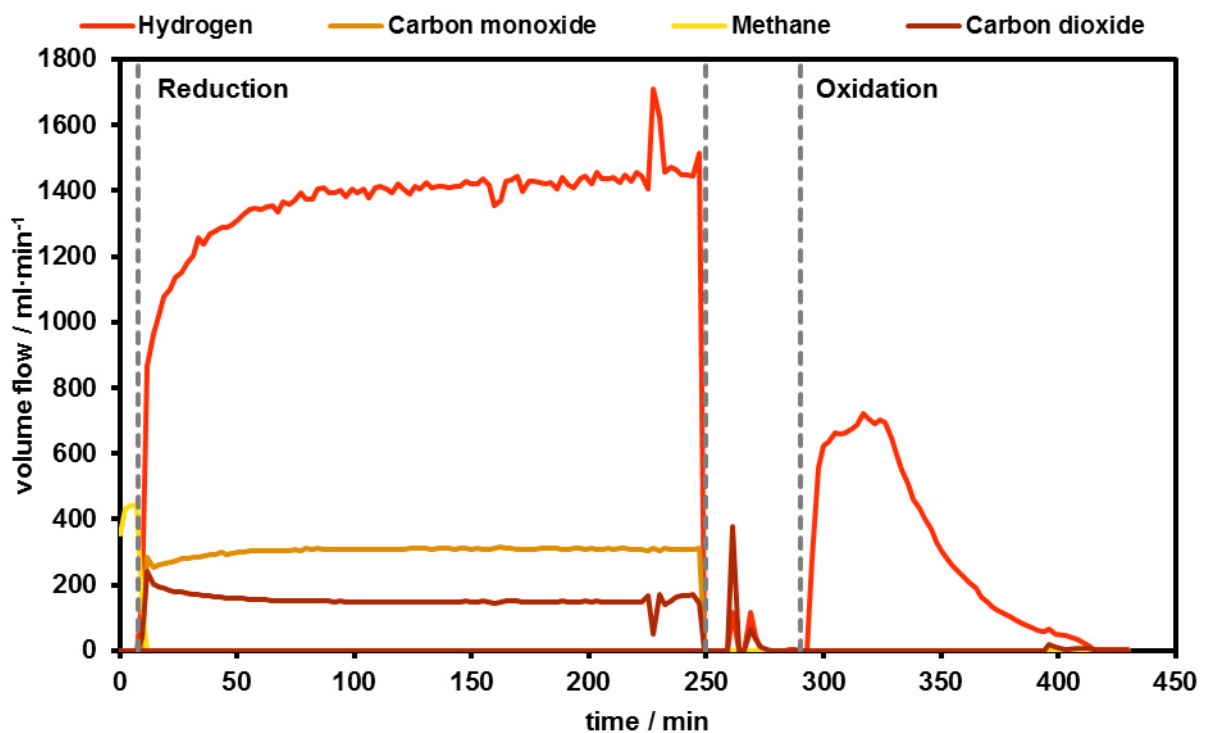


**Figure 46: Dry gas composition during the third cycle measured with the micro GC; note that the time is not synchronised with Figure 45 and Figure 47.**

Beside the shorter measuring interval a lower detection limit is the major advantage of the gas analyser. Figure 48 shows the amounts of impurities produced during the oxidation reaction. Contrary to the results of the micro GC not only carbon dioxide but also carbon monoxide and methane were detected. A very strong random noise of the carbon monoxide and methane signals is clearly visible while the carbon dioxide signal is very clear. This is explained by the effect that the methane and carbon monoxide signals are measured with a detector calibrated for the whole detection range while the carbon dioxide signal is measured with a system solely designed for the measurement of concentrations in the ppm range. Therefore, the overall quantification of the different spices is doubtful.
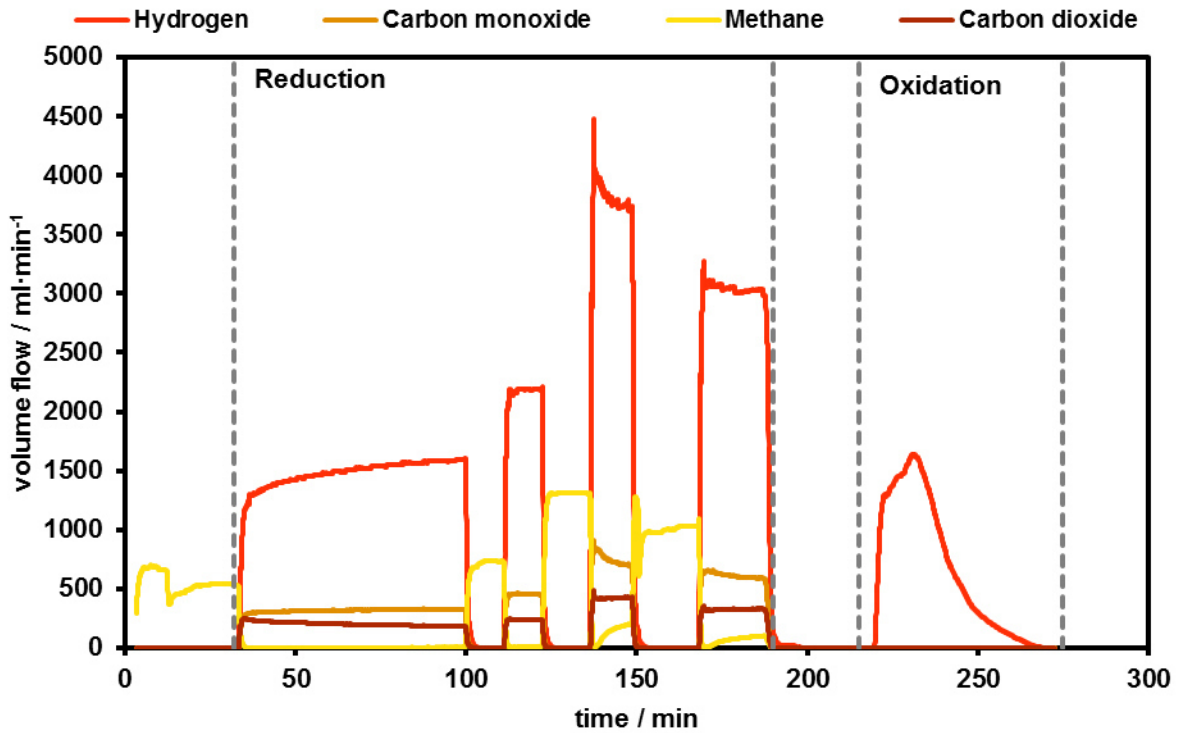
**Figure 47: Dry gas composition during the third cycle measured with the gas analyser; note that the time is not synchronised with Figure 45 and Figure 46.**
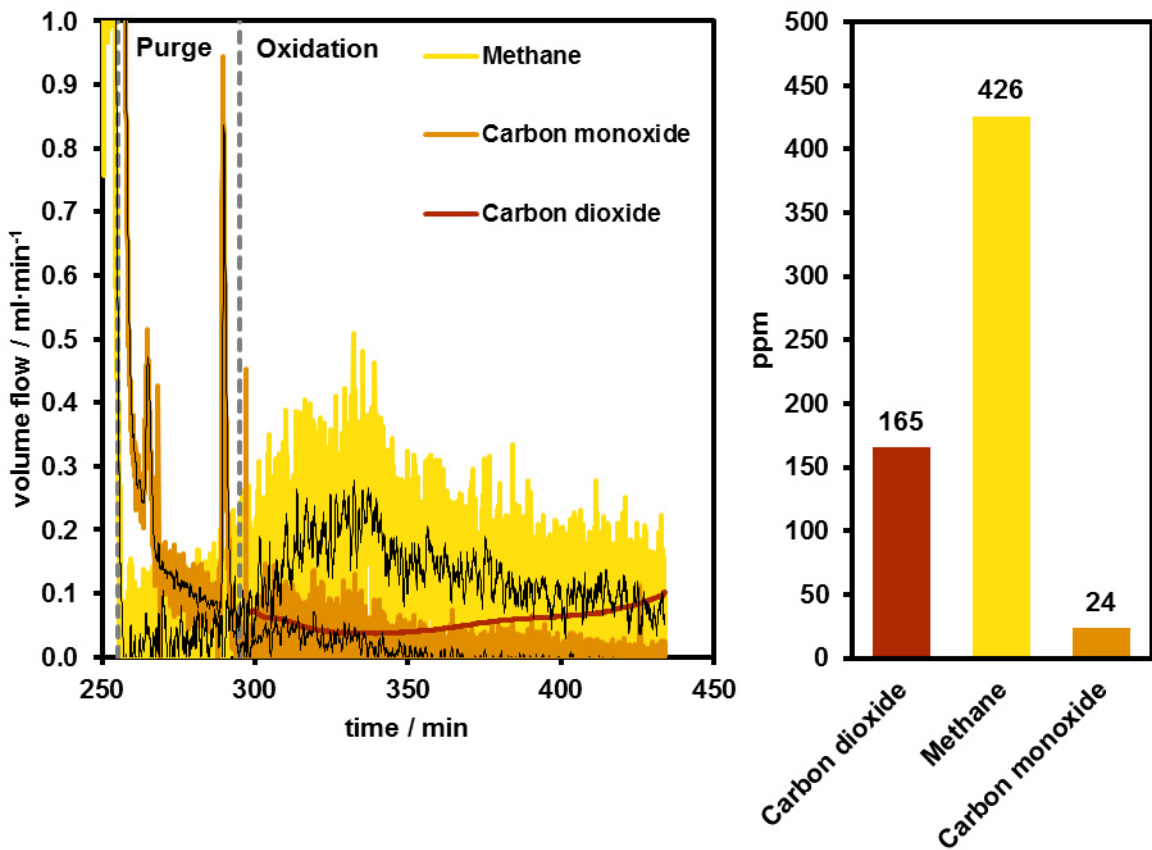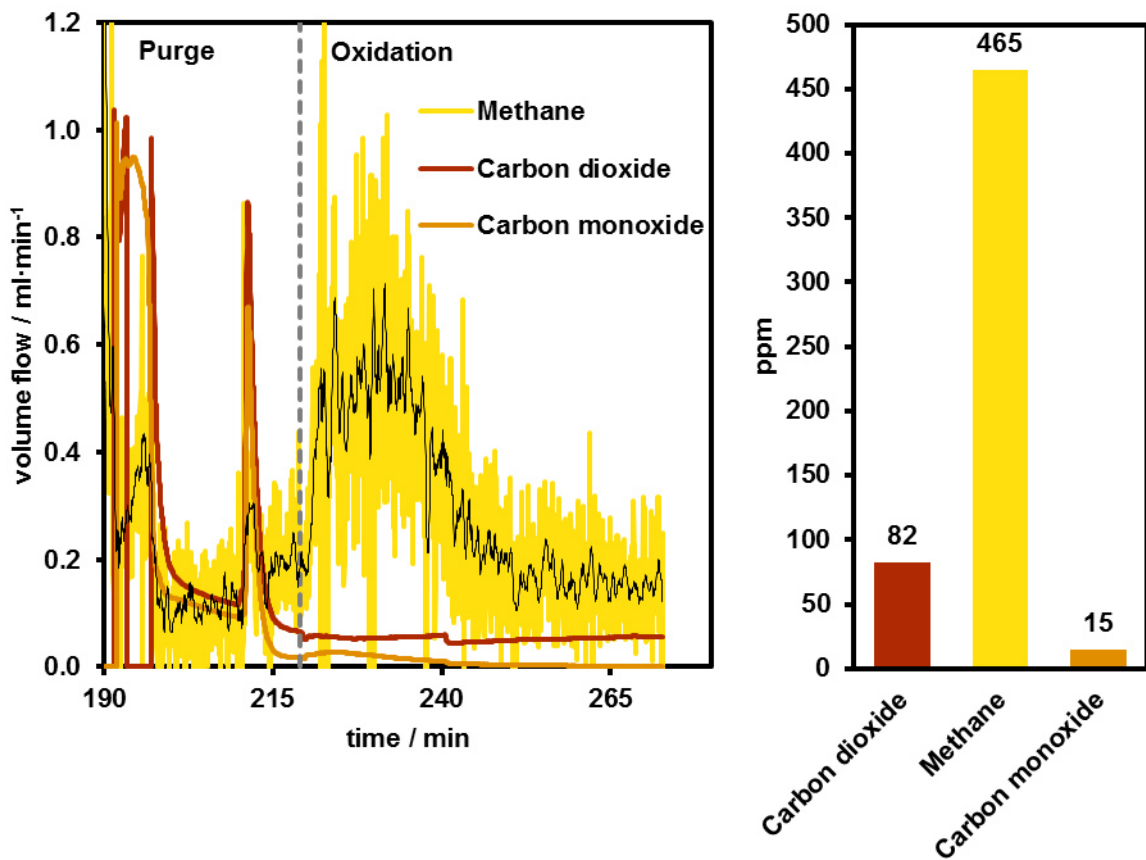


**Figure 48: Impurities during the purge and oxidation phase of cycle 3; black lines are averaged values in order to in increase the signal to noise ratio (left), total amount of impurities (right).**

In addition especially carbon monoxide seems not to be produced during the steam-oxidation but to be a relic of the reduction reaction still present at the end of the purge phase. A significant increase of methane at the beginning of the oxidation is measurable but due to the high random noise it cannot be clearly said if methane is produced during the oxidation via the methanation (Eq. (16)) or the signal is just an error of measurement.

**Cycle 4:**

Cycle 4 represents the second biogas experiment. The temperature at the inlet of the catalyst region (T5) decreased from 860 °C to below 700 °C and also the reactor wall temperature (T6) showed a slight temperature decrease during the reduction due to the high amount of methane and carbon dioxide present.
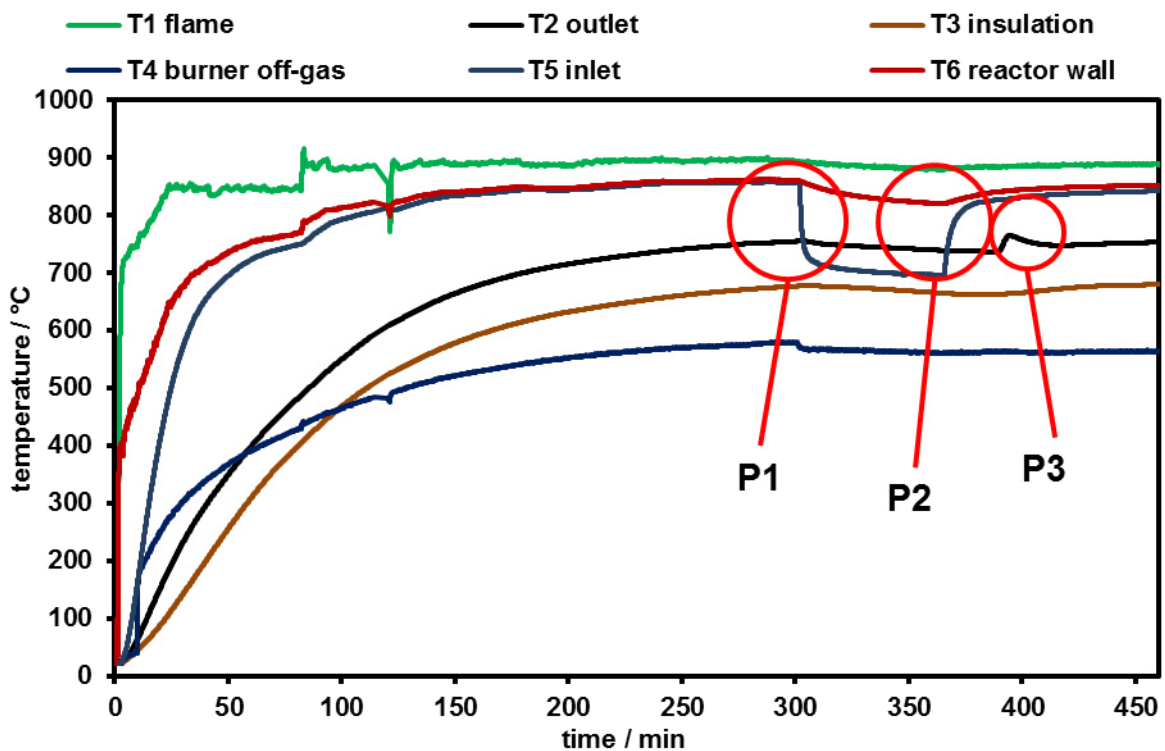


**Figure 49: Temperature profile of the complete cycle 4; highlighted points are: P1-start of the reforming reaction, P2-end of the reforming reaction and P3-start of the oxidation reaction.**

Again no stable plateau was visible during the reduction reaction but hydrogen and carbon monoxide amount increased continuously while the carbon dioxide amount decreased due to the ongoing reduction reaction. A total amount of 23205.8 ml hydrogen (99.84% purity) was produced and a maximum hydrogen flow of 841.3 ml·min$^{-1}$ (0.150 kW) was achieved which equals a maximum steam conversion rates of 75%. As seen at cycle 2 no increased amount of impurities was detected during the biogas reforming experiments compared to the experiments conducted with pure methane.

**Figure 50: Dry gas composition during the fourth cycle measured with the micro GC; note that the time is not synchronised with Figure 49.**

**Cycle 5:**

The aim of the fifth cycle was the determination of the maximum methane conversion rate of the prototype reactor. Therefore, the methane flow was changed four times during the reduction step. In addition a system for automated temperature control was installed on order to enable automated heating of the prototype. Figure 51 shows the temperature profile was well as the methane flow of the gas burner during the fifth cycle. The temperature control was achieved through the coupling of a thermocouple (T1) with the MFC for fuel gas. The temperature profile is comparable to the previous cycles. The temperature drops (T5) during the different reforming/reduction steps (P1and P2) as well as at the beginning of the oxidation step (T2, P3) are highlighted. A methane flow of 2650 ml·min$^{-1}$ was necessary to keep the temperatures at a feasible level.
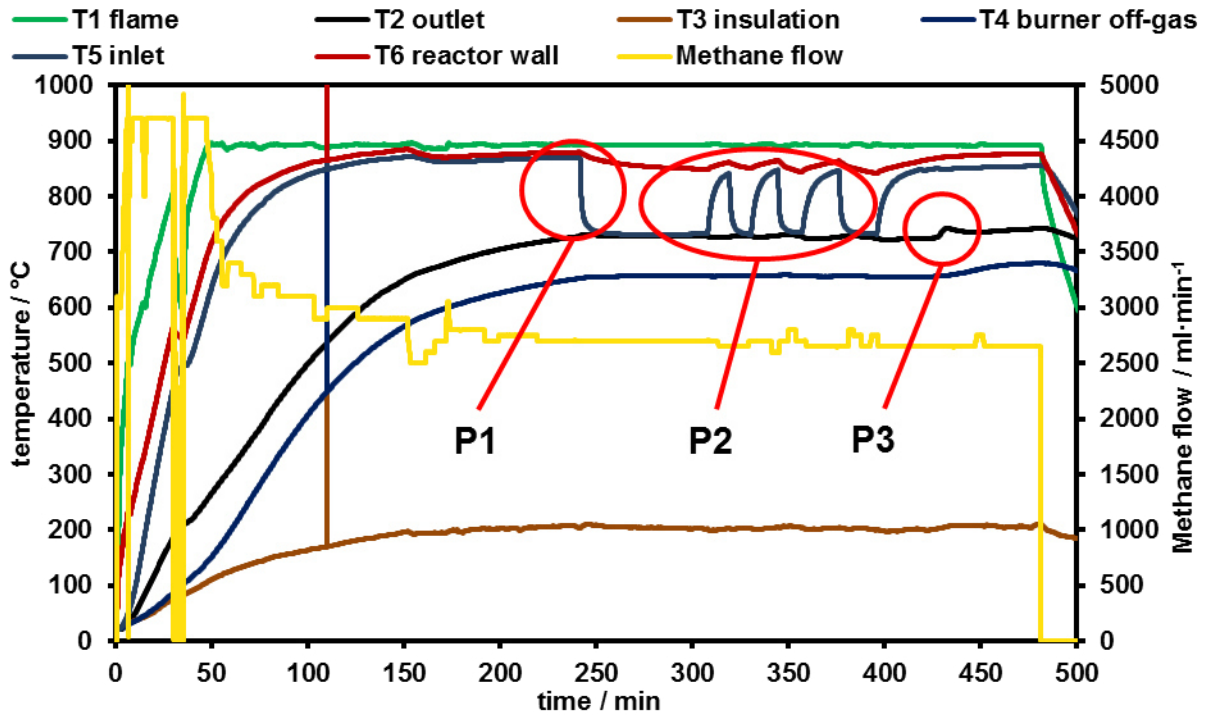
**Figure 51 Temperature profile of the complete cycle 5; highlighted points are: P1-start of the reforming reaction, P2-consecutive reforming/reduction phases and P3-start of the oxidation reaction.**

Table 15 shows the measured methane conversion rates versus the corresponding inlet flow rates. A conversion range is given for high flow rates of 1310 ml·min$^{-1}$ and 1030 ml·min$^{-1}$ because no stable value was measured. The conversion decreased during the measurement and this phenomenon might be related to the continuous reduction of iron oxides with unreacted methane according to Eq. (10). The decreasing methane conversion rate is clearly visible in Figure 52 and Figure 53 during the third and fourth reforming/reduction step. This data shows that the maximum methane flow rate, at which almost complete methane conversion can be achieved at the given conditions, lies between 730 and 1030 ml·min$^{-1}$. It has to be clarified at this point that a high methane conversion does not imply a high efficiency or hydrogen yield since even at high methane conversion rates significant amounts of syngas can leave the reactor without reducing iron oxide.

**Table 15: Methane conversion versus SMR methane flow.**

| SMR methane flow / ml·min$^{-1}$ | Methane conversion / % |
|---|---|
| 530 | >99% |
| 730 | >99% |
| 1310 | 85-90% |
| 1030 | 90-99% |

The oxidation was performed at an initial water flow rate of 2.27 g·min$^{-1}$ which increased during the reaction to an averaged value of 2.6 g·min$^{-1}$. The formation of 32956.7 ml hydrogen (100% purity) was measured by the micro GC, 33976.5 ml hydrogen (99.94% purity) were measured by the gas analyser. The maximum hydrogen flow measured by the micro GC was 1566.7 ml·min$^{-1}$ (0.280 kW), and 1633.1 ml·min$^{-1}$ (0.292 kW) measured by the gas analyser. These values equal maximum steam conversion rates of 56% and 58% respectively.
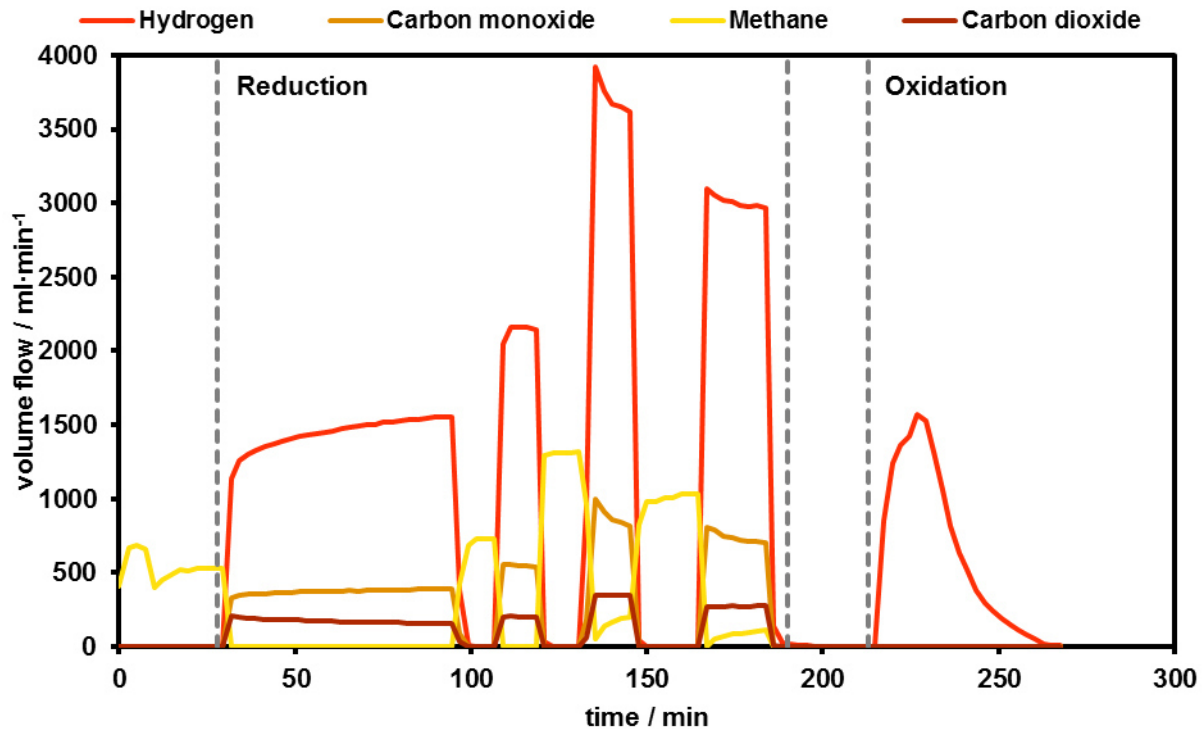


**Figure 52: Dry gas composition during the fifth cycle measured with the micro GC; note that the time is not synchronised with Figure 51 and Figure 53.**

Figure 54 shows the amounts of impurities produced during the oxidation reaction. As already shown at the third cycle (Figure 48) carbon dioxide, carbon monoxide and methane were present. At this experiment also the detector for carbon monoxide was calibrated for concentrations in the ppm range and, therefore, only the methane signal showed strong random noises. The experiment clearly showed that carbon monoxide has the smallest share of all species present. A significant amount of methane was also quantified at this oxidation experiment. The shape of the methane signal in Figure 54 gives hint to the assumption that methane is produced during the oxidation and is not only a relic of the prior reforming reaction but further improvements in the analytics would be necessary to get reliable data and to prove the occurrence of methanation.

**Figure 53: Dry gas composition during the fifth cycle measured with the gas analyser; note that the time is not synchronised with Figure 51 and Figure 52.**



**Figure 54: Impurities during the oxidation phase of cycle 5; the black line represents averaged values in order to in increase the signal to noise ratio (left), total amount of impurities (right).**

Table 16 summarises the results of the 5 prototype cycles. The highest conversion of syngas as well as the lowest rate for hydrogen recovery (Eq. (27)) was achieved at the first cycle and is explained by the fact that the cycle started from the haematite level while at the other cycles magnetite was the highest oxidised species.

$$\text{Hydrogen recovery/\%} = 100*H_{2,\,produced}/SEQ_{converted} \qquad (27)$$

**Table 16: Summary of the 5 prototype cycles, note that cycle 1 started from $Fe_2O_3$.**

| Gas analysis | Cycle 1 | Cycle 2 | Cycle 3 | | Cycle 4 | Cycle 5 | |
|---|---|---|---|---|---|---|---|
| | Micro GC | Micro GC | Micro GC | Gas analyser | Micro GC | Micro GC | Gas analyser |
| SEQ-Con. / ml | 26812.7 | 14519.6 | 37626.7 | 35102.0 | 18796.4 | 36721.6 | 23830.7 |
| SEQ-Con. / % | 26.2 | 23.1 | 8.6 | 8.1 | 13.1 | 11.0 | 7.6 |
| $H_2$-prod. / ml | 18689.9 | 17960.2 | 39804.6 | 40387.0 | 23205.8 | 32956.7 | 33976.5 |
| OC-Red. / % | 26.6 | 16.2 | 41.9 | 39.1 | 20.9 | 40.9 | 26.5 |
| OC-Ox. / % | 20.8 | 20.0 | 44.3 | 45.0 | 25.9 | 36.7 | 37.8 |
| $H_2$-Rec. / % | 69.7 | 123.7 | 105.8 | 115.1 | 123.5 | 89.7 | 142.6 |
| $H_2$-Yield* / % | 18.2 | 28.5 | 9.1 | 9.3 | 16.2 | 9.9 | 10.9 |
| $H_2$-Purity / % | 99.89 | 99.79 | 99.55 | 99.94 | 99.84 | 100.00 | 99.94 |
| *excl. combustion | | | | | | | |

In all cases except cycle 1 and cycle 5 the measured amount of produced hydrogen was higher than the amount of consumed syngas. This cannot be explained for sure but might be related to an error in the gas analysis. At cycle 3 and 5 a micro GC and a gas analyser were used in order crosscheck the results. The measured difference between consumed syngas and produced hydrogen was bigger for the gas analyser than for the micro GC. The amount of produced hydrogen was almost the same for both detection systems. This gives hint to the assumption that the hydrogen quantification is reliable while the quantification of syngas is inaccurate at both systems but to a higher extent at the gas analyser. Even if the mass balance cannot be closed due to the inaccurate gas analysis, the general findings of the experiments are reliable and valid. The overall purity of the produced hydrogen is always above 99% and errors in gas quantification do not have a significant influence on these values. No significant difference in terms of hydrogen purity was found between the conversion of pure methane and mixtures of methane and carbon dioxide. This makes the process interesting for the decentralised conversion of biogas for fuel cell applications and as an alternative for conventional biogas utilisation. On the other hand, although the high purity of the produced hydrogen is very promising, the measured amount of 15 respectively 24 ppm of carbon monoxide is still too high for state of the art low temperature fuel cells. Cheng et al.

reviewed articles to investigate the negative effect of carbon monoxide on PEM-FCs at concentrations between 0 and 250 ppm and found a decrease in efficiency already at 25 ppm [111]. Bender et al. measured negative effects of carbon monoxide on PEM-FCs even at a concentration of 1 ppm [112]. Jean St-Pierre developed a contamination model and calculated a steady state performance loss of less than 1% at 0.2 - 0.9 ppm [113]. Although catalysts with higher tolerance towards carbon monoxide are under development attempts should be undertaken to increase the purity of the produced hydrogen [114,115].

Only 20% - 45% of the oxygen carrier was reduced respectively oxidised during the prototype cycles. This indicates that some parts of the oxygen carrier particles were reacting very slow with the syngas or were completely inaccessible for the reducing gases. Sintering of the oxygen carrier is a well-known phenomenon and can be the main reason for the low oxygen carrier conversion but the intensity of inactivation was unexpected. Regarding the hydrogen yield of the system it has to be said that the overall syngas conversion was rather low, between 7.6% and 26.2%, which means that a significant share of chemical energy is lost during the reduction step and, therefore, hydrogen yield and efficiency are low. Irrespective of whether a thermodynamic or kinetic limitation leads to the low syngas conversion, improvements are necessary to increase the efficiency of the system. High amounts of methane were burned in order to reach the high reaction temperatures needed for the process. At the fifth cycle almost complete methane conversion in the reactor was reached at a flow rate of 730 ml·min$^{-1}$ but 2650 ml·min$^{-1}$ of methane were used to keep the temperature above 700 °C. Therefore, at the given system configuration even if 100% of the unreacted syngas would be combusted in order to decrease the gas demand of the burner the overall efficiency of the prototype would still be very low. Based on the findings of these experiments a simulation of the prototype was carried out in order to investigate the effects of syngas recirculation and heat integration on the overall efficiency of the system.

## 5.4. Prototype simulation and improvement

During the experiments three points were identified as major issues for system improvement:

- Minimisation of methane demand for heat generation
- Utilisation of unreacted syngas to increase hydrogen yield and efficiency
- Decreasing the carbon monoxide content of the produced hydrogen

### 5.4.1. Model description

The simulation was carried out using the commercial software ASPEN PlusTM – V8.4 (Aspen Technology, Inc.). As for the simulations presented in section 3 the Standard Peng-

Robinson equation of state was used. Figure 55 shows the flowsheet of the whole process. Experimental data from cycle 3 of the previous chapter was used for the simulation (Table 17).

**Table 17: Experimental data of cycle three used for the calculations.**

| Parameter | Value |
|---|---|
| Methane flow for combustion | 2.65 l·min$^{-1}$ |
| Methane flow for steam reforming | 0.46 l·min$^{-1}$ |
| $H_2O$ flow for steam reforming | 0.9 g·min$^{-1}$ |
| Temperature for reforming, reduction and oxidation | 730 °C |
| Ambient temperature | 25 °C |
| Steam conversion during the oxidation | 26% |

The RStoic reactor was used to simulate the combustion zone. The RGibbs block was used for the steam reforming reaction. Reduction and oxidation were calculated using FORTRAN statements and the ASPEN calculator block. Hydrogen and carbon monoxide conversion for the reduction were calculated from equilibrium data [40]. The $H_2O/(H_2+H_2O)$ ratio of 0.6 and the $CO_2/(CO+CO_2)$ ratio of 0.7 were assumed for the reduction of magnetite to wustite. Based on experimental data an average steam conversion of 26% was assumed for the oxidation reaction. Methane was not considered for the reduction since calculations showed almost complete methane conversion during the steam reforming step. Reaction energies were taken from HSC chemistry 5.11 (Outokumpu). The FORTRAN calculations of the simulation are listed in the appendix (section 9.4). Simple heat exchanger blocks were used to simulate the energy conversion for reduction and oxidation. The calculated equilibrium composition for the reforming reaction at the given conditions as well as the measured gas composition at the end of the experiment showed a hydrogen and carbon monoxide content only slightly higher than the equilibrium composition of the reduction of wustite to iron. Therefore, only the reaction magnetite ↔ wustite was considered although experimental data showed that at least a part of the oxygen carrier was fully reduced to iron. Energy for steam reforming, reduction and gas preheating to 900 °C was transferred via heat streams form the burner to the particular blocks of the process flowsheet. The amount of air (AIR-IN) was adjusted in order to achieve a temperature of 760 °C in the outlet stream of the burner block (BURNM1). This stream was used to evaporate water and to preheat methane and steam for the steam methane reforming reaction. A temperature difference of 10 °C between BURNM1 and the preheated steam/methane mixture (PREHEAT) was assumed. An additional heat exchanger (B1) was used to simulate the superheating of the mixture to a temperature of 900 °C prior to the reforming reaction. This additional heating step was implemented to the

simulation since at the real prototype gases are superheated before they enter the reaction zone of the reactor (see Figure 40 and Figure 45).

In addition, the feasibility of methanation for fine purification of the produced hydrogen was investigated. Therefore, a mixture based on the experimental results of cycle three was analysed via the RGibbs reactor block at temperatures of 150 - 500 °C and pressure levels between 1 and 50 bar(a) (Table 18). A wet gas stream as well as a water-free stream was investigated.

**Table 18: Gas compositions used for the simulation of the methanation reaction.**

| Component | wet gas / $mol \cdot s^{-1}$ | dry gas / $mol \cdot s^{-1}$ |
|:---:|:---:|:---:|
| $CH_4$ | 0.3463414 | 0.3463414 |
| $H_2$ | 100 | 100 |
| CO | 0.0195121 | 0.0195121 |
| $H_2O$ | 385 | 0 |
| $CO_2$ | 0.1341463 | 0.1341463 |

The Flex Fuel Reformer prototype
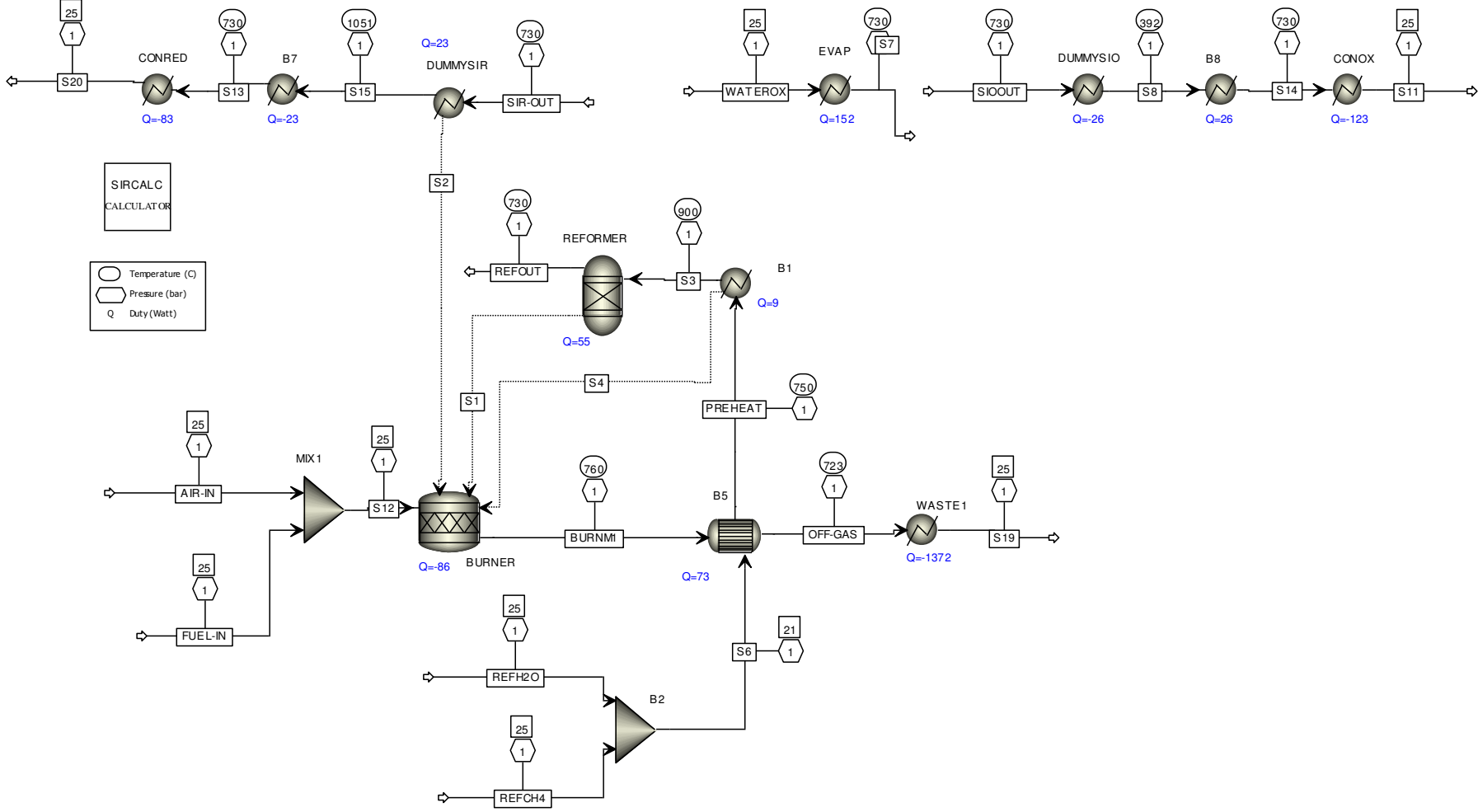


**Figure 55: Process flowsheet of the prototype.**

### 5.4.2. Results and discussion

Figure 56 shows $CH_4$-conversion and dry gas composition of cycle three as well as the consumed energy during the reduction. It is obvious that more than 50% of the process energy is required for gas heating and steam generation while only one third is used for the reforming reaction. The energy consumed for the reduction of iron equals only 14% of the process energy. The consumed power of the reducer was calculated with 22.7 J·s$^{-1}$ and the steam-oxidation led to a calculated power output of 26.2 J·s$^{-1}$. The difference of these values can be easily explained by the fact that the net reaction of reduction and oxidation is the water-gas shift reaction. Based on the calculated amount of converted carbon monoxide during the reduction and the power difference between reduction and oxidation the reaction energy of -34.83 kJ·mol$^{-1}_{CO}$ was calculated. This value is in agreement with HSC data for the water-gas shift reaction and indicates correct results of the calculations. Considering the oxidation reaction, the energy needed for steam generation alone is higher than for all other unit operations due to the low steam conversion rate. On the other hand, this amount of energy can be recirculated relatively easy because of the fact that the produced hydrogen has to be cooled and dried anyway. Therefore, a simple counter current heat exchanger can be used to recover most of the energy of this stream and to utilise it directly for steam generation.
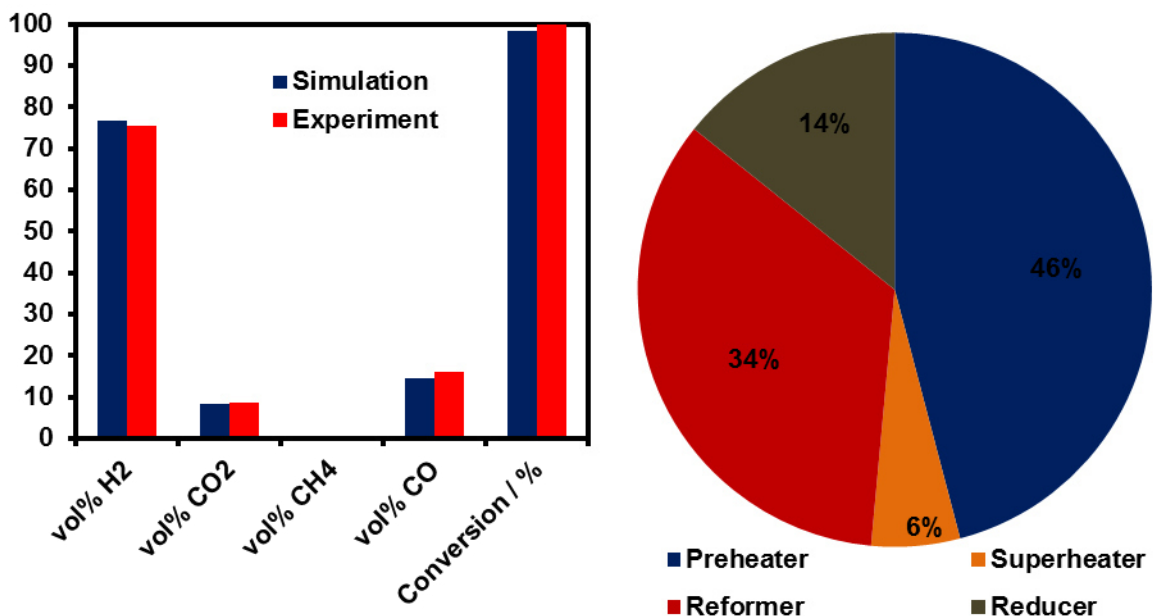


**Figure 56: CH$_4$-conversion and dry gas composition for steam reforming of methane (left), calculated energy consumption during the reduction (right).**

In general it has to be said that 87% of the heat delivered from the gas burner is lost with the off-gas stream (WASTE1) while non-existent heat recovery after reduction (CONRED) and after oxidation (CONOX) only contribute with 5% and 8% of total heat loss respectively. In

this simulation other thermal losses such as imperfect insulation of the system were also allocated to the off-gas stream so the calculated heat of this stream can never be fully utilised. Nevertheless, an efficient process can only be realised if the energy loss from the off-gas stream is decreased significantly.

Based on the simulation results a modified flowsheet of the process was developed (Figure 57). In this simulation the amount of oxygen for the combustion reaction was fixed to an air to fuel ratio of $\lambda=1.2$ in order to minimise the overall gas flow and the amount of energy needed for the heating of air. The temperature of the reformer inlet stream (PREHEAT) was set to 900°C and the burner outlet temperature (BURNM1) was set to 1000 ± 50 °C. To further optimise the system a heat integration of reduction and oxidation was done. Due to the low steam conversion rate a high amount of energy is necessary to produce steam for the oxidation reaction. On the other hand, the unreacted steam has to be removed from the product stream in order get pure hydrogen. Therefore, the utilisation of the energy gained from this process step is obvious. Additional energy gained from the outlet stream of the reduction step is sufficient to generate the needed steam and no additional fuel needs to be combusted. Therefore, an assembly of two reactors, one in reduction mode and the other in oxidation mode, is able to increase the efficiency of the process. The heat produced during the oxidation was not considered at these calculations since the utilisation of this energy is seen as complicated and inefficient for a real process. Based on these constraints and considerations the fuel flow of the process was minimised using the optimisation tool of ASPEN plus. The calculations revealed that only 269 ml·min$^{-1}$ of methane have to be combusted in order to deliver the necessary heat for the conversion of 460 ml·min$^{-1}$ methane with the reformer-steam iron process. This equals an amount of 37%. Only 71 W of waste-heat are produced at the optimised process, compared to 1578 W before heat integration and optimisation of the combustion. Nevertheless, the low amount of converted syngas during the reduction step, due to the thermodynamic limitations of the process, still limits the efficiency in terms of hydrogen production.

Based on the calculated hydrogen flow ($H_{2, out}$=739 ml·min$^{-1}$), the $CH_4$ demand ($fuel_{in}$) and the lower heating values ($LHV_{H2}$ and $LHV_{fuel}$), even after optimised heat integration, a hydrogen yield of only 25% and an overall efficiency of 31% are achieved (see equation (24) and (28)).

$$\text{Efficiency / \% } = 100*(H_{2, out} * LHV_{H2})/(fuel_{in} * LHV_{fuel}) \tag{28}$$

Although the high amounts of unreacted hydrogen and carbon monoxide can be combusted after the reduction step the overall efficiency is still low. Assuming a complete combustion of the unreacted syngas it is possible to avoid the need of additional methane for combustion and to achieve a hydrogen yield of 40% and an overall efficiency of 48%.

The Flex Fuel Reformer prototype
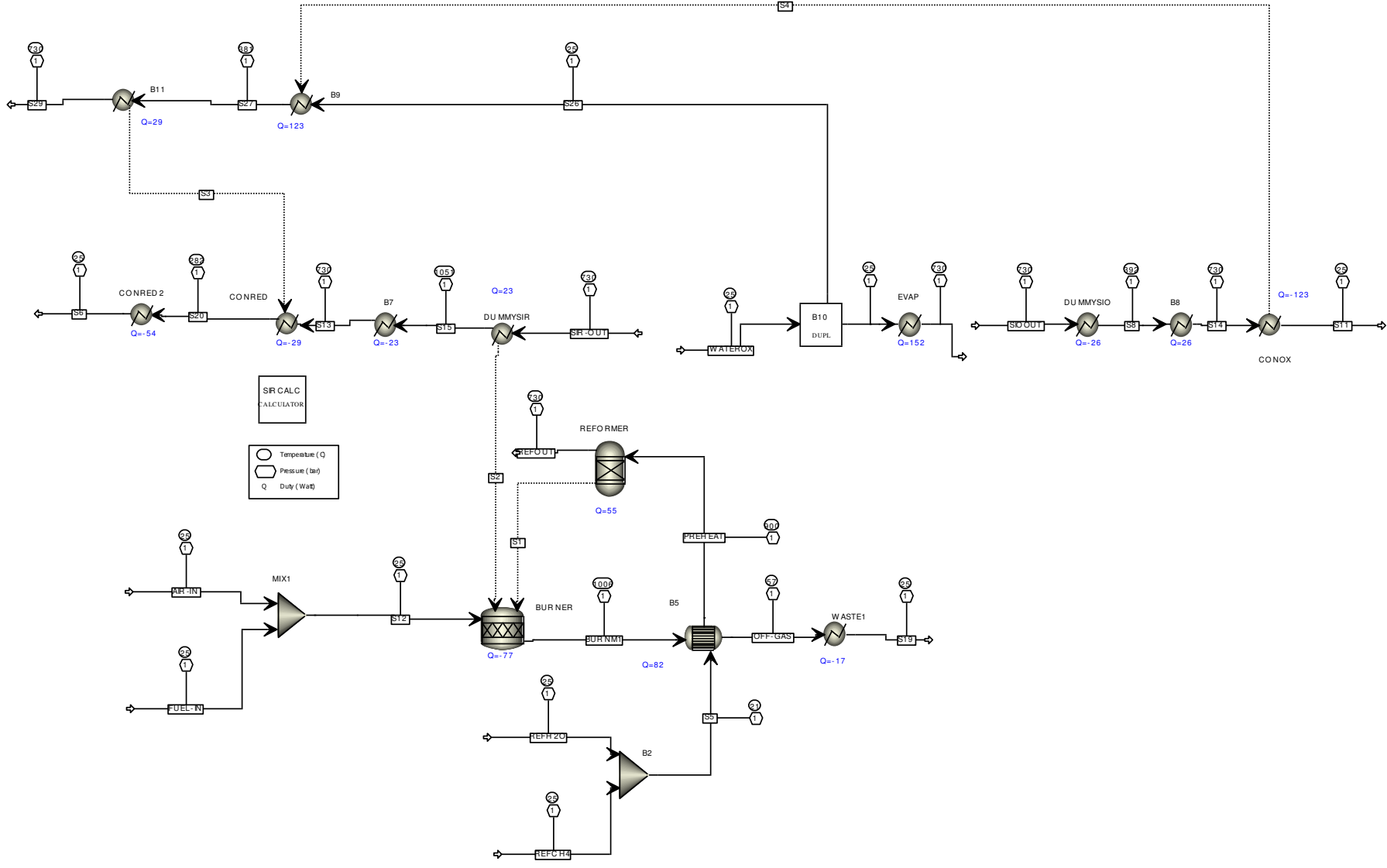


**Figure 57: Optimised process with heat integration.**

A further increase in efficiency is possible if the hydrogen and carbon monoxide content of the produced syngas are increased. Figure 58 shows the effect of increasing reformer temperature and decreasing steam to carbon ratio on the hydrogen and carbon monoxide content of the produced syngas. If the temperature is high enough, at a s/c-ratio of 1 almost 100% selectivity towards hydrogen and carbon monoxide are achieved. Using carbon dioxide instead of steam for the reforming reaction the same trend can be seen. At these optimised conditions the efficiency of the process is directly limited by the $H_2/H_2O$ and $CO/CO_2$ equilibria. Therefore, conversion efficiencies in the range of 70% - 90% can be achieved if only the reduction from magnetite to wustite is performed. At a reforming temperature of 900 °C and a s/c-ratio of 1.3 a syngas containing a $H_2/H_2O$ ratio of 11.5 and a $CO/CO_2$ ratio of 14.5 is achieved. Assuming an equilibrium concentration of 80% $H_2O$ and $CO_2$ after the reduction, a hydrogen yield of 41% and an efficiency of 49% can be achieved without combustion of the reformer off-gas. Including off-gas combustion a hydrogen yield of 58% and an efficiency of 69% can be achieved.
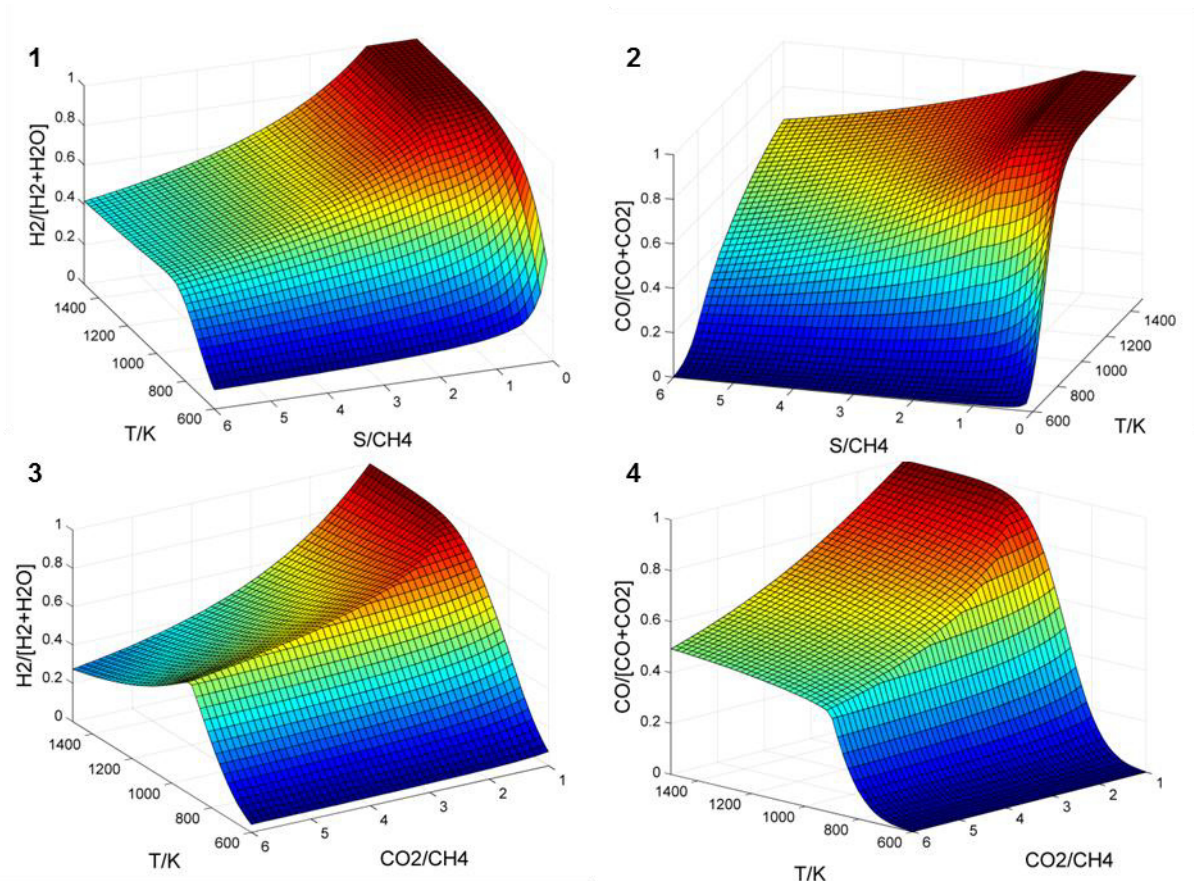


**Figure 58: Simulated ratios of $H_2/(H_2+H_2O)$ and $CO/(CO+CO_2)$ as function of temperature and steam to $CH_4$ ratio (1 & 2), and carbon dioxide to $CH_4$ ratio (3 & 4).**

These high efficiencies and hydrogen yields are only possible if the reduction is stopped before magnetite is fully converted to wuestite. For the complete reduction of the oxygen carrier to Fe the efficiency decreases significantly due to the unfavourable equilibria. To

achieve a high efficiency and a high hydrogen yield also during the reduction of wuestite to Fe strategies for the recycling of the reducer off-gas have been proposed [46][116].

In terms of hydrogen purity the measured data showed low but significant amounts of carbon monoxide in the produced hydrogen although thermodynamic calculations did not predict the formation of solid carbon at the chosen experimental conditions. This finding gives rise to the assumption that completely carbon free hydrogen might not be producible at feasible experimental conditions. If this is the case a purging step with hydrogen at low temperatures prior to the steam-oxidation might be an option in order to remove solid carbon from the oxygen carrier via the formation of methane following Eq. (16). An alternative approach to guarantee highest hydrogen purity is the implementation of an additional purification step after the steam-oxidation phase. Two different purification steps are possible:

- Selective oxidation of carbon monoxide using air (Eq. (29))
- Methanation of carbon monoxide and carbon dioxide with hydrogen (Eq. 20 and 30)

$$CO + 1/2 O_2 \rightarrow CO_2 \tag{29}$$

$$CO + 3H_2 \rightarrow CH_4 + H_2O \tag{30}$$
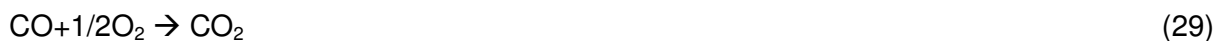
For selective oxidation air has to be injected into the system which further increases the complexity of the whole process and leads to additional nitrogen contamination. On the other hand, methanation can be conducted directly downstream the steam-oxidation reaction without the need of additional process compounds except a catalytically active species. Therefore, this process seems more favourable and a thermodynamic simulation of the process was carried out. Figure 59 shows the results of thermodynamic simulations of the methanisation reaction between 150 °C and 500 °C at different pressure levels. Under all investigated pressure conditions the simulations predict the possibility to decrease the carbon monoxide content to a level far below 1 ppm. Due to the exothermic nature of the methanation reaction the highest purity is achieved at the lowest temperature. Catalysts showing high activity in carbon monoxide conversion at low temperature are known [117]. Due to Le Chatelier's principle also higher pressure leads to a lower content of carbon monoxide and carbon dioxide. The presence of water in the gas stream shifts the $CO \leftrightarrow CO_2$ equilibria towards carbon dioxide but leads to a decreased carbon monoxide and carbon dioxide conversion at all temperature and pressure levels. It is highly beneficial for the reformer-steam iron process that the lowest amount of carbon monoxide is present at highest pressure and at dry conditions. As shown in section 2 of this thesis the process is suitable to produce pressurised hydrogen during the oxidation step. Therefore, the condensation of steam can be conducted at higher temperatures due to the increased boiling point of water at elevated pressure. At a pressure of 50 bar condensation of water is already possible at a

temperature of approximately 260 °C. This enables the drying of the gas stream after the oxidation at temperatures suitable for the methanation reaction. One can even think on reaction conditions that enable the permanent condensation of produced water during the methanation reaction which will lead to a further increase in CO and $CO_2$ conversion. A similar effect of the selective removal of a reaction product is well known for membrane assisted processes such as methane steam reforming using dense palladium-membrane reactors [33,34].
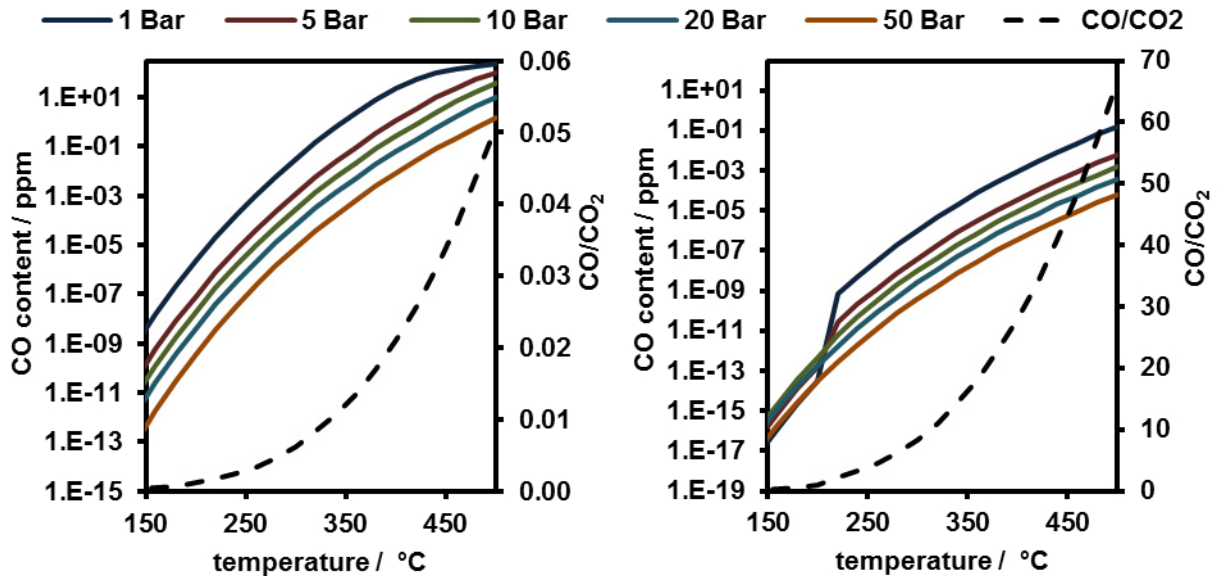


**Figure 59: Thermodynamic calculations of CO (ppm volume based) content and CO/CO$_2$ ratio of wet gas (left) and dry gas (right).**

## 5.5.    Summary and conclusion

The gained results show the fundamental proof of concept of the developed reactor concept and the designed prototype. Experiments using pure methane and mixtures of methane and carbon dioxide as model compound for biogas were carried out. All measurements confirmed the ability of the process for the production of pure hydrogen. Hydrogen purities between 99.8% and 100% were measured during all experiments. A detailed analysis of the produced hydrogen revealed that carbon monoxide was not the main impurity but carbon dioxide and methane. The experimental results and process simulations helped to determine design strategies to improve the efficiency of the system. The high amount of combusted methane to deliver the necessary heat was determined as the major problem in terms of efficiency and hydrogen yield. Calculations revealed that up to 87% of the heat delivered from the gas burner was wasted due to thermal losses. Therefore, an efficient heat recovery system and an improved thermal insulation are the primary issues that have to be implemented. The second obstacle is the low amount of converted syngas during the reduction step. Due to the

low temperature of 700 °C – 750 °C and high amounts of steam used for the reforming reaction only a small share of the syngas (7% - 26%) was converted during the reduction step of the process. Performing the reaction at higher temperature and with a lower steam to carbon ratio will increase the conversion efficiency of the reduction step but will also increase the thermal stress applied on the reactor and the oxygen carrier. In addition low amounts of steam also increase the risk of coke formation and lower hydrogen purity might be the result. An enhanced process design including the utilisation of burner off-gas for the preheating of air and fuel as well as thermal coupling of reduction and oxidation reaction was simulated at 900 °C. These heat integration steps as well as the combustion of unreacted syngas led to a calculated efficiency of 69% and a hydrogen yield of 58%. If the oxygen carrier gets completely reduced to Fe instead of FeO higher amounts of hydrogen and carbon monoxide remain in the off-gas stream due to unfavourable equilibrium concentrations. Therefore, more sophisticated concepts, such as the re-circulation of the off-gas during the reduction reaction, might be more efficient than the simple combustion of the off-gas. In this case efficiencies in the range of 74.25% – 79.53% vs. LHV were calculated by Fraser, Monsberger and Hacker for different hydrocarbon fuels [116]. These values are slightly higher than the 69% vs. LHV maximum efficiency, which were calculated in this chapter but their system was more complex and the implementation of off-gas re-circulation might be challenging. Thus, for a real system, designed for pressurised operation, the configuration which was developed in this thesis is advantageous. It combines simple and cost-efficient design with high efficiency and hydrogen purity.

Simulations to investigate the feasibility of the methanation reaction for increased purity showed that the carbon monoxide content can be reduced to the range of ppb if appropriate reaction conditions are chosen and catalytic activity is high enough. Especially the fact that pressurised hydrogen can be produced with the reformer-steam iron process turned out to have a major positive effect on the hydrogen purity when methanation is performed.

Several assumptions and simplifications were made to simulate the process. Nevertheless, the gained data helped to understand fundamental aspects of the process. It can be used for further improvements of the prototype such as the recirculation of unreacted syngas, the optimisation of operating conditions and the investigation of methanation for fine purification.

# 6. Conclusions and outlook

Hydrogen must be compressed or liquefied for efficient storage and distribution and these are themselves energy intensive processes. Pressurised hydrogen production via the conventional steam reforming process is challenging, especially for small decentralised hydrogen plants, since methane conversion is strongly influenced by the operational pressure of the reactor. The two-step steam iron process in combination with conventional steam reforming, offers a practical solution for the decentralised production of pure pressurised hydrogen. If the steam reforming reaction and the reduction of the oxygen carrier are performed at ambient pressure no gas compression step is needed and ideal reaction conditions are applied from a thermodynamic point perspective. At the oxidation step the system can be pressurised by the evaporation of water and the formation of gaseous hydrogen. After the condensation of unreacted steam pressurised hydrogen is produced. Stable hydrogen flow rates at 8 – 10 bar were achieved at lab-scale and are discussed in this thesis.

A detailed investigation of commercial nickel- and ruthenium based catalysts was carried out in order to obtain reliable data for steam reforming of methane and biogas with regard to the applicability for the steam iron process. At 750 °C a methane conversion rate of 93% - 95% was achieved with both systems. At this temperature no significant difference between steam reforming of pure methane or biogas was found in terms of $CH_4$-conversion but biogas reforming always led to lower $H_2$-yields because of the reversed water-gas shift reaction. Since carbon monoxide can also be used for the reduction of iron oxides this trend has no negative effect on the reformer-steam iron process.

High temperatures and low steam to carbon ratios shift the equilibria towards high $H_2/H_2O$ and $CO/CO_2$ ratios. These measures improve the efficiency of the reformer-steam iron process, but are limited by the risk of solid carbon formation on the oxygen carrier. In addition, high temperatures increase sintering effects of the oxygen carriers. Samples containing $Fe_2O_3$ and different amounts of $CeO_2$ were synthesised and characterised. The TGA experiments showed that the oxygen storage capacity only decreased between 0.1% and 0.5% per cycle. While the reaction rate of the 10 wt% $CeO_2$ oxygen carrier decreased during 7 cycles, a more stable rate was achieved with the 20 wt% $CeO_2$ sample and the 30 wt% $CeO_2$ sample showed the best performance and stable reaction rates. The reduction of the oxygen carriers led to the formation of iron and the $CO_2$ oxidation performed led to the formation of $CeFeO_3$. After a consecutive air-oxidation step $Fe_2O_3$ and $CeO_2$ were produced and no accumulation of $CeFeO_3$ was measured after repeated cycling. The synthesised material turned out to be active for the decomposition of methane. Large amounts of methane might thus cause the formation of solid carbon during the reduction step of the

reformer-steam iron process if it is not converted to syngas in a prior reforming step. The same behaviour is also expected for other systems such as $Fe_2O_3$-$Al_2O_3$ which was used for the evaluation of the reformer-steam iron reactor prototype developed.

This prototype showed the fundamental suitability of the reformer-steam iron process for the production of pure hydrogen. Pure methane and methane-$CO_2$ mixtures were used and hydrogen purities above 99.8% were demonstrated. This shows the potential for biogas based hydrogen production. Only low amounts of 15 – 24 ppm carbon monoxide were detected in the hydrogen produced. No significant trend was found concerning the use of methane or biogas in terms of hydrogen purity. An ASPEN Plus simulation of the process based on experimental data, revealed several aspects for system improvement. The amount of combusted methane to generate the necessary temperature for the process must be minimised by optimising the thermal insulation, by minimising the amount of air for combustion and by the combustion of unreacted syngas. In addition the combination of two or more reactors in one assembly can be used for further system efficiency improvements. If one reactor is operated in reduction mode and one in oxidation mode heat which will otherwise be lost can be utilised. Low s/c-ratios and high reaction temperatures are desirable operating parameters to reach high $H_2/H_2O$ and $CO/CO_2$ ratios.

When the oxygen carrier is reduced to FeO instead of Fe an efficiency of 69%, based on the lower heating values of methane and hydrogen, and a hydrogen yield of 58% was calculated. Thus, the maximum efficiency of the configuration used for the prototype is slightly below the calculated efficiency of a system including an off-gas re-circulation which was stated to be 74.25% - 79.53% vs. LHV. On the other hand the developed concept combines good efficiency and hydrogen yield with a very simple and compact design. Systems including off-gas re-circulation by contrast, are more complex and the combination with pressurised oxidation in particular might prove hard to realise in such a system.

A simulation of the methanation reaction to reduce the carbon monoxide content was carried out and revealed the potential of this process especially at elevated pressure. Since the boiling point of water increases with the pressure it is possible to operate the methanation process at a temperature high enough for sufficient catalyst activity, but still low enough for steam condensation. In addition, the rise in pressure leads to a higher methanation activity due to Le Chatelier's principle and increases the conversion of carbon monoxide and carbon dioxide. Under these conditions carbon monoxide concentrations below 1 ppb can be achieved. Further research should include the behaviour of the oxygen carrier at higher pressure levels in terms of stability and reactivity, the investigation of the coke formation mechanisms during the reduction process, the analysis of the degradation process as a function of time, temperature and pressure as well as kinetic studies in combination with

computational fluid dynamics simulation. An improved system based on experimental data and simulation results should be assembled. With a stabilised performance of the oxygen carrier at a hydrogen pressure level of 50 - 100 bar, and an optimised system design and operational strategy, the reformer-steam iron process represents an alternative to high pressure electrolysis or membrane based steam reforming. It combines a simple and compact design with high hydrogen purity while avoiding high cost materials.

# 7. Experimental setup and characterisation methods

## 7.1. The microactivity reference system

The microactivity reference (MA0645LAT PID Eng&Tech) is an automated system for the characterisation of gas-solid reactions. After several modifications it was used for the experimental evaluation of the reformer-steam iron process for pressurised hydrogen production (chapter 2) as well as for the characterisation of nickel and ruthenium based catalysts for steam methane reforming and biogas reforming (chapter 3). Gases are supplied via 6 thermal mass flow controllers (EL-FLOW, Bronkhorst High-Tech B.V). Two different systems were used for steam generation. A steam generator (ADrop) was used for steam supply at ambient pressure. To produce steam at elevated pressure for pressurised hydrogen production a HPLC-pump (307 Piston Pump, Gilson Inc.) was used. Liquid water was fed into the heated region of the microactivity reference and was evaporated. The system was developed for temperatures up to 700 °C and a maximum operation pressure of 100 bar. A hastelloy fixed bed reactor (di=9.1 mm do=14.3 mm) was used to perform reactions at high temperature and pressure conditions.

## 7.2. The RSA-test rig

With the microactivity reference system it was only possible to characterise several grams of solids. In order to perform reactions at a prototype-level a new test rig was built up (Figure 60). An aluminium profile system (45 mm × 45 mm, Bosch Rexroth) was used for the main elements (see Figure-A IV in the-appendix for detailed information).
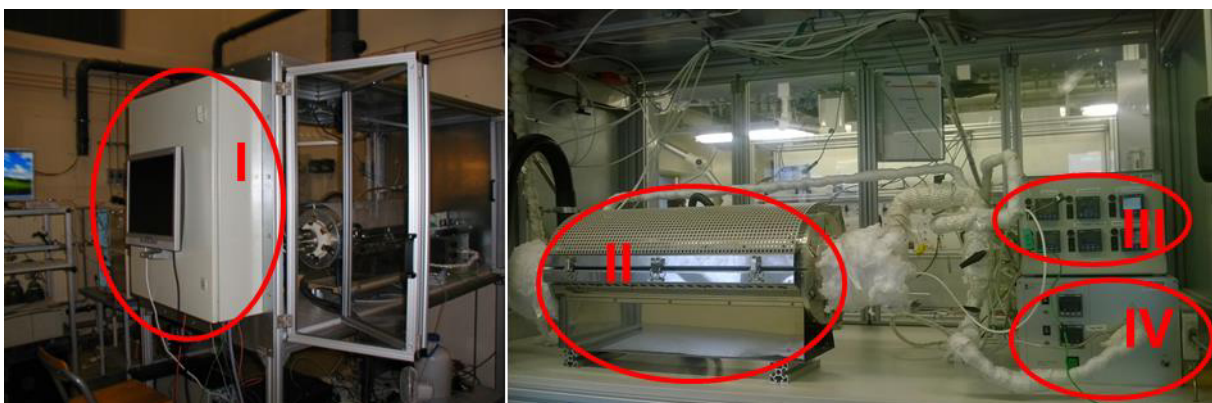


**Figure 60: The RSA-test rig including process control electronics (I), electric oven (II) PID controller for heating cords (III) and steam generator with liquid flow controller (IV).**

The test rig is divided into two sections. The upper section contains the electric oven with the stainless-steel fixed bed reactor system, the steam generator, heated pipes and the condenser for steam removal. This section can be sealed and is connected to the lab-

ventilation system which makes it possible to carry out experiments using large quantities of harmful and explosive gases such as carbon monoxide, methane or hydrogen. Non-critical components such as the water supply pump and thermal mass flow controllers are located in the lower section of the test rig. The electronics for process control are located at the front side of the test rig within an electrical enclosure. A detailed list of the used equipment is given in Table 19.

**Table 19: Main components of the RSA-test rig.**

| Component | Company | Specifications |
|---|---|---|
| Oven | Carbolite Gero GmbH & Co. KG | 12/02/3241 6 kW 1200 °C |
| Steam generator | aDROP Feuchtemeßtechnik GmbH | ATHMOS/T-1203-1 1 kg/h $H_2O$ |
| Water pump | GATHER Industrie GmbH | T1216691 |
| Variable-frequency drive for water pump | Peter electronics | FU-2/370W |
| Liquid flow controller | Bürkert | 1 kg/h $H_2O$ |
| Mass flow controllers | Bronkhorst High-Tech B.V Vögtlin Instruments AG | EL-FLOW red-y for gasflow |
| Condenser | SISON Ventile & Fittings Gmbh | own design |
| Heating cords | SAF Wärmetechnik GmbH | KM-HC-G |
| PID controller | Emko Elektronik A.S | ESM-4450 |
| Power supply module | National Instruments | FP-PS-4 |
| Programmable logic controller module | National Instruments | FP 2010 |
| Analog output module | National Instruments | FP-AO-200 |
| Solid state relay | Celduc relais | XKA20420 |
| Analog input module | National Instruments | FP-AI-100 |
| Thermo couple module | National Instruments | FP-TC-120 |

## 7.3.    Gas analysis

Two different systems were used for gas analysis. An Agilent 3000 micro gas chromatograph was used to quantify methane, carbon monoxide, hydrogen, nitrogen and carbon dioxide. While carbon dioxide was quantified using a PLOT U column (30.00μm/320.00μm/8m; fixed inlet) the other components were analysed via a molsieve column (12.00μm/320.00μm/10m; backflush inlet) equipped with a PLOT U pre-column (30.00μm/320μm/3m). The PLOT U column uses the polar divinylbenzene/ethyleneglycol-dimethacrylate system for the separation of $C_1$ to $C_7$ compounds, carbon dioxide and other species. The molsieve column

uses zeolites for the separation of gases. The main advantage of the micro GC system is the ability to analyse all important components online with only one system. In addition only several microliter of sample volume are needed. The two major drawbacks of the system are the long measurement period of 2 - 3 minutes as well as the high detection limits. For the reforming experiments (chapter 3) the long measurement period does not cause any problems since continuous reactions were investigated and no concentrations below 1% had to be quantified. For the investigation of the steam iron process, on the other hand, the long measurement period limits the feasibility of the system due to the limited time span of each cycle. Since the detection limit for carbon monoxide and carbon dioxide is in the range of 0.1% the micro GC cannot be used to evaluate the quality of the produced hydrogen in terms of usability for low temperature PEM-FCs. Therefore, a second gas analysis system (ABB-Uras 14 for the detection of $CH_4$, CO and $CO_2$ at ppm scale and ABB-Caldos 17 for the detection of vol% $H_2$) was used. The URAS 14 uses a nondispersive infrared detector, the Caldos 17 uses a thermal conductivity detector.

## 7.4.    Material characterisation

Different characterisation methods were applied to investigate the structural properties as well as the cyclic stability of the developed oxygen carriers.

### 7.4.1.  Measurement of surface area and pore size

The surface area of selected oxygen carriers was measured using the $N_2$-adsorption method. The so-called BET-method is named after Stephan Brunauer, Paul Hugh Emmett and Edward Teller who have published the basic concept of the method in 1938 [118]. The pore volume and area distribution of the samples can be measured using the $N_2$-desorption method published by, Elliott P. Barrett, Leslie G. Joyner and Paul P. Halenda (BJH-method) [119]. Although the BET theory is based on an over-simplified model of multilayer adsorption, the BET method continues to be used as a standard procedure for the determination of surface area [120]. At this method the monolayer capacity ($n_m$) is calculated via equation (31) where $n_a$ is the amount of adsorbed species at the relative pressure $p/p_0$ and C is a constant that is dependent on the isotherm shape. If the average area which is occupied by each adsorbed molecule in the monolayer is known ($a_m$) the surface are ($A_{BET}$) can be calculated form $n_m$ via equation 32 and the Avogadro constant (L= $6.02214*10^{23} \cdot mol^{-1}$) [121].

$$p/n_a(p_0-p) = 1/n_mC + (C-1)/n_mC * p/p_0 \qquad (31)$$

$$A_{BET} = n_m*L*a_m \qquad (32)$$

### 7.4.2. Thermogravimetric analysis

Thermogravimetric data was measured using two different thermo gravimetric analysers, a STA 449C Jupiter (Netzsch) coupled with a steam generator (aDrop-DV2MK, containing a Bronkhorst liquid flow controller) and a Mettler-Toledo thermogravimetric analyser coupled with a gas analyser for hydrogen detection (ABB-EL3020, nondispersive infrared detector). Both systems enable the determination of the mass change during reduction and oxidation and, therefore, give information about the reducibility of the investigated samples as well as of the speed of the different reaction steps. The STA 449C Jupiter was coupled with a steam generator and, therefore, it was possible to re-oxidise iron with steam. With the Mettler-Toledo thermogravimetric analyser this was not possible and, therefore, the oxidation reaction was performed with carbon dioxide. On the other hand, with the Mettler-Toledo thermogravimetric analyser it was possible to perform reduction experiments with hydrogen and methane and to re-oxidise the oxygen carrier with carbon dioxide and air. The combination with the gas analyser also enabled the determination of the hydrogen consumption during the TPR experiments.

### 7.4.3. X-ray diffraction

X-ray diffraction was used to get information about the crystal structure of the different oxidation stages of developed oxygen carriers (system: Bruker, AXS D8 Advance). At this non-destructive technique the diffraction of X-rays which is caused by the crystal structure of the sample is used to characterise the sample. Bragg´s law (Eq. (33)) states that a constructive interference of a diffracted X-ray of a given wavelength (λ) is only possible if AB+CD gives an integral multiple of λ (Eq. (34)). This relationship, which is illustrated in Figure 61 can be used to calculate the distance (d) between two planes of atoms by changing the angle (θ) and recording the corresponding diffraction pattern.

$$n\lambda = 2*d*\sin\theta \tag{33}$$

$$AB+CD = n*\lambda \tag{34}$$

Powder samples can be investigated using the powder diffraction method (Debye-Scherrer method). Ideally, in a powdered sample every possible crystalline orientation is represented equally and, therefore, Bragg´s law is always fulfilled for several lattice planes of a certain number of crystals. The comparison of the measured diffraction patterns with literature data enables the identification of the analysed specimen.
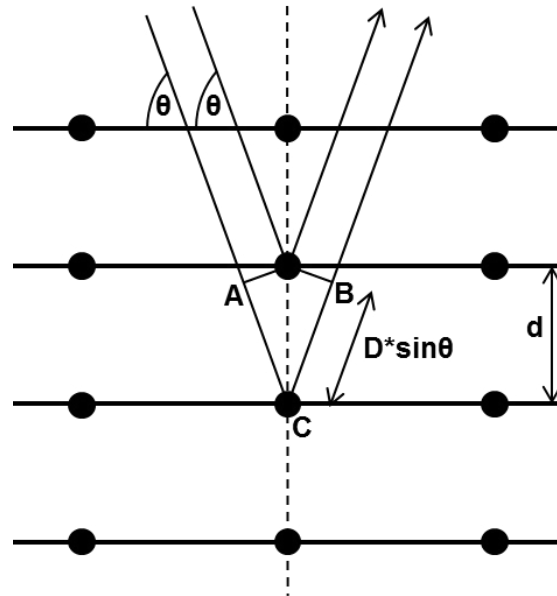
**Figure 61: Schematic illustration of X-ray diffraction at different atoms within a solid.**

### 7.4.4. Scanning electron microscopy and energy-dispersive X-ray spectroscopy

Scanning electron microscopy was used to investigate the structure of fresh and used oxygen carriers at a nanometer scale. SEM is a standard characterisation technique for various applications. Condenser lenses form an electron beam which is used to scan across the specimen. Different types of detectors are used to measure secondary electrons (SE) and backscattered electrons (BSE). Secondary electrons are electrons in the specimen that are ejected by the beam electron. They can only escape from the surface of the specimen and give no information about the elemental compositions of the sample. Backscattered electrons show strong dependence of the atom number. Heavy atoms appear darker compared to lighter atoms and, therefore, the detection of backscattered electrons opens up the possibility to identify different species in the sample. To get more information about the chemical composition of the sample SEM can be coupled with energy-dispersive X-ray spectroscopy (EDX). At this method the electron beam is used to remove an inner shell specimen electron to create an electron hole. In a secondary event an outer shell electron fills up the empty inner state and releases its excess energy as an X-ray emission. Since the energy of the X-ray emission is characteristic for the atomic structure and the energy between the two shells of the emitting element it can be used to identify the elemental composition of the scanned region.

### 7.4.5. Gas flow calculations

If not stated explicitly volumes are defined as standard volumes at 0 °C and at 101.325 kPa which means that 1 mole of gas or steam corresponds to 22.4 litres. If mass flows, molar flows or volume flows are explicated as a power output (e.g ml·min$^{-1}$ $H_2$ is written as kW $H_2$) the conversion is based on the lower heating value (LHV) of the substance.

LHVs and HHVs from HSC 5.11

$LHV_{H2}$        241.826 kJ·mol$^{-1}$

$LHV_{CH4}$        802.557 kJ·mol$^{-1}$

# 8. References

[1]     Nestl S, Voitic G, Lammer M, Marius B, Wagner J, Hacker V. **The production of pure pressurised hydrogen by the reformer-steam iron process in a fixed bed reactor system**. *J Power Sources* 2015;280:57–65. doi:10.1016/j.jpowsour.2015.01.052.

[2]     **2014 Key World Energy Statistics**. International Energy Agency: 2014.

[3]     **BP Statistical Review of World Energy June 2014**. 2014.

[4]     **American Chemical Society to Honor Keeling Curve in June 12 Ceremony** n.d. https://scripps.ucsd.edu/programs/keelingcurve/2015/06/02/american-chemical-society-to-recognize-keeling-curve/#more-1297 (accessed July 1, 2015).

[5]     Keeling CD, Piper SC, Whorf TP, Keeling RF. **Evolution of natural and anthropogenic fluxes of atmospheric CO2 from 1957 to 2003**. *Tellus, Ser B Chem Phys Meteorol* 2011;63:1–22. doi:10.1111/j.1600-0889.2010.00507.x.

[6]     **The Keeling Curve**. *Carbon Dioxide Conc Mauna Loa Obs* 2015. https://scripps.ucsd.edu/programs/keelingcurve/ (accessed June 28, 2015).

[7]     Hansen J, Ruedy R, Sato M, Lo K. **Global surface temperature change**. *Rev Geophys* 2010;48:RG4004. doi:10.1029/2010RG000345.

[8]     Smil V. **The Earth's Biosphere: Evolution, Dynamics, and Change**. Massachusetts: MIT Press; 2003.

[9]     Held IM, Soden BJ. **Water Vapor Feedback and Global Warming**. *Annu Rev Energy Environ* 2000;25:441–75.

[10]    Fourier JBJ. **Memoire sur les temperatures du globe terrestre et des espaces planetaires-Mémoires de l Academie des sciences de l institue de france** 1827:569–604.

[11]    Tyndall J. **Heat considered as a mode of motion**. New York: D. Appleton and company; 1873.

[12]    **Energy and Climate Change-World Energy Outlook Special Report**. Paris: 2015.

[13]    Stocker TF, Quin D, Plattner G-K, Tignor M, Allen SK, Boschung J, et al., editors. **IPCC, 2013: Summary for Policymakers**. Clim. Chang. 2013 Phys. Sci. Basis. Contrib. Work. Gr. I to Fifth Assess. Rep. Intergov. Panel Clim. Chang., Cambridge, United Kingdom and New York, NY, USA: Cambridge University Press; 2013.

[14]    Alley RB, Berntsen T, Bindoff NL, Chen Z, Chidthaisong A, Friedlingstein P, et al. **IPCC, 2007: Summary for Policymakers**. In: Solomon S, Qin D, Manning M, Chen Z, Marquis M, Averyt KB, et al., editors. Clim. Chang. 2007 Phys. Sci. Basis. Contrib. Work. Gr. I to Fourth Assess. Rep. Intergov. Panel Clim. Chang., Cambridge and New York: Cambridge University Press; 2007. doi:10.1038/446727a.

[15]    **Turn Down the Heat-Confronting the New Climate Normal**. Washington DC: 2014.

[16]    Dincer I. **Renewable energy and sustainable development: a crucial review**. *Renew Sustain Energy Rev* 2000;4:157–75. doi:10.1016/S1364-0321(99)00011-8.

[17]    Jacobson MZ. **Review of solutions to global warming, air pollution, and energy security**. *Energy Environ Sci* 2009;2:148. doi:10.1039/b809990c.

[18]    Lund H. **Renewable energy strategies for sustainable development**. *Energy* 2007;32:912–9. doi:10.1016/j.energy.2006.10.017.

[19]    Panwar NL, Kaushik SC, Kothari S. **Role of renewable energy sources in environmental protection: A review**. *Renew Sustain Energy Rev* 2011;15:1513–24. doi:10.1016/j.rser.2010.11.037.

[20]    **Global wind report-Annual market update 2014**. Brussels: 2014.

[21]    **Global Market outlook for photovoltaics 2014-2018**. Brussels: 2014.

[22]    **The state of the biofuels market: Regulatory, trade and development perspectives**. 2014.

[23]    **Renewable Energy Medium Term Market Report 2013**. Paris: 2013.

[24]    Schultz MG, Diehl T, Brasseur GP, Zittel W. **Air pollution and climate-forcing impacts of a global hydrogen economy**. *Science* 2003;302:624–7. doi:10.1126/science.1089527.

[25]    Kleijn R, Van Der Voet E. **Resource constraints in a hydrogen economy based on renewable energy sources: An exploration**. *Renew Sustain Energy Rev* 2010;14:2784–95. doi:10.1016/j.rser.2010.07.066.

[26]    Bartels JR, Pate MB, Olson NK. **An economic survey of hydrogen production from conventional and alternative energy sources**. *Int J Hydrogen Energy* 2010;35:8371–84. doi:10.1016/j.ijhydene.2010.04.035.

[27]    Andrews J, Shabani B. **Re-envisioning the role of hydrogen in a sustainable energy economy**. *Int J Hydrogen Energy* 2012;37:1184–203. doi:10.1016/j.ijhydene.2011.09.137.

[28]    Mazloomi K, Gomes C. **Hydrogen as an energy carrier: Prospects and challenges**. *Renew Sustain Energy Rev* 2012;16:3024–33. doi:10.1016/j.rser.2012.02.028.

[29]    Agnolucci P, Akgul O, McDowall W, Papageorgiou LG. **The importance of economies of scale, transport costs and demand patterns in optimising hydrogen fuelling infrastructure: An exploration with SHIPMod (Spatial hydrogen infrastructure planning model)**. *Int J Hydrogen Energy* 2013;38:11189–201. doi:10.1016/j.ijhydene.2013.06.071.

[30]    Lammer M. **Investigations on Generation of Ultra-Pure Hydrogen by the Steam-Iron Process Using a Tubular Reactor System**. Graz University of Technology; 2014.

[31]    Marius B. **Investigation and Characterization of Contact Mass Stability in the reversible Steam-Iron Process for Hydrogen Production , -storage and – purification**. Graz University of Technology; n.d.

[32]    Armaroli N, Balzani V. **The Hydrogen Issue**. *ChemSusChem* 2011;4:21–36. doi:10.1002/cssc.201000182.

[33]    Basile A, Campanari S, Manzolini G, Iulianelli A, Longo T, Liguori S, et al. **Methane steam reforming in a Pd–Ag membrane reformer: An experimental study on reaction pressure influence at middle temperature**. *Int J Hydrogen Energy* 2011;36:1531–9. doi:10.1016/j.ijhydene.2010.10.101.

[34]    De Falco M, Piemonte V, Di Paola L, Basile A. **Methane membrane steam reforming: Heat duty assessment**. *Int J Hydrogen Energy* 2014;39:4761–70. doi:10.1016/j.ijhydene.2013.09.066.

[35]    Rydén M, Lyngfelt A. **Using steam reforming to produce hydrogen with carbon dioxide capture by chemical-looping combustion**. *Int J Hydrogen Energy* 2006;31:1271–83. doi:10.1016/j.ijhydene.2005.12.003.

[36]    Fan L. **Chemical Looping Systems for Fossil Energy Conversion**. New Jersey: John Wiley and Sons; 2010.

[37]    Adanez J, Abad A, Garcia-Labiano F, Gayan P, de Diego LF. **Progress in Chemical-Looping Combustion and Reforming technologies**. *Prog Energy Combust Sci* 2012;38:215–82. doi:10.1016/j.pecs.2011.09.001.

[38]    Fan L-S, Zeng L, Wang W, Luo S. **Chemical looping processes for CO2 capture and carbonaceous fuel conversion – prospect and opportunity**. *Energy Environ Sci* 2012;5:7254–80. doi:10.1039/c2ee03198a.

[39]    Penthor S, Mayer K, Kern S, Kitzler H, Wöss D, Pröll T, et al. **Chemical-looping combustion of raw syngas from biomass steam gasification – Coupled operation of two dual fluidized bed pilot plants**. *Fuel* 2014;127:178–85. doi:10.1016/j.fuel.2014.01.062.

[40]    Hacker V, Faleschini G, Fuchs H, Fankhauser R, Simader G, Ghaemi M, et al. **Usage of biomass gas for fuel cells by the SIR process**. *J Power Sources* 1998;71:226–30. doi:10.1016/S0378-7753(97)02718-3.

[41]    Müller CR, Bohn CD, Song Q, Scott SA, Dennis JS. **The production of separate streams of pure hydrogen and carbon dioxide from coal via an iron-oxide redox cycle**. *Chem Eng J* 2011;166:1052–60. doi:10.1016/j.cej.2010.11.067.

[42]    Lorente E, Peña JA, Herguido J. **Cycle behaviour of iron ores in the steam-iron process**. *Int J Hydrogen Energy* 2011;36:7043–50. doi:10.1016/j.ijhydene.2011.03.069.

[43]    Rydén M, Arjmand M. **Continuous hydrogen production via the steam–iron reaction by chemical looping in a circulating fluidized-bed reactor**. *Int J Hydrogen Energy* 2012;37:4843–54. doi:10.1016/j.ijhydene.2011.12.037.

[44]    Aston VJ, Evanko BW, Weimer AW. **Investigation of novel mixed metal ferrites for pure H2 and CO2 production using chemical looping**. *Int J Hydrogen Energy* 2013;38:9085–96. doi:10.1016/j.ijhydene.2013.05.078.

[45]    Hacker V, Fankhauser R, Faleschini G, Fuchs H, Friedrich K, Muhr M, et al. **Hydrogen production by steam–iron process**. *J Power Sources* 2000;86:531–5. doi:10.1016/S0378-7753(99)00458-9.

[46] Hacker V. **A novel process for stationary hydrogen production: the reformer sponge iron cycle (RESC)**. *J Power Sources* 2003;118:311–4. doi:10.1016/S0378-7753(03)00076-4.

[47] Messerschmitt A. **Verfahren zur Erzeugung von Wasserstoff durch abwechselnde Oxydation und Reduktion von Eisen in von außen beheizten, in den Heizräumen angeordneten Zersetzern**. Germany: 1911.

[48] Thaler M, Hacker V. **Storage and separation of hydrogen with the metal steam process**. *Int J Hydrogen Energy* 2012;37:2800–6. doi:10.1016/j.ijhydene.2011.06.119.

[49] Nestl S, Voitic G, Geymayer M, Hacker V. **Component Development for the Reformer Steam Iron Process for Decentralised Sustainable Hydrogen Production**. *2013 AIChE Annu Meet* 2013.

[50] Otsuka K, Kaburagi T, Yamada C, Takenaka S. **Chemical storage of hydrogen by modified iron oxides**. *J Power Sources* 2003;122:111–21. doi:10.1016/S0378-7753(03)00398-7.

[51] Lorente E, Peña JA, Herguido J. **Separation and storage of hydrogen by steam-iron process: Effect of added metals upon hydrogen release and solid stability**. *J Power Sources* 2009;192:224–9. doi:10.1016/j.jpowsour.2008.12.116.

[52] Durbin DJ, Malardier-Jugroot C. **Review of hydrogen storage techniques for on board vehicle applications**. *Int J Hydrogen Energy* 2013;38:14595–617. doi:10.1016/j.ijhydene.2013.07.058.

[53] Ahluwalia RK, Hua TQ, Peng J-K. **Fuel cycle efficiencies of different automotive on-board hydrogen storage options**. *Int J Hydrogen Energy* 2007;32:3592–602. doi:10.1016/j.ijhydene.2007.03.021.

[54] Papadias DD, Lee SHD, Ferrandon M, Ahmed S. **An analytical and experimental investigation of high-pressure catalytic steam reforming of ethanol in a hydrogen selective membrane reactor**. *Int J Hydrogen Energy* 2010;35:2004–17. doi:10.1016/j.ijhydene.2009.12.042.

[55] Rabenstein G, Hacker V. **Hydrogen for fuel cells from ethanol by steam-reforming, partial-oxidation and combined auto-thermal reforming: A thermodynamic analysis**. *J Power Sources* 2008;185:1293–304. doi:10.1016/j.jpowsour.2008.08.010.

[56] Galvagno A, Chiodo V, Urbani F, Freni F. **Biogas as hydrogen source for fuel cell applications**. *Int J Hydrogen Energy* 2013;38:3913–20. doi:10.1016/j.ijhydene.2013.01.083.

[57] Xiao R, Song Q, Song M, Lu Z, Zhang S, Shen L. **Pressurized chemical-looping combustion of coal with an iron ore-based oxygen carrier**. *Combust Flame* 2010;157:1140–53. doi:10.1016/j.combustflame.2010.01.007.

[58] Garcia-Labiano F, Adanez J, de Diego LF, Gayán P, Abad A. **Effect of Pressure on the Behavior of Copper- , Iron- , and Nickel-Based Oxygen Carriers for Chemical-Looping Combustion**. *Energy & Fuels* 2006;20:26–33.

[59] Siriwardane R, Poston J, Chaudhari K, Zinn A, Simonyi T, Robinson C. **Chemical-Looping Combustion of Simulated Synthesis Gas Using Nickel Oxide Oxygen Carrier Supported on Bentonite**. *Energy & Fuels* 2007;21:1582–91.

[60] Tong A, Sridhar D, Sun Z, Kim HR, Zeng L, Wang F, et al. **Continuous high purity hydrogen generation from a syngas chemical looping 25kWth sub-pilot unit with 100% carbon capture**. *Fuel* 2013;103:495–505. doi:10.1016/j.fuel.2012.06.088.

[61] Tong A, Bayham S, Kathe M V., Zeng L, Luo S, Fan L-S. **Iron-based syngas chemical looping process and coal-direct chemical looping process development at Ohio State University**. *Appl Energy* 2014;113:1836–45. doi:10.1016/j.apenergy.2013.05.024.

[62] Abbas HF, Wan Daud WMA. **Hydrogen production by methane decomposition: A review**. *Int J Hydrogen Energy* 2010;35:1160–90. doi:10.1016/j.ijhydene.2009.11.036.

[63] Jin L, Si H, Zhang J, Lin P, Hu Z, Qiu B, et al. **Preparation of activated carbon supported Fe–Al2O3 catalyst and its application for hydrogen production by catalytic methane decomposition**. *Int J Hydrogen Energy* 2013;38:10373–80. doi:10.1016/j.ijhydene.2013.06.023.

[64] Tang L, Yamaguchi D, Burke N, Trimm D, Chiang K. **Methane decomposition over ceria modified iron catalysts**. *Catal Commun* 2010;11:1215–9. doi:10.1016/j.catcom.2010.07.004.

[65] Li Y, Li D, Wang G. **Methane decomposition to COx-free hydrogen and nano-carbon material on group 8–10 base metal catalysts: A review**. *Catal Today* 2011;162:1–48. doi:10.1016/j.cattod.2010.12.042.

[66] Ibeh B, Gardner C, Ternan M. **Separation of hydrogen from a hydrogen/methane mixture using a PEM fuel cell**. *Int J Hydrogen Energy* 2007;32:908–14. doi:10.1016/j.ijhydene.2006.11.017.

[67] Borup R, Meyers J, Pivovar B, Kim YS, Mukundan R, Garland N, et al. **Scientific Aspects of Polymer Electrolyte Fuel Cell Durability and Degradation**. *Chem Rev* 2007;107:3904–51.

[68] Campo R, Durán P, Plou J, Herguido J, Peña JA. **Combined production and purification of hydrogen from methanol using steam iron process in fixed bed reactor**. *J Power Sources* 2013;242:520–6. doi:10.1016/j.jpowsour.2013.05.146.

[69] Hormilleja E, Durán P, Plou J, Herguido J, Peña JA. **Hydrogen from ethanol by steam iron process in fixed bed reactor**. *Int J Hydrogen Energy* 2014;39:5267–73. doi:10.1016/j.ijhydene.2014.01.002.

[70] Oyama ST, Hacarlioglu P, Gu Y, Lee D. **Dry reforming of methane has no future for hydrogen production: Comparison with steam reforming at high pressure in standard and membrane reactors**. *Int J Hydrogen Energy* 2012;37:10444–50. doi:10.1016/j.ijhydene.2011.09.149.

[71] Abad A, García-Labiano F, de Diego LF, Gayán P, Adánez J. **Reduction Kinetics of Cu- , Ni- , and Fe-Based Oxygen Carriers Using Syngas ( CO + H 2 ) for Chemical-Looping Combustion**. *Energy & Fuels* 2007;21:1843–53.

[72] Bohn CD, Cleeton JP, Müller CR, Chuang SY, Scott SA, Dennis JS. **Stabilizing Iron Oxide Used in Cycles of Reduction and Oxidation for Hydrogen Production**. *Energy & Fuels* 2010;24:4025–33. doi:10.1021/ef100199f.

[73] Liu W, Dennis JS, Scott SA. **The Effect of Addition of ZrO2 to Fe2O3 for Hydrogen Production by Chemical Looping**. *Ind Eng Chem Res* 2012;51:16597–609.

[74] Voitic G, Nestl S, Lammer M, Wagner J, Hacker V. **Pressurized hydrogen production by fixed-bed chemical looping**. *Appl Energy* 2015. doi:10.1016/j.apenergy.2015.03.095.

[75] Nestl S, Hacker V. **Component Development for Decentralized Sustainable Hydrogen Production**. AIChE Annu. Meet., Pittsburgh: 2012.

[76] Ammendola P, Chirone R, Ruoppolo G, Russo G, Solimene R. **Some issues in modelling methane catalytic decomposition in fluidized bed reactors**. *Int J Hydrogen Energy* 2008;33:2679–94. doi:10.1016/j.ijhydene.2008.03.033.

[77] Thaler M, Hacker V, Anilkumar M, Albering J, Besenhard J, Schrottner H, et al. **Investigations of cycle behaviour of the contact mass in the RESC process for hydrogen production**. *Int J Hydrogen Energy* 2006;31:2025–31. doi:10.1016/j.ijhydene.2006.01.009.

[78] Kidambi PR, Cleeton JPE, Scott S a., Dennis JS, Bohn CD. **Interaction of Iron Oxide with Alumina in a Composite Oxygen Carrier during the Production of Hydrogen by Chemical Looping**. *Energy & Fuels* 2012;26:603–17. doi:10.1021/ef200859d.

[79] Chen S, Shi Q, Xue Z, Sun X, Xiang W. **Experimental investigation of chemical-looping hydrogen generation using Al2O3 or TiO2-supported iron oxides in a batch fluidized bed**. *Int J Hydrogen Energy* 2011;36:8915–26. doi:10.1016/j.ijhydene.2011.04.204.

[80] Ku Y, Liu YC, Chiu PC, Kuo YL, Tseng YH. **Mechanism of Fe2TiO5 as oxygen carrier for chemical looping process and evaluation for hydrogen generation**. *Ceram Int* 2014;40:4599–605. doi:10.1016/j.ceramint.2013.08.138.

[81] Liu W, Ismail M, Dunstan MT, Hu W, Zhang Z, Fennell PS, et al. **Inhibiting the interaction between FeO and Al2O3 during chemical looping production of hydrogen**. *RSC Adv* 2015;5:1759–71. doi:10.1039/C4RA11891J.

[82] Huang T-J, Lin H-J, Yu T-C. **A Comparison of Oxygen-vacancy Effect on Activity Behaviors of Carbon Dioxide and Steam Reforming of Methane over Supported Nickel Catalysts**. *Catal Letters* 2005;105:239–47. doi:10.1007/s10562-005-8697-2.

[83] Kambolis a., Matralis H, Trovarelli a., Papadopoulou C. **Ni/CeO2-ZrO2 catalysts for the dry reforming of methane**. *Appl Catal A Gen* 2010;377:16–26. doi:10.1016/j.apcata.2010.01.013.

[84] Gonzalez-Delacruz VM, Ternero F, Pereñíguez R, Caballero A, Holgado JP. **Study of nanostructured Ni/CeO2 catalysts prepared by combustion synthesis in dry reforming of methane**. *Appl Catal A Gen* 2010;384:1–9. doi:10.1016/j.apcata.2010.05.027.

[85] Srinivas D, Satyanarayana CV V, Potdar HS, Ratnasamy P. **Structural studies on NiO-CeO2-ZrO2 catalysts for steam reforming of ethanol**. *Appl Catal A Gen* 2003;246:323–34. doi:10.1016/S0926-860X(03)00085-1.

[86] Tomishige K, Asadullah M, Kunimori K. **Syngas production by biomass gasification using Rh/CeO2/SiO2 catalysts and fluidized bed reactor**. *Catal Today* 2004;89:389–403. doi:10.1016/j.cattod.2004.01.002.

[87] Miyazawa T, Kimura T, Nishikawa J, Kado S, Kunimori K, Tomishige K. **Catalytic performance of supported Ni catalysts in partial oxidation and steam reforming of tar derived from the pyrolysis of wood biomass**. *Catal Today* 2006;115:254–62. doi:10.1016/j.cattod.2006.02.055.

[88] Duman G, Watanabe T, Uddin MA, Yanik J. **Steam gasification of safflower seed cake and catalytic tar decomposition over ceria modified iron oxide catalysts**. *Fuel Process Technol* 2014;126:276–83. doi:10.1016/j.fuproc.2014.04.035.

[89] Qiao D, Lu G, Liu X, Guo Y, Wang Y, Guo Y. **Preparation of Ce1-x FexO2 solid solution and its catalytic performance for oxidation of CH4 and CO**. *J Mater Sci* 2011;46:3500–6. doi:10.1007/s10853-011-5256-7.

[90] Trovarelli A, de Leitenburg C, Boaro M, Dolcetti G. **The utilization of ceria in industrial catalysis**. *Catal Today* 1999;50:353–67. doi:10.1016/S0920-5861(98)00515-X.

[91] Minicò S, Scirè S, Crisafulli C, Maggiore R, Galvagno S. **Catalytic combustion of volatile organic compounds on gold/iron oxide catalysts**. *Appl Catal B Environ* 2000;28:245–51. doi:10.1016/S0926-3373(00)00181-8.

[92] Basu T, Ghosh UC. **Nano-structured iron(III)–cerium(IV) mixed oxide: Synthesis, characterization and arsenic sorption kinetics in the presence of co-existing ions aiming to apply for high arsenic groundwater treatment**. *Appl Surf Sci* 2013;283:471–81. doi:10.1016/j.apsusc.2013.06.132.

[93] Zhu X, Li K, Wei Y, Wang H, Sun L. **Chemical-Looping Steam Methane Reforming over a CeO2 −Fe2O3 Oxygen Carrier: Evolution of Its Structure and Reducibility**. *Energy & Fuels* 2014;28:754–60.

[94] Gu Z, Li K, Qing S, Zhu X, Wei Y, Li Y, et al. **Enhanced reducibility and redox stability of Fe2O3 in the presence of CeO2 nanoparticles**. *RSC Adv* 2014;4:47191–9. doi:10.1039/C4RA06715K.

[95] Miller D, Siriwardane R V. **Mechanism of methane chemical looping combustion with Fe2O3 promoted with CeO2**. *AIChE 2012 - 2012 AIChE Annu Meet Conf Proc* 2013;27:4087–96.

[96] Lee D, Cha K, Lee Y, Kang K, Park C, Kim Y. **Effects of CeO2 additive on redox characteristics of Fe-based mixed oxide mediums for storage and production of hydrogen**. *Int J Hydrogen Energy* 2009;34:1417–22. doi:10.1016/j.ijhydene.2008.11.084.

[97] Liu F, Chen L, Neathery JK, Saito K, Liu K. **Cerium Oxide Promoted Iron-based Oxygen Carrier for Chemical Looping Combustion**. *Ind Eng Chem Res* 2014;53:16341–8.

[98]    Li F, Kim HR, Sridhar D, Weng F, Zeng L, Chen J, et al. **Syngas Chemical Looping Gasification Process : Oxygen Carrier Particle Selection and Performance**. *Energy & Fuels* 2009;23:4182–9. doi:10.1021/ef900236x.

[99]    Kierzkowska AM, Bohn CD, Scott SA, Cleeton JP, Dennis JS, Mu CR. **Development of Iron Oxide Carriers for Chemical Looping Combustion Using Sol - Gel**. *Ind Eng Chem Res* 2010;49:5383–91.

[100]   Eckhardt B, Ortel E, Bernsmeier D, Polte J, Strasser P, Vainio U, et al. **Micelle-Templated Oxides and Carbonates of Zinc, Cobalt, and Aluminum and a Generalized Strategy for Their Synthesis**. *Chem Mater* 2013;25:2749–58. doi:10.1021/cm400535d.

[101]   **IFA - Databases on hazardous substance** 2015. http://www.dguv.de/ifa/Gefahrstoffdatenbanken/GESTIS-Stoffdatenbank/index-2.jsp (accessed July 21, 2015).

[102]   Laachir A, Perrichon V, Badri A, Lamotte J, Catherine E, Lavalley JC, et al. **Reduction of CeO2 by Hydrogen**. *J Chem Soc Faraday Trans* 1991;87:1601–9.

[103]   Moog I, Prestipino C, Figueroa S, Majimel J, Demourgues A. **Dual Ce4+/Fe3+ Redox Phenomena into Nanocrystalline Ce1-xFexO2-x/2 Solid Solution**. *J Phys Chem C* 2014;118:22746–53.

[104]   Deganello F, Marcì G, Deganello G. **Citrate–nitrate auto-combustion synthesis of perovskite-type nanopowders: A systematic approach**. *J Eur Ceram Soc* 2009;29:439–50. doi:10.1016/j.jeurceramsoc.2008.06.012.

[105]   Chu RQ, Xu ZJ. **Synthesis of mixed-conducting oxide SrFeCo0.5O y powder by auto-combustion of citrate-nitrate gel**. *J Electroceramics* 2008;21:778–81. doi:10.1007/s10832-007-9289-x.

[106]   Mahata T, Das G, Mishra RK, Sharma BP. **Combustion synthesis of gadolinia doped ceria powder**. *J Alloys Compd* 2005;391:129–35. doi:10.1016/j.jallcom.2004.07.085.

[107]   Nestl S, Voitic G, Hacker V. **Investigations of the Steam Iron Process for Decentralised Renewable Hydrogen Production**. 4th Eur. PEFC H2 Forum 2013, Lucerne: 2013.

[108]   Nestl S, Voitic G, Geymayer M, Hacker V. **Component Development for the Reformer Steam Iron Process for Decentralised Sustainable Hydrogen Production**. 2013 AIChE Annu. Meet., San Francisco: 2013.

[109]   Nestl S, Voitic G, Hacker V. **Chemical Looping Hydrogen Production by the Steam Iron Process using Fixed Bed Reactor Technology**. 3rd Int. Conf. Chem. Looping, Gothenburg: 2014.

[110]   Grimmer C, Nestl S, Senn J, Hacker V. **Selective real-time quantification of hydrogen within mixtures of gases via an electrochemical method**. *Int J Hydrogen Energy* 2014;40:2055–61. doi:10.1016/j.ijhydene.2014.11.126.

[111]   Cheng X, Shi Z, Glass N, Zhang L, Zhang J, Song D, et al. **A review of PEM hydrogen fuel cell contamination: Impacts, mechanisms, and mitigation**. *J Power Sources* 2007;165:739–56. doi:10.1016/j.jpowsour.2006.12.012.

[112] Bender G, Angelo M, Bethune K, Rocheleau R. **Quantitative analysis of the performance impact of low-level carbon monoxide exposure in proton exchange membrane fuel cells**. *J Power Sources* 2013;228:159–69. doi:10.1016/j.jpowsour.2012.11.062.

[113] St-Pierre J. **PEMFC contaminant tolerance limit-CO in H2**. *Electrochim Acta* 2010;55:4208–11. doi:10.1016/j.electacta.2010.02.061.

[114] Antolini E. **The problem of Ru dissolution from Pt-Ru catalysts during fuel cell operation: Analysis and solutions**. *J Solid State Electrochem* 2011;15:455–72. doi:10.1007/s10008-010-1124-7.

[115] Hassan A, Paganin VA, Ticianelli EA. **Applied Catalysis B : Environmental Pt modified tungsten carbide as anode electrocatalyst for hydrogen oxidation in proton exchange membrane fuel cell : CO tolerance and stability**. *"Applied Catal B, Environ* 2015;165:611–9. doi:10.1016/j.apcatb.2014.10.068.

[116] Fraser SD, Monsberger M, Hacker V. **A thermodynamic analysis of the reformer sponge iron cycle**. *J Power Sources* 2006;161:420–31. doi:10.1016/j.jpowsour.2006.04.082.

[117] Park ED, Lee D, Lee HC. **Recent progress in selective CO removal in a H2-rich stream**. *Catal Today* 2009;139:280–90. doi:10.1016/j.cattod.2008.06.027.

[118] Brunauer S, Emmett PH, Teller E. **Adsorption of Gases in Multimolecular Layers**. *J Am Chem Soc* 1938;60:309–19. doi:10.1021/ja01269a023.

[119] Barrett EP, Joyner LG, Halenda PP. **The Determination of Pore Volume and Area Distributions in Porous Substances. Computations from Nitrogen Isotherms**. *J Am Chem Soc* 1951;73:373–80.

[120] Sing KS. **Adsorption methods for the characterization of porous materials**. *Adv Colloid Interface Sci* 1998;76-77:3–11. doi:10.1016/S0001-8686(98)00038-4.

[121] Klobes P, Meyer K, Munro RG. **Porosity and Specific Surface Area Measurements for Solid Materials**. National Institute of Standards and Technology; 2006.

# 9. Appendix

## 9.1. List of Abbreviations, terms and symbols

| | |
|---|---|
| BET | Brunauer–Emmett–Teller method |
| BSE | backscattered electrons |
| CLC | chemical looping combustion |
| CLH | chemical looping hydrogen production |
| CLR | chemical looping reforming |
| CL-SMR | chemical looping-steam methane reforming |
| $CO_2$-eq | carbon-dioxide equivalent |
| CS | consumed syngas; see Eqxy SEQ |
| EDX | energy-dispersive X-ray spectroscopy |
| ETD | Everhart-Thornley-detector |
| GHG | greenhouse-gas |
| IPCC | International Panel on Climate Change |
| LHV | lower heating value |
| MEA | monoethanolamine scrubbing |
| MFC | mass flow controller |
| OC | oxygen carrier |
| PEM-FC | proton exchange membrane fuel cells |
| ppb | parts per billion |
| ppm | parts per million |
| PSA | pressure swing adsorption |
| RESC | reformer sponge iron cycle |
| s/c-ratio | mole of steam per mole of carbon present in hydrocarbon feedstock |

SE          secondary electrons

SEM         scanning electron microscopy

SEQ         syngas equivalent

SMR         steam methane reforming

TGA         thermogravimetric analysis

TPR         temperature programmed reduction

XRD         X-ray diffraction

YSZ         Yttria-stabilised zirconia

## 9.2. List of Figures

## 9.3. List of Tables

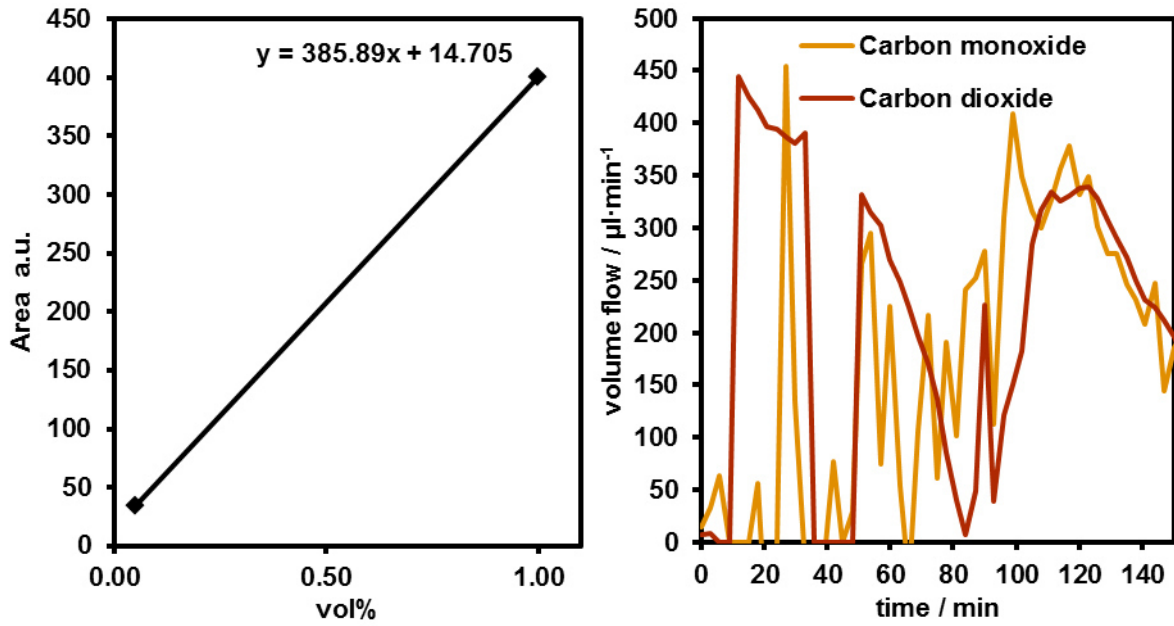## 9.4. Supplementary data



**Figure-A I: 2-point calibration for carbon monoxide concentrations between 0.05% and 1% (left) and volume flow of carbon monoxide and carbon dioxide (right).**
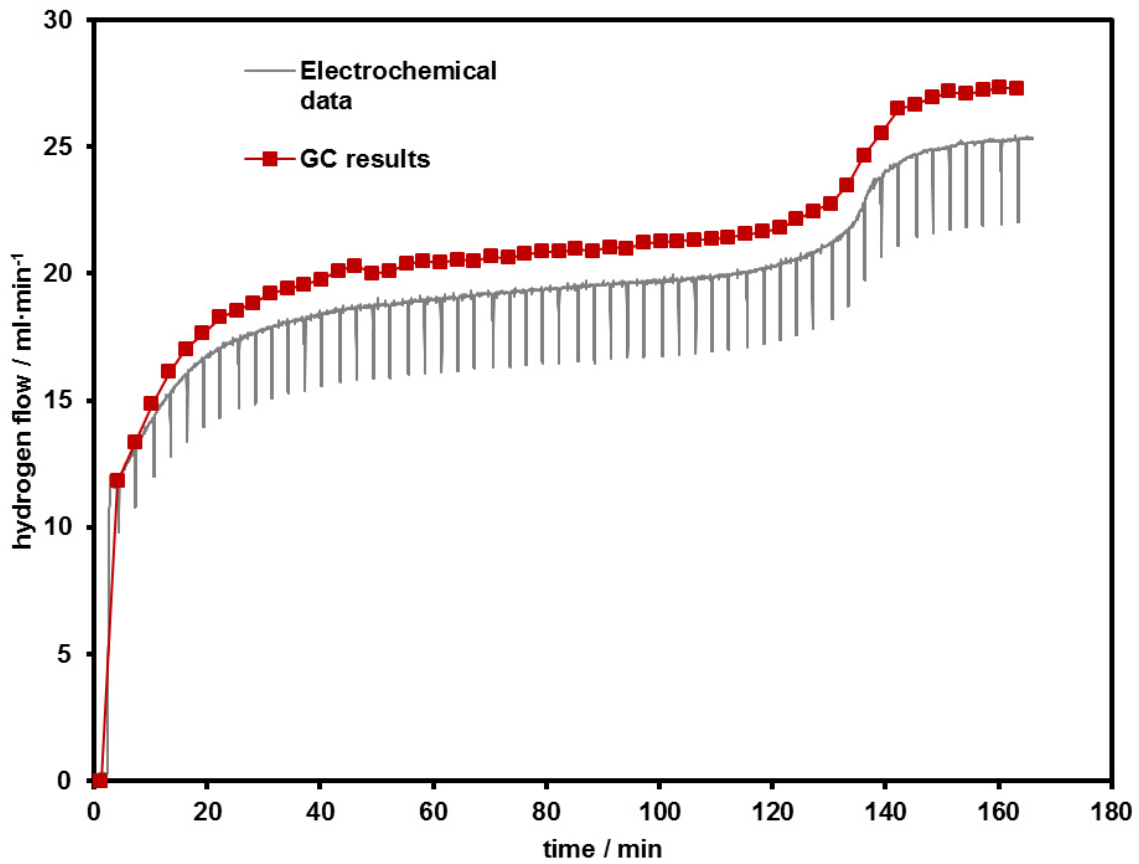


**Figure-A II: Hydrogen flow of the reduction step of the steam iron chemical looping process; comparison of electrochemical data and GC results [110].**
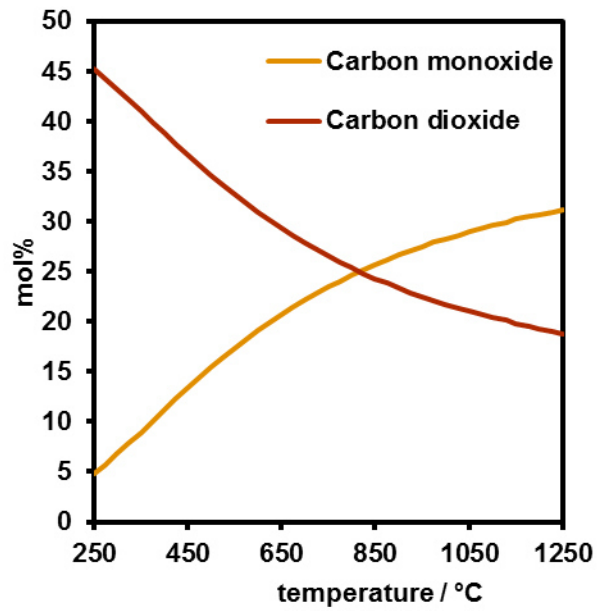
**Figure-A III: Calculated carbon monoxide and carbon dioxide ratio as a function of temperature; $(H_2+H_2O)/(CO+CO_2)=1$.**
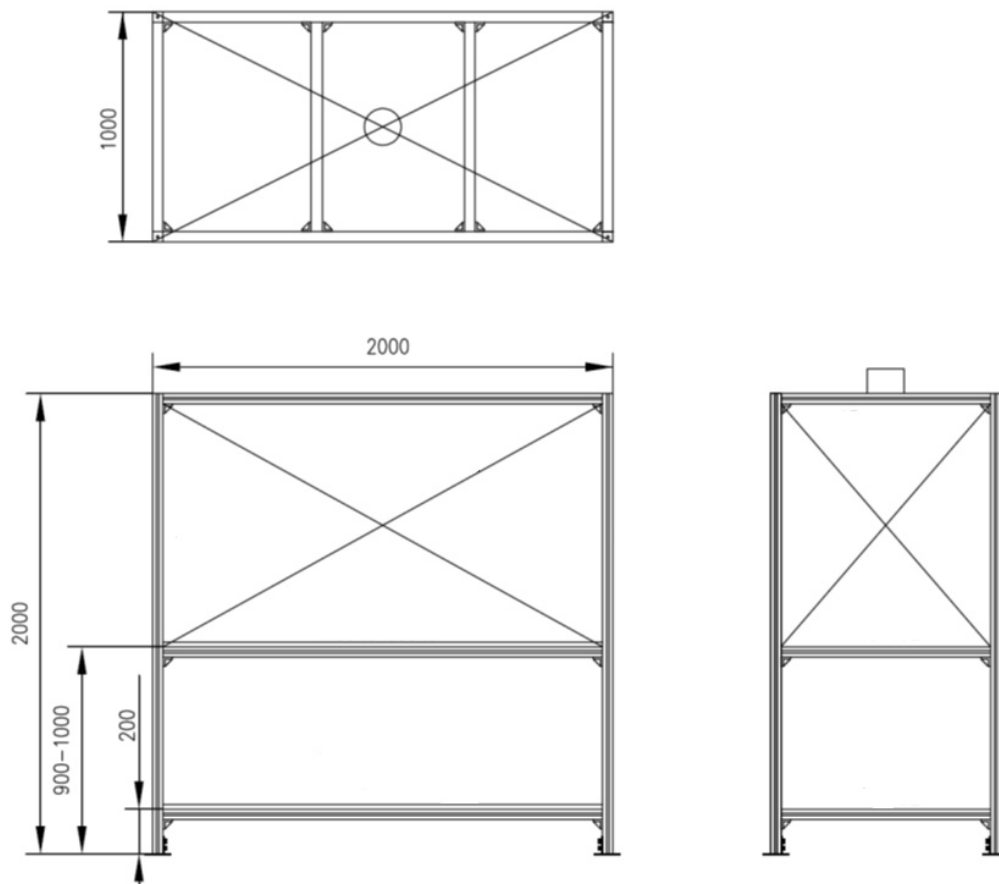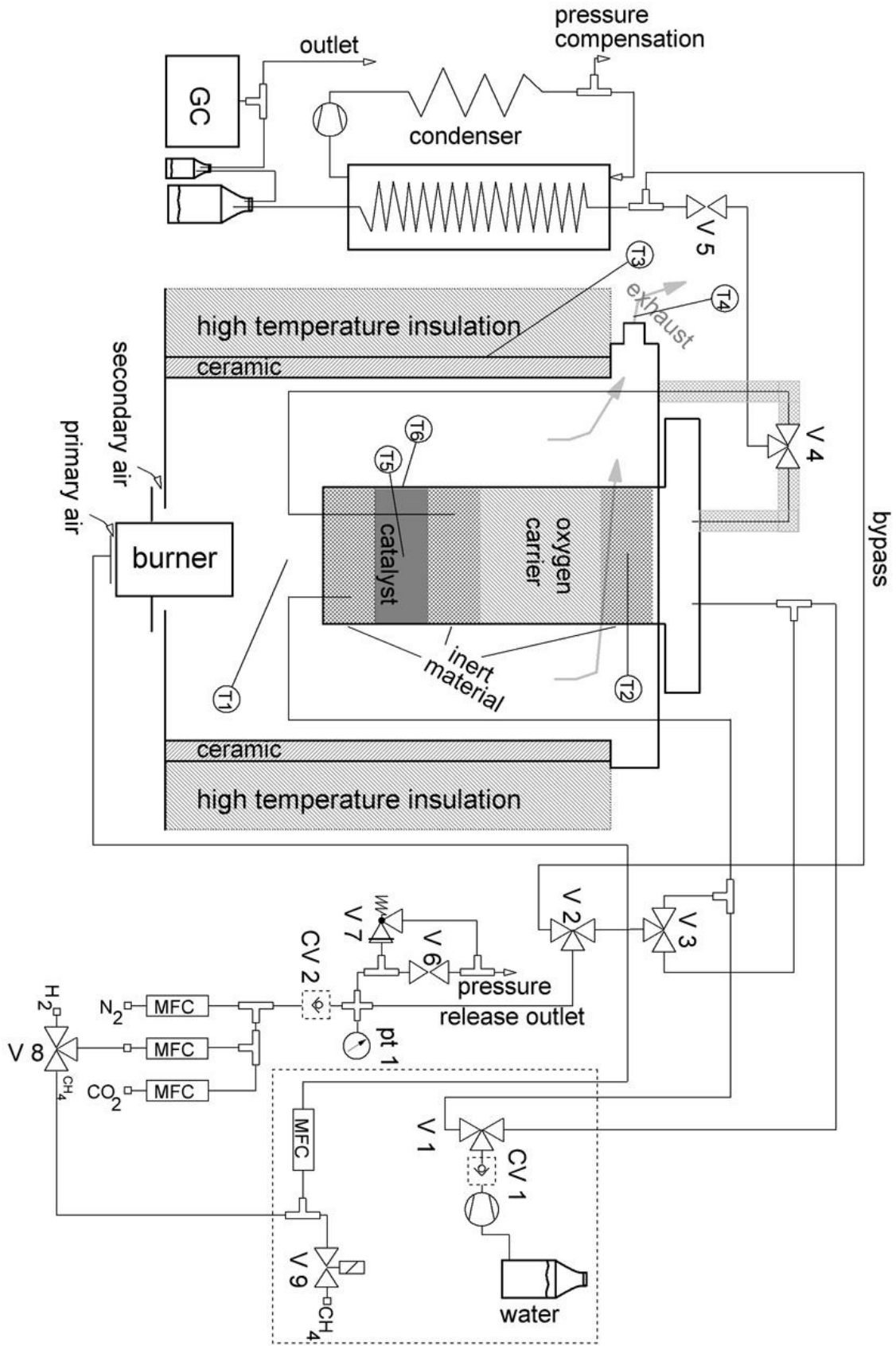


**Figure-A IV: Dimensions of the RSA-test rig**

**Figure-A V: Detailed plan of the prototype; drawn by R. Strasser.**

**Table-A I: Components list of the prototype.**

| Component | Company | Specifications |
|---|---|---|
| Gas burner | Pharos | IB 00 N/F-8.4 kW |
| Ignition electrode | Pharos | - |
| Gas burner Safety Control | Honeywell | DKG 972 |
| Ignition transformer | MCT Transformatoren GmbH | MCT ZA-30 075 LH 21-01 230V 1.24A 50 Hz |
| Ceramic tube | Haldenwanger | Pythagoras tube |
| Thermal insulation | ELI-Therm | ISOBLOCK R 126/128 (7320 x 610 x 25 mm) |
| Mass flow controllers | Bronkhorst | EL-Flow |
| Relief Valve | Sison | RLSS-ML6-7 |
| Solenoid valve | END-Armaturen GmbH & Co. KG | 230V 0-10 bar |
| PID-controller | ENDA | ETC-442-SSR |
| Solid state relay | Celduc relais | XKA20420 |
| Thermocouple data logger | Pico technology | TC-08 |
| Main switch | RS-components | 3SB3400-0B |
| Kill switch | RS-components | 3SB3400-0A NC |
| Fuse-1 | - | 400V 6A |
| Fuse-2 | - | 400V 4A |
| Fuse-3 | - | 400V 2A |
| Pump for steam supply | Ismatec | Reglo-peristaltic pump |
| Pump for product cooling | Ismatec | Reglo-Z |

**FORTRAN statements used for the calculations in chapter 5.4**

**Calculator block before optimisation:**

XH2O=0.6

XCO2=0.7

HH2F=24553.25

HCOF=-10274.5

HH2W=47700

HCOW=12873


COSOUT=(1-XCO2)*(COSIN+CO2SIN)

CO2SOUT=XCO2*(COSIN+CO2SIN)

H2SOUT=(1-XH2O)*(H2SIN+H2OSIN)

H2OSOUT=XH2O*(H2SIN+H2OSIN)

CH4SOUT=CH4SIN


H2RED=H2SIN-H2SOUT

CORED=COSIN-COSOUT

H2OXOUT=H2RED+CORED


DUTYSRED=(H2RED* HH2W)+(CORED*HCOW)

TSIR=TREF


H2OCON=0.26

WATEROX=H2OXOUT/H2OCON

H2OOXOUT=WATEROX-H2OXOUT

DUTYSOX=H2OXOUT*HH2W*-1

**Calculator block including heat recovery and off-gas combustion:**

OXIN=((CH4IN*2)+(COIN*0.5)+(H2IN*0.5))*1.2

N2IN=OXIN*0.79/0.21


XH2O=0.8

XCO2=0.8

HH2F=24553.25

HCOF=-10274.5

HH2W=46115

HCOW=12983


COSOUT=(1-XCO2)*(COSIN+CO2SIN)

CO2SOUT=XCO2*(COSIN+CO2SIN)

H2SOUT=(1-XH2O)*(H2SIN+H2OSIN)

H2OSOUT=XH2O*(H2SIN+H2OSIN)

CH4SOUT=CH4SIN


H2RED=H2SIN-H2SOUT

CORED=COSIN-COSOUT

H2OXOUT=H2RED+CORED


DUTYSRED=(H2RED* HH2W)+(CORED*HCOW)

TSIR=TREF


H2OCON=0.2

WATEROX=H2OXOUT/H2OCON

H2OOXOUT=WATEROX-H2OXOUT

DUTYSOX=H2OXOUT*HH2W*-1